Università degli Studi di Modena e Reggio Emilia

Dipartimento di Ingegneria "Enzo Ferrari"

Ph.D. School

Industrial and environmental engineering

- XXXIII cycle –

THERMAL ANOMALIES DETECTION ON NATURAL AND URBAN AREAS USING SATELLITE TIR TIME SERIES

Tutor: Prof. Sergio Teggi

PhD Director School: Prof. Alberto Muscio

Candidate: Malvina Silvestri

Academic year 2019/2020

What we know is a drop,

what we don't know is an ocean.

Isaac Newton

Table of contents

List of figures

List of tables

ABSTRACT

Current satellite missions, providing imagery in the Thermal InfraRed (TIR) spectral region at 60-100 meters of spatial resolution, give the possibility to estimate the land surface temperature (LST) and highlight the main surface thermal anomalies, i.e. areas where the surface temperature has a value significantly different from the background. Thermal anomalies are potentially related to the underground energy sources or to land use and coverage variations as urban areas where the urban heat island (UHI) phenomenon can be observed. This work wants to fit in these two fields.

Two separate analyses on two case studies were carried out. The first case study is the detection of thermal anomalies on geothermal active areas (volcanic or not). The second focuses on the detection of UHI. Both the studies are based on remote sensing LST time series.

In the first study, ASTER and TIRS/Landsat 8 time series have been processed using two different methodologies: Temperature and Emissivity Separation (TES) algorithm for ASTER and Single Channel Algorithm (SCA) for Landsat 8. Two LST time series have been obtained and results are cross-compared and validated with ground measurements. TES and SCA are well-known methodologies and have been used to evaluate LST on two different test sites with different geological features: the volcanic area of *Solfatara-Campi Flegrei* and the geothermal area of *Parco delle Biancane*.

The second case study has been addressed to the characterization of the UHI of the city of *Modena*. The analysis is based on TIRS/Landsat 8 image time series processed using the SCA methodology.

In both the case studies the thermal anomalies detection is also inspected using the principal component analysis (PCA) of the LST time series. The results of these studies furnished some important considerations:

- the methodologies used to obtain LST produce reliable temperature estimates also in the very particular case of geothermal anomalies and usable for near ground air temperature trends analysis;
- PCA allows to extract the dominant patterns within the time series as the detection of thermal anomalies offering a good and easy way to produce very detailed maps of thermal anomalies both in geothermal areas and in urban areas (UHI);
- the PCA allows the differentiation of the surface cover without using other remote sensing images in VIS/NIR or auxiliary classification products. This differentiation improves the analysis of the thermal behavior of the surfaces.

The two studied cases represent two more demonstrations of the potentiality of satellite observations in TIR for environmental applications.

SOMMARIO

Le attuali missioni satellitari che forniscono immagini nella regione spettrale dell'infrarosso termico (TIR) e con una risoluzione spaziale di 60-100 metri, permettono la stima della temperatura del suolo (LST) e sono capaci di evidenziare anomalie termiche, aree cioè dove la temperatura superficiale ha un valore significativamente diverso da quella di background. Le anomalie termiche sono potenzialmente legate a fonti di energia presenti nel sottosuolo o ad una modifica dell'uso e della sua copertura come ad esempio le aree urbane dove è possibile osservare il fenomeno delle isole di calore (UHI). Il presente lavoro di dottorato vuole analizzare a questi due campi.

Sono stati condotti due tipi di analisi su due casi di studio. Il primo caso di studio è l'individuazione di anomalie termiche su aree geotermicamente attive (vulcaniche e non). Il secondo è focalizzato sull'identificazione dell'UHI. Entrambi i casi sono basati sulle serie storiche di LST ottenute da dati satellitari.

Nel primo studio, le serie storiche dei sensori ASTER e TIRS/Landsat 8 sono state elaborate utilizzando due diverse metodologie: l'algoritmo Temperature and Emissivity Separation (TES) per ASTER e il Single Channel Algorithm (SCA) per Landsat 8. Sono state ottenute due serie storiche LST e i risultati sono stati confrontati e validati con misure a terra. TES e SCA sono metodologie note e sono state applicate su due siti con differenti caratteristiche geologiche: l'area vulcanica dei *Solfatara-Campi Flegrei* e l'area geotermica del *Parco delle Biancane*.

Il secondo caso di studio ha riguardato la caratterizzazione dell'UHI della città di *Modena*. L'analisi è basata sull'utilizzo delle serie temporali di LST di immagini TIRS / Landsat 8 ottenute tramite la metodologia SCA.

In entrambi i casi di studio l'identificazione dell'anomalia termica è stata indagata anche basandosi sull'analisi delle componenti principali (PCA) sulle serie temporali di LST. I risultati ottenuti da questi studi hanno fornito alcune importanti considerazioni:

- le metodologie usate per ottenere la stima di LST producono una buona stima di temperatura anche in aree molto particolari dove sono presenti anomalie geotermiche e sono utilizzabili per l'analisi dell'andamento di temperatura dell'aria vicino al suolo;
- il metodo della PCA consente l'estrazione di pattern dominanti all'interno delle serie temporali come l'individuazione di anomalie termiche, offrendo una buona e facile soluzione per evitare questo problema generando una mappa molto ben dettagliata delle anomalie termiche in entrambe le aree geotermiche e nelle aree urbane (UHI);
- il metodo della PCA consente la differenziazione della copertura superficiale senza utilizzare altre immagini di telerilevamento in VIS / NIR o prodotti di classificazione ausiliari. Questa differenziazione migliora l'analisi del comportamento termico delle superfici.

I due casi di studio rappresentano due ulteriori dimostrazioni della potenzialità delle osservazioni satellitari nella regione dell'infrarosso termico per applicazioni di tipo ambientale.

ACKNOWLEDGMENTS

I would like to thank many people who have accompanied me during the three years of this thesis work.

First of all, I would like to express my deepest gratitude to my advisor Prof. Sergio Teggi for his patient guidance and continuing support to conduct this thesis research, for motivation, enthusiasm, and immense knowledge. Thanks for letting me carry out my research freely.

My sincere thanks to Dr. Maria Fabrizia Buongiorno and Dr. Massimo Musacchio for their friendship, for introducing me in the "Remote Sensing world", for collaborating together in several projects and whose help in this thesis has been fundamental.

Special thanks goes to Dr. Federico Rabuffi and Dr. Vito Romaniello, the first one for his help in GIS environment, the second one for support in statistical analyses.

Thanks to Dr. Enrica Marotta and Dr. Francesca Despini for their friendship and continuous encouragement during these years.

Thanks to my colleagues Dr. Fabio Sansivero, Dr. Giuseppe Vilardo for the availability of TIRNet data and thanks to Dr. Eliana Bellucci Sessa and Dr. Teresa Caputo for their support in TIRNet data processing and kindness at all time.

I also thank INGV- OV drone team (Dr. Gala Avvisati and Pasquale Belviso) for data acquisition during the Parco delle Biancane field campaigns. Moreover, thanks to Dr. Rosario Peluso for helping in the interpretation of *Solfatara* area and Dr. Luca Lombroso for *Modena* weather station data.

Sincere thanks to the two proofreaders, Dr. Vincent J. Realmuto and Dr. Stefano Pignatti for their constructive comments and suggestions.

Last but not the least I would like to say a special thanks to two important people: Valentina for supporting and believing in me until the end continuously giving me joy and satisfaction in my life and my little brother Marcello, his wonderful and gentle soul will forever remain in my heart…

" *…tanto domani corri!*".

1 INTRODUCTION

1.1 Problem definition

Remote sensing allows us to observe the Earth surface at a large scale, with a defined acquisition frequency, and with a favorable cost-benefit ratio; moreover, it allows us to acquire data in areas that are difficult to reach. Current satellite missions, providing imagery in the Thermal InfraRed (TIR) spectral region at 60-100 meters of spatial resolution, give the possibility to estimate the land surface temperature (LST) and highlight the main surface changes, potentially related to the underground energy sources. In this contest, remote sensing represents an effective and expedite tool to acquire TIR images when there are large extents of areas showing thermal anomalies, i.e. areas where the surface temperature has a value significantly different from the background. In areas where the presence of crustal heat flow is anomalously high, geothermal systems transfer heat to the Earth's surface often through hot springs, fumaroles, heated ground and associated mineral deposits. Moreover, the use of TIR satellite at different spatial resolution offers the possibility to identify the presence of thermal anomalies on volcanic areas which could potentially be related to changes in volcanic activity [1, 2, 3]. Surface temperature and the relative presence of thermal anomaly can be also considered an indicator of possible geothermal energy for economic exploitation [4 - 6].

Although coarse spatial resolution satellite thermal sensors (60-100 m pixels), such as TIRS/Landsat, ASTER or the latest ECOSTRESS, have limited potential for detailed mapping of small geothermal features, a number of studies have exploited these datasets for broader scale detection of geothermal anomalies [7, 8 and references therein]. However, at the resolution of satellite TIR data, due to the heterogeneous nature of surfaces, pixels can be mixed: background surface radiance and radiance due to underground sources can be present in the same pixel. This means that the surface temperature estimated by satellite TIR data is often composed of a mixture of different temperature components: the temperature corresponding to thermal anomalies and the background. Despite this, the use of satellite data can help the exploration and monitoring of areas where the presence of anomalous variation of surface temperature is present.

As mentioned, LST can be used to detect shallow thermal anomalies for geothermal exploration and it is used as an indicator of the thermal information associated with volcanic complexes.

LST can be also used as a key factor to obtain surface heat fluxes for a variety of investigations such as Urban Heat Island (UHI) effect [9, 10], a

phenomenon characterized by the heating of urban zones with respect to its non-urbanized surroundings. UHI is considered as one of the most important problems of overheating in urban areas with impacts as increasing of urban smog, increasing of air-conditioning mainly in hot climate regions (with a consequence increasing of energy consumption) and influence on human health. Remote sensing data are a powerful tool to study the urban environment offering the advantage to cover the entire urban area at the same time with respect to the urban weather station (not always evenly distributed spatially within the city with consequence of no coverage of large areas).

1.2 Aim, relevance and novelty of the work

This work wants to fit in these concepts. Two separate analysis were carried out with the retrieval of surface temperature through remote sensing data: the first is based on the detection of thermal anomalies by using LST time series estimated on geothermal active areas (volcanic or not), the second focuses on the detection of UHI by using same approach.

In the first case, ASTER and Landsat 8 time series have been used. The LST time series are obtained using two different methodologies: temperature and emissivity separation (TES) algorithm for ASTER and single channel algorithm (SCA) for Landsat 8; results are validated with cross-comparison or with ground measurements. The validation is an important step to consider because the primary difficulty in estimating surface temperature from TIR satellite data is the variable emissivity associated with different surface types. In this work the emissivity is automatically estimated by TES for ASTER data by using multiple observations from its five thermal bands while ASTER-GED emissivity (distributed by USGS) is used as input file for Landsat 8 because for this sensor only one thermal channel is considered (detailed information will be described in the next sections). The well-known methodologies have been used to evaluate the surface temperature on two different test sites with different geological features: the volcanic area of *Solfatara-Campi Flegrei* and the geothermal area of *Parco delle Biancane*.

The second case study is an application of the methodology used in the first case study on a TIRS/Landsat 8 image time series acquired on the *Modena* city area to characterize the UHI.

In both the case studies the thermal anomaly detection is inspected using the principal component analysis (PCA) of the LST time series and statistical analyses.

The approach to the proposed work is shown in the Figure 1.

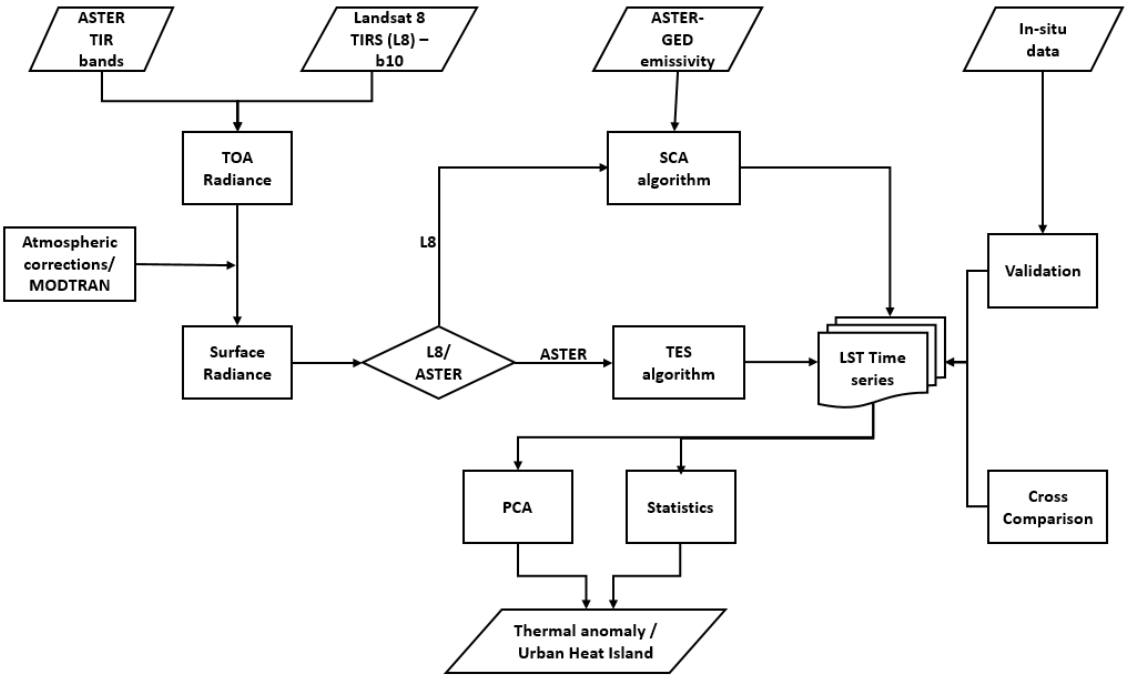

Figure 1. Flow chart for LST retrieval and thermal anomaly detection.

The novelty of this work can be highlighted in following points: 1) the combination of two different methodologies (TES and SCA methodologies, described in 4) to obtain LST time series taking advantage of TIR satellite data having a pixel spatial resolution less than 100 meters; 2) the test of application in different contexts (geothermal and urban areas); 3) the detection of thermal anomalies based on LST time series which are often affected by seasonal trends and therefore the use of PCA method to solve this problem producing very detailed maps of thermal anomalies both in geothermal areas and in urban areas.

The points 1) and 2) are synthetised in Table 1:

	LST		
Applications	Geothermal areas		Urban Heat Island (UHI)
Sites	Volcanic area (*Solfatara - Campi Flegrei)*	No volcanic area (*Parco delle Biancane*)	*Modena City*
Data/Algorithm	ASTER data - > TES	ASTER data - > TES	TIRS/Landsat 8 -> SCA
	TIRS/Landsat 8 -> SCA	TIRS/Landsat 8 -> SCA	

Table 1. Sites and algorithms used for LST retrieval.

Remote sensing offers a complementary input especially in the prefeasibility stages of geothermal exploration through the synoptic coverage of large areas and the detection of anomalies exhibited by temperature and surface

manifestations. In this work, the used methodologies provide a consistent and effective way if implementing operation related to decoding of information from the thermal anomaly as well as identifying its location. Considering that this kind of geothermal energy is one of the clean energy types, its detection has been much of interest for earth scientists.

Moreover, with this work, the use of TIR satellite data in the environmental field is consolidated and concerning the UHI it can integrate measurements collected by weather stations. Even if the weather station data is accurate, it records what is happening at ground level, requiring constant recording, maintenance and measurements to rely on, only in the immediate vicinity of the station, TIR satellites provide measurements at very large scale with no differences in accuracy.

1.3 Thesis outline

This work is divided in the following parts:

- Chapter 1 is the introduction to the work with problem definition, relevance and novelty;
- Chapter 2 provides an overview on remote sensing data used in this work;
- Chapter 3 describes the satellite data used and the test sites description;
- Chapter 4 is focused on the Radiative Transfer Equation and the necessity to consider the atmospheric corrections on satellite data. Moreover, two methodologies have been considered and described and the process for obtaining LST time series. Validations are also reported for all test sites;
- Chapter 5 provides the PCA use for the thermal anomaly detection and results.

The conclusions are also provided together with the acronyms list used in this work. References are included in each Chapter.

1.4 References of chapter 1

1. Buongiorno, M. F., Pieri, D., & Silvestri, M. (2013). Thermal analysis of volcanoes based on 10 years of ASTER data on Mt. Etna. In Thermal Infrared Remote Sensing (pp. 409-428). Springer, Dordrecht.
2. Pieri, D., & Abrams, M. (2004). ASTER watches the world's volcanoes: a new paradigm for volcanological observations from orbit. Journal of Volcanology and Geothermal Research, 135(1-2), 13-28.
3. Silvestri, M., Romaniello, V., Hook, S., Musacchio, M., Teggi, S., & Buongiorno, M. F. (2020). First Comparisons of Surface Temperature Estimations between ECOSTRESS, ASTER and Landsat 8 over Italian Volcanic and Geothermal Areas. Remote Sensing, 12(1), 184.

4. Fridleifsson, I. B., Bertani, R., Huenges, E., Lund, J. W., Ragnarsson, A., & Rybach, L. (2008, January). The possible role and contribution of geothermal energy to the mitigation of climate change. In IPCC scoping meeting on renewable energy sources, proceedings, Luebeck, Germany (Vol. 20, No. 25, pp. 59-80).
5. Howari, F. (2015). Prospecting for geothermal energy through satellite based thermal data: Review and the way forward. Global Journal of Environmental Science and Management, 1(4), 265-274.
6. Qin, Q., Zhang, N., Nan, P., & Chai, L. (2011). Geothermal area detection using Landsat ETM+ thermal infrared data and its mechanistic analysis—A case study in Tengchong, China. International Journal of Applied Earth Observation and Geoinformation, 13(4), 552-559.
7. Sekertekin, A., & Arslan, N. (2019). Monitoring thermal anomaly and radiative heat flux using thermal infrared satellite imagery–A case study at Tuzla geothermal region. Geothermics, 78, 243-254.
8. Haselwimmer, C., & Prakash, A. (2013). Thermal infrared remote sensing of geothermal systems. In Thermal Infrared Remote Sensing (pp. 453-473). Springer, Dordrecht.
9. Voogt, J. A., & Oke, T. R. (2003). Thermal remote sensing of urban climates. Remote sensing of environment, 86(3), 370-384.
10. Sobrino, J. A., Oltra-Carrió, R., Sòria, G., Bianchi, R., & Paganini, M. (2012). Impact of spatial resolution and satellite overpass time on evaluation of the surface urban heat island effects. Remote Sensing of Environment, 117, 50-56.

2 SATELLITE REMOTE SENSING TIR SENSORS

Surface temperature is a key signature of surface energy budgets; it can be directly related to the surface energy fluxes, and particularly to the latent heat flux (evapotranspiration) and water stress.

LST is the effective temperature calculated from the mean radiance emitted by all the objects on the instrument field of view, as measured by ground-based, airborne, and spaceborne remote radiometers. Considering that LST derives from a radiative energy balance of the surface, it provides a good approximation to the thermodynamic surface temperature. The terms composing the theoretical basis for LST are the energy balance, the blackbody emission laws and the atmospheric radiative transfer modeling. LST can be determined from satellite measurements of radiation emitted at wavelengths in either infrared or microwave atmospheric windows. Retrievals in TIR region are preferred since at ambient temperature surface emission is maximum in this region (Wien's law) and surface emissivity is less variable than in the microwave spectral region [11, 12 and references therein].

TIR Earth Observation satellite sensors measure top-of-atmosphere (TOA) radiance, which consists of the upwelling radiance emitted by the ground, the upwelling radiance emitted by the atmosphere, and the part of the downwelling irradiance emitted by the atmosphere and reflected by the ground which reaches the TOA (Figure 2). All these terms can be expressed in a Radiative Transfer Equation (RTE) that will be described in the next chapter. Accurate LST retrievals are challenging due to different effects, which include atmospheric interactions, transmittance and mainly absorption by gases, water vapor and clouds and surface emissivity.

2.1 Satellite data

The current space sensors with high temporal resolution and with low spatial resolution are most useful for retrieving meteorological and climate information, while only few space sensors show appropriate TIR spectral channels with moderate spatial resolution. These sensors allow to investigate the complex interactions between many Earth processes at smaller scale. One important objective is to acquire significant information by observing phenomena at different scales and therefore understanding how the changes originated at regional and local level produce effects at global-scale.

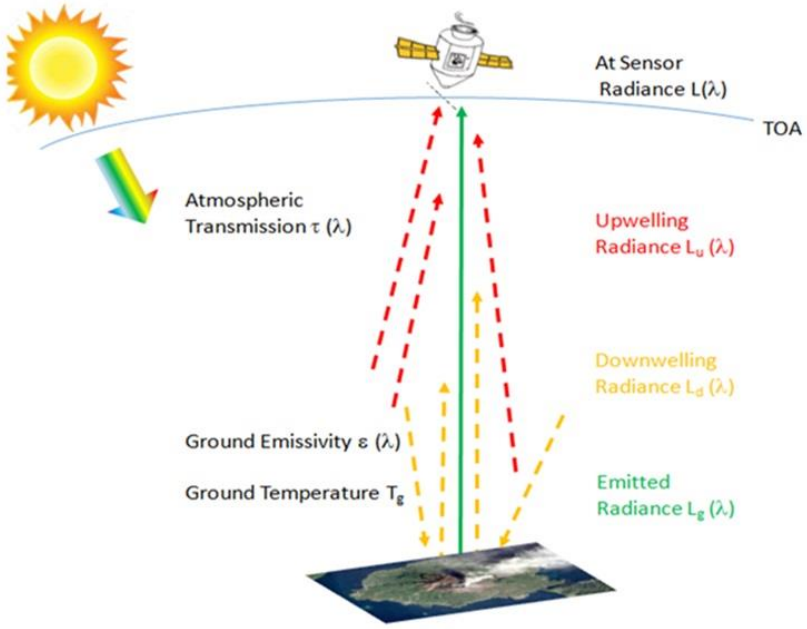

Figure 2. TOA radiance measured by satellites.

Only with the launch of the Terra satellite at the end of 1999, many of the techniques developed by the research community have been transferred to image space-borne sensors with mid-low spatial resolution (MODIS or Moderate Resolution Imaging Spectroradiometer, SLSTR or Sea and Land Surface Temperature Radiometer on Sentinel 3, MSG or Meteosat Second Generation). This generation of systems allowed the consolidation and extension of the use of TIR channels to retrieve parameters of the Earth surface and low atmosphere. The spatial scale at which thermal phenomena are observed, is given by the Ground Sampling Distance (GSD, more generally, spatial resolution) and swath, while the temporal scale is linked to the revisit time on a given area, which in turn depends on orbit swath dimension and steering capability of the sensor. In order to observe phenomena on "regional to local" scale, GSD of 60-100 m is required as well as a short revisit time. At today, ASTER (Advanced Spaceborne Thermal Emission and Reflection Radiometer) on Terra and TIRS (Thermal InfraRed Sensor) on Landsat 8 offer such a capability with 90-100 m of spatial resolution (swath width of 60 km and 185 km respectively, within the 8-12 μm atmospheric window) and low revisit time (16 days). ECOSTRESS (ECOsystem Spaceborne Thermal Radiometer Experiment on International Space Station) is the new experimental stage space mission of NASA-JPL, launched on July 2018, with a multispectral thermal infrared radiometer to measure radiance in five spectral channels ranging from 8 to 12 μm and an additional band at 1.6 μm for geolocation and cloud detection (six bands in total) [13, 14, 15]. ECOSTRESS has been launched with the aim to measure the temperature of plants and understand their evaporative

stress [16]. Its high spatial resolution (69 m x 38 m, 2 pixels in cross track and 1 pixel in down track) and revisit time (about 4-5 days) provides a significant improvement to the operative thermal infrared missions for LST estimation. Unfortunately, this sensor is not considered for this work due to the small number of data collected in only two years of activity.

Night-time image analysis is essential for most applications because the thermal contrast due to solar heating is absent, then the thermal anomalies could be discriminated more easily due also to the absence of topographic effects and reflectance component of the surface (common in daytime images). Another advantage of night-time images is that surface radiant temperature is more constant than in the daytime. For these reasons, ASTER and Landsat 8 TIRS nighttime image series have been considered in this study.

2.1.1 Landsat 8

Landsat is the only U.S. satellite system designed and operated to repeatedly observe the global land surface at a moderate scale that shows both natural and human-induced changes.

Landsat satellites have been collecting imagery of the Earth's surface since 1972 (Figure 3), creating a historical archive that is unmatched. The millions of scenes held in the USGS (United States Geological Survey) archives provide useful science to all users worldwide.

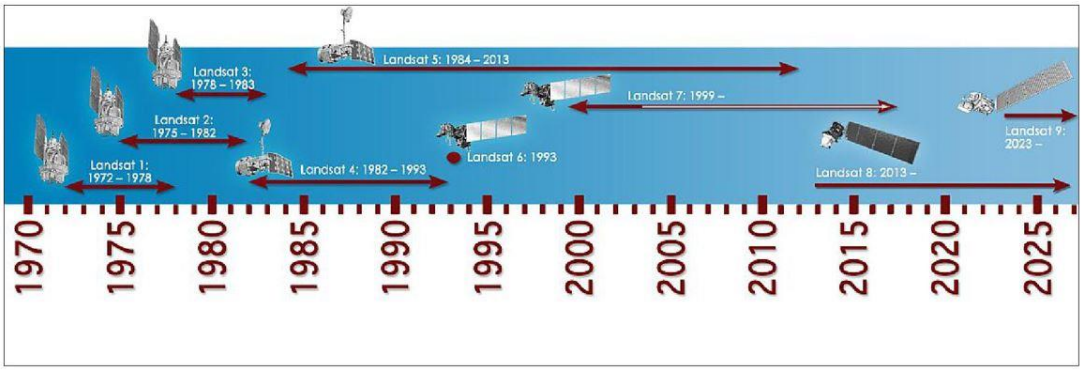

Figure 3. Landsat mission from 1972 till today (credit NASA).

Landsat 8 is the last satellite launched on February 11, 2013 [17, 18]. It has two main sensors: the Operational Land Imager (OLI) and the Thermal Infrared Sensor (TIRS). OLI collects images using nine spectral bands in different wavelengths of visible, near-infrared, and shortwave light to observe a 185 km wide swath of the Earth in 15-30 m spatial resolution covering wide areas of the Earth's landscape while providing sufficient resolution to distinguish features like urban centers, farms, forests and other land uses. TIRS images consist of two bands (10 and 11) useful in providing more accurate surface temperatures

and are collected at 100 m spatial resolution. Approximate scene size is 170 km north-south by 183 km east-west. In Table 2 the Landsat 8 band features are reported, while in Figure 4 an example of data acquired by Landsat 8 in the TIR band 10 is shown.

Landsat 8 Operational Land Imager (OLI) and Thermal Infrared Sensor (TIRS) Launched February 11, 2013	Bands	Wavelength (micrometers)	Resolution (meters)
	Band 1 - Coastal aerosol	0.43 - 0.45	30
	Band 2 - Blue	0.45 - 0.51	30
	Band 3 - Green	0.53 - 0.59	30
	Band 4 - Red	0.64 - 0.67	30
	Band 5 - Near Infrared (NIR)	0.85 - 0.88	30
	Band 6 - SWIR 1	1.57 - 1.65	30
	Band 7 - SWIR 2	2.11 - 2.29	30
	Band 8 - Panchromatic	0.50 - 0.68	15
	Band 9 - Cirrus	1.36 - 1.38	30
	Band 10 - Thermal Infrared (TIRS) 1	10.60 - 11.19	100 * (30)
	Band 11 - Thermal Infrared (TIRS) 2	11.50 - 12.51	100 * (30)

Table 2. Landsat 8 band features; * TIRS bands are acquired at 100 m spatial resolution, but are resampled to 30 m in delivered data product. (http://landsat.usgs.gov/).

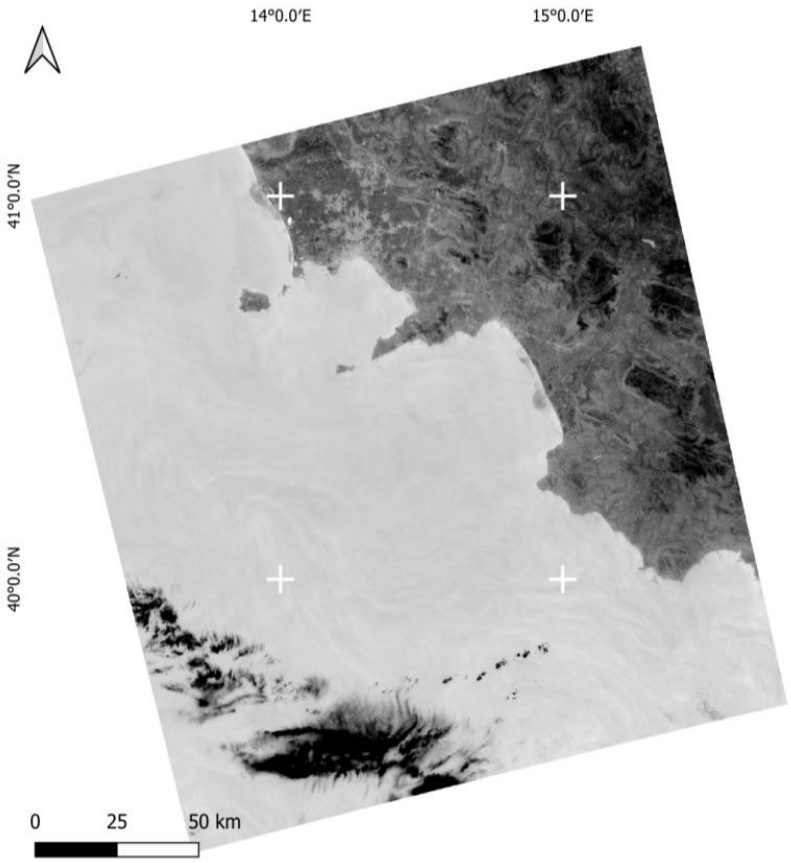

Figure 4. Landsat 8 image acquired 11th April 2020; TIR band 10 is shown as example.

2.1.2 Advanced Spaceborne Thermal Emission and Reflection Radiometer (ASTER)

The ASTER sensor launched in December 1999 is one of the five instruments on the Terra satellite, part of NASA's Earth Observing System (EOS). Terra follows a sun-synchronous nearly polar orbit with an equator crossing time of ~10:30 am/pm. The ASTER instrument has a 60 km swath width, which allows any point on the surface to be imaged at least once every 16 days. This sensor has 14 spectral bands including three in the VNIR region (0.5 to 1.0 μm) with 15 m spatial resolution, six in the shortwave infrared (SWIR) region (1.0 to 2.5 μm) with 30 m spatial resolution, and five within the thermal infrared (TIR) region (8 to 12 μm) with 90 m spatial resolution [19, 20, 21]. Unfortunately, ASTER SWIR detectors are no longer functioning due to anomalously high SWIR detector temperatures and for this reason ASTER SWIR data acquired since April 2008 are not useable. VNIR and TIR data continue to show excellent quality, meeting all mission requirements and specifications. ASTER is the first orbital sensor that provides publicly-available high-spatial resolution data with more than two bands in the TIR region. These data provide the ability to develop new methods for extracting the small scale compositional and temperature structure of the surface [22, 23, 24].

In Table 3 the ASTER band features are reported, while in Figure 5 an example of image acquired by ASTER in the TIR band 10 is shown.

Instrument	**VNIR**		**SWIR**		**TIR**	
Bands and Spectral Range (μm)	1	0.52-0.60	4	1.60-1.70	10	8.125-8.475
	2	0.63-0.69	5	2.145-2.185	11	8.475-8.825
	3N	0.78-0.86	6	2.185-2.225	12	8.925-9.275
			7	2.235-2.285	13	10.25-10.95
			8	2.295-2.365	14	10.95-11.65
			9	2.360-2.430		
Spatial Resolution	15 m		30 m		90 m	
Swath Width	60 km		60 km		60 km	
Cross Track Pointing	±318 km(±24 deg)		±116 km(±8.55 deg)		±116 km(±8.55 deg)	
Quantisation (bits)	8		8		12	
Revisit Time (days)	16		16		16	

Table 3. ASTER instrument characteristics [20].

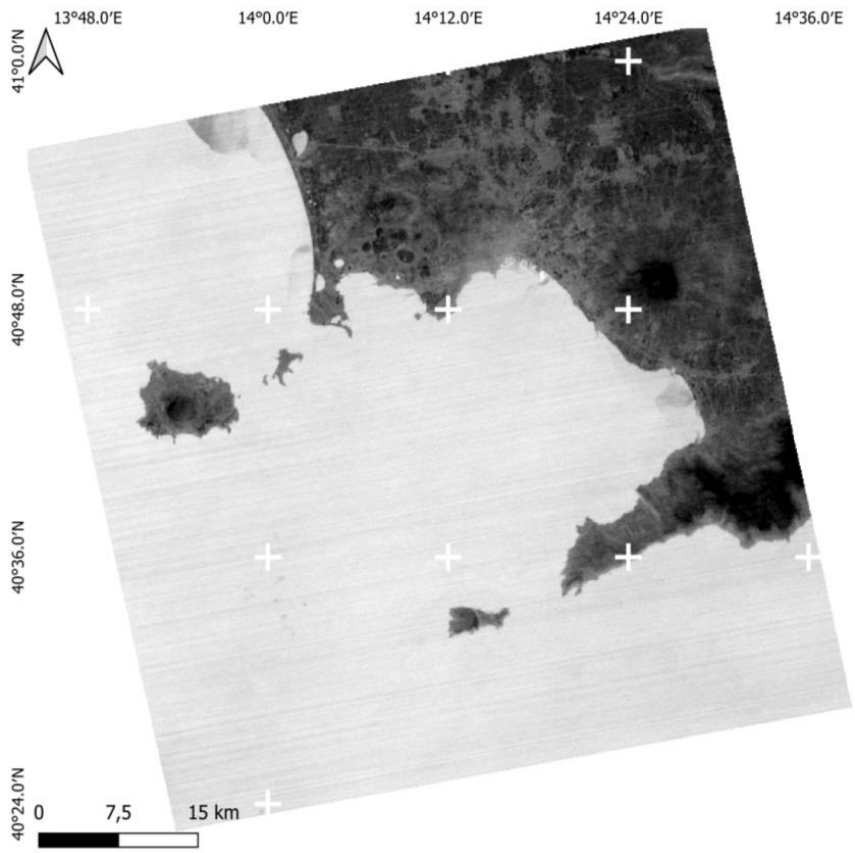

Figure 5. Example of TIR channel (band 10) nighttime ASTER image acquired 17th October 2019 on Campania region, Italy.

2.2 References of chapter 2

11. Philpot, W. D., & Philipson, W. R. (2012). Remote sensing fundamentals. In chapter 10 Passive Microwave. Cornell University.
12. Duan, S. B., Han, X. J., Huang, C., Li, Z. L., Wu, H., Qian, Y., ... & Leng, P. (2020). Land Surface Temperature Retrieval from Passive Microwave Satellite Observations: State-of-the-Art and Future Directions. Remote Sensing, 12(16), 2573.
13. Fisher, J. B., Hook, S., Allen, R., Anderson, M., French, A., Hain, C., ... & Wood, E. (2014, December). The ECOsystem Spaceborne Thermal Radiometer Experiment on Space Station (ECOSTRESS): Science motivation. In Proceedings of the American Geophysical Union (AGU) Fall Meeting, San Francisco, CA, USA (pp. 15-19).
14. Fisher, J. B., Hook, S., Allen, R., Anderson, M. C., French, A. N., Hain, C., ... & Wood, E. F. (2015, December). ECOSTRESS: NASA's next-generation mission to measure evapotranspiration from the International Space Station. In AGU Fall Meeting Abstratcs; AGU: Washington, DC, USA.
15. ECOSTRESS. Available online: https://ecostress.jpl.nasa.gov/ (accessed on 29 April 2021).

16. ECOSTRESS product description available online https://lpdaac.usgs.gov/products/eco1bmapradv001/ (accessed on 29 April 2021).
17. Roy, D. P., Wulder, M. A., Loveland, T. R., Woodcock, C. E., Allen, R. G., Anderson, M. C., ... & Scambos, T. A. (2014). Landsat-8: Science and product vision for terrestrial global change research. Remote sensing of Environment, 145, 154-172.
18. Landsat 8. Available online https://landsat.gsfc.nasa.gov/landsat-8/ (accessed on 29 April 2021).
19. Fujisada, H., Sakuma, F., Ono, A., & Kudoh, M. (1998). Design and preflight performance of ASTER instrument protoflight model. IEEE Transactions on Geoscience and Remote Sensing, 36(4), 1152-1160.
20. Yamaguchi, Y., Kahle, A. B., Tsu, H., Kawakami, T., & Pniel, M. (1998). Overview of advanced spaceborne thermal emission and reflection radiometer (ASTER). IEEE Transactions on geoscience and remote sensing, 36(4), 1062-1071.
21. Kahle, A. B., Palluconi, F. D., Hook, S. J., Realmuto, V. J., & Bothwell, G. (1991). The advanced spaceborne thermal emission and reflectance radiometer (ASTER). International Journal of Imaging Systems and Technology, 3(2), 144-156.
22. Ramsey, M. S. (2002). Ejecta distribution patterns at Meteor Crater, Arizona: On the applicability of lithologic end-member deconvolution for spaceborne thermal infrared data of Earth and Mars. Journal of Geophysical Research: Planets, 107(E8), 3-1.
23. Carter, A. J., & Ramsey, M. S. (2009). ASTER-and field-based observations at Bezymianny Volcano: Focus on the 11 May 2007 pyroclastic flow deposit. Remote Sensing of Environment, 113(10), 2142-2151.
24. Ramsey, M., & Dehn, J. (2004). Spaceborne observations of the 2000 Bezymianny, Kamchatka eruption: the integration of high-resolution ASTER data into near real-time monitoring using AVHRR. Journal of Volcanology and Geothermal Research, 135(1-2), 127-146.

3 AREAS OF STUDY AND DATA

The *Solfatara-Campi Flegrei* area, near Naples, and the *Parco delle Biancane* area (*Grosseto*), in Tuscany are the studied areas, along with *Modena* city (Figure 6). The first site is important for the presence of active volcano, the second for geothermal resource exploration, while the third is suitable for UHI analysis.

Figure 6. The three selected test sites represented by pins (credits Google Earth).

In Figure 7 the high temperature convective system of Italy is reported in orange, underlining the two investigates areas (*Solfatara-Campi Flegrei* and Tuscany) where the geothermal fields are present.

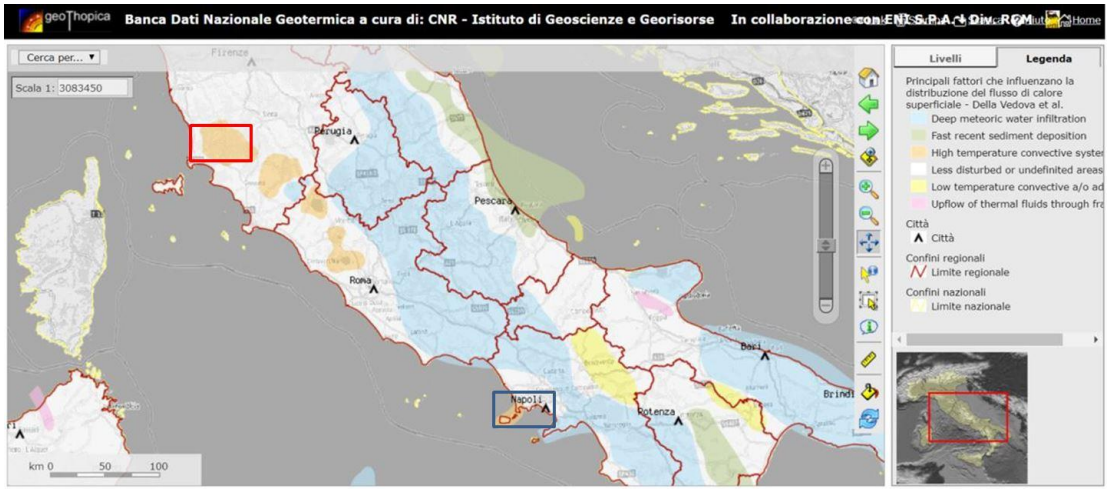

Figure 7. Geothermal test sites (http://palici.igg.cnr.it/wm_geothopica/map.phtml). Blue box includes *Solfatara-Campi Flegrei* area; red box includes geothermal area in Tuscany where *Parco delle Biancane* is located.

3.1 Areas of study

3.1.1 *Solfatara* and *Campi Flegrei* (Naples, Italy)

Solfatara crater is part of the *Campi Flegrei* volcanic complex (Figure 8) that contains fumarolic areas, whose activity is mainly from the emission of steam and gases with high sulphur component [25]. It is located within an area densely populated and historically had different periods of activity; the latest explosive activity dates back to 1538 (origin of *Monte Nuovo*). The *Solfatara-Campi Flegrei* is also characterized by periodically bradyseism whose most recent crisis are those of 1969-1972 and 1982-1984 [26]. During the latter period a maximum lift height of about 1.8 m and several thousands of shallow earthquakes (<4 km) were recorded and caused the evacuation of about 400,000 people [27]. Coinciding with this period of uplift the opening of a fracture has also been observed it is oriented towards approximately NE-SW, about 0.7 m wide within the *Solfatara* itself. Since 2005, after 20 years long phase of subsidence, this area has been raising again with a slower rate and with a total maximum vertical displacement of about 39 cm [28].

The *Solfatara* volcano is continuously monitored by Istituto Nazionale di Geofisica e Vulcanologia (INGV, Italy) through permanent network of stations and field campaigns. In particular, permanent and automatic infrared thermal cameras acquire images in areas where portion of the steam heated hot soils of *Solfatara* volcano are present measuring the surface temperature. For this reason, this site can be considered a suitable site for the validation activity of the present work [28, 29].

The permanent network of stations have been selected (Figure 9) as references for the validation:

- SF1 and SF2: *Solfatara* 1 and *Solfatara* 2 (Long: 14.139693 E, Lat: 40.829209 N);
- OBN: *Olibano*: (Long: 14.142552 E, Lat: 40.823609 N);
- PS1: *Pisciarelli* (Long: 14.147061 E, Lat: 40.828930 N);
- SOB: *Solfatara OB* (Long: 14.147061 E, Lat:4 0.826754 N).

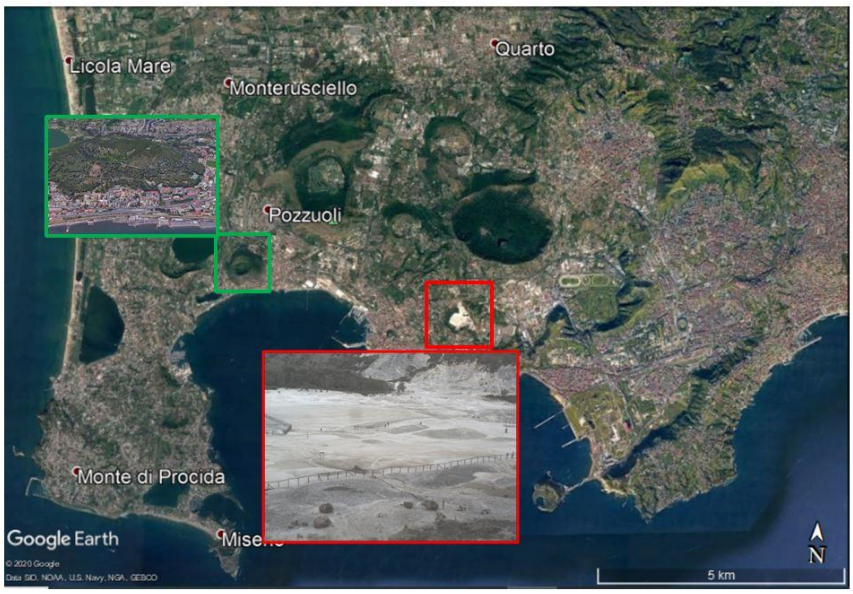

Figure 8. *Campi Flegrei* area: in the red box the *Solfatara* volcano with a particular of the area, in green box the *Monte Nuovo* (credit Google Earth and Silvestri for the *Solfatara* photo).

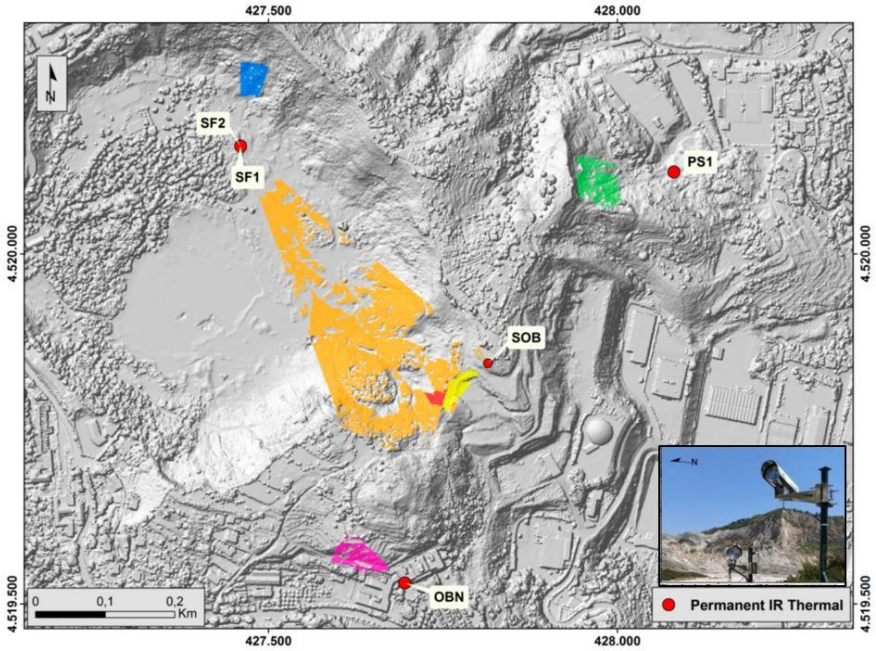

Figure 9. Location permanent stations at *Solfatara-Campi Flegrei*. SF1 = *Solfatara* Station 1; SF2 = *Solfatara* Station 2; SOB = *Solfatara* OB Station; OBN = *Olibano* Station; PS1 = *Pisciarelli* Station. In the box, picture of the TIRNet station site inside *Solfatara* crater (SF1 and SF2), composed of two TIR cameras pointing towards two different anomaly areas (modified after [30]).

3.1.2 *Parco delle Biancane* (Grosseto, Italy)

Parco delle Biancane is located in central Italy (near *Grosseto*), in a steam dominated geothermal field [31]. It has an extension of about 1 km wide by 2 km long and near a strong and wide thermal anomaly that characterizes most of the Tuscany region (Figure 10). In the area where *Parco delle Biancane* is located, a large number of studies relate to the structural analysis and geological features of the geothermal reservoirs used for heat and electricity. In literature, there are several works on modeling and measurements of the deep geothermal field [32-35] but there is a lack in the characterization of surface thermal signatures of *Parco delle Biancane* and this can filled up with this thesis.

The *Larderello–Travale* geothermal system, known as Larderello geothermal field (of which *Parco delle Biancane* is part), is the site of a large-scale steam-dominated geothermal anomaly. In this area superheated steam is present at depths over 3.5 km and with temperatures exceeding 350 °C, whereas the deep reservoir of the mount *Amiata* geothermal fields is in a two-phase (liquid + vapour mixture) state with temperatures of 300–350 °C [36].

The different geological assets and thermal behavior of these areas correspond to surface thermal anomalies that may be very different both for the maximum temperatures and for the size and distribution on the ground. In this context, systematic global cataloging of thermal anomalies as measured from high spatial resolution space borne sensors [1] are still in their infancy.

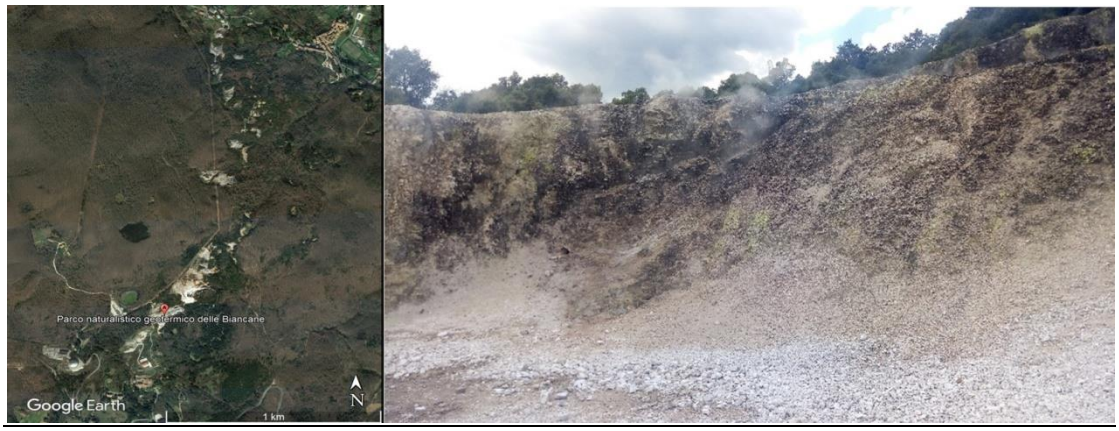

Figure 10. Test site: left, *Parco delle Biancane* (Monterotondo Marittimo, Grosseto); right, presence of fumaroles in the test site.

3.1.3 *Modena* city

The study area for the UHI analysis corresponds to the city of *Modena* and parts of its suburbs.

Modena city, about 180000 inhabitants, is located in the north of Italy, in the Po Valley. Po Valley is characterized by a high population density, is highly

industrialized and is interested by intensive agriculture [37]. The climate of this city is continental with hot summers and cold and wet winters. Considering its medium-size, its geographical position and climate, *Modena* city offers a good opportunity to test the methodology presented above.

In this area the air temperature measured at 2 meters of height acquired by four meteorological stations have been selected as references for the analysis (Figure 11):

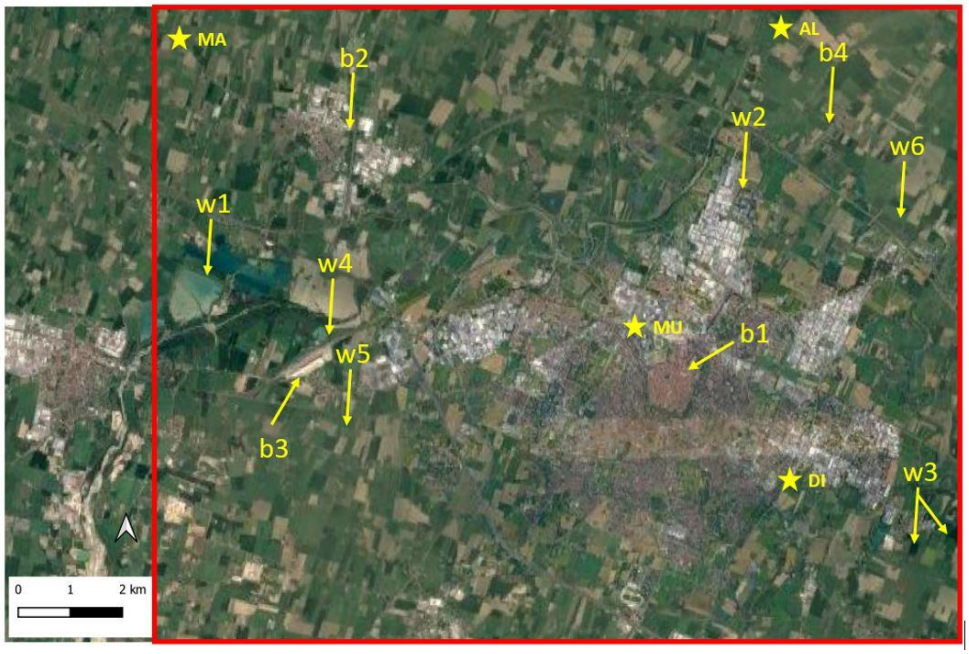

Figure 11. Red box: studied area. Stars indicate weather stations: AL-*Albareto*, MU-*Modena Urbana*, DI-DIEF campus, MA-*Marzaglia*. Waters: w1, *Secchia* river natural reserve (lakes); w2-*Modena* sewage treatment tanks; *Panaro* river natural reserve (lakes); w4 and w5, artificial pounds. Built: b1, *Modena* historic center; b2; *Campogalliano* town; b3, freight yard/storage area; b4; *Albareto* town.

- MU: Weather station located in the urban area of *Modena* (Long: 10.916985 E, Lat: 44.656392 N) [38];
- DI: University of Modena and Reggio Emilia Department "Enzo Ferrari" (DIEF), located in the east suburbs of *Modena* (Long: 10.95051667 E, Lat: 44.62826667 N);
- AL: *Albareto*: located in the north area surrounding *Modena* (Long: 10.956703 E, Lat: 44.702144 N);
- MA: *Marzaglia*: located in the west rural area surrounding *Modena* (Long: 10.806014 E, Lat: 44.702144 N)

The weather stations are managed by Geophysical Observatory of the University of Modena and Reggio Emilia [39].

3.2 Data

The analysis carried out on the studied areas have been done using:

- *Solfatara-Campi Flegrei*:
  - ASTER TIR and Landsat 8/TIRS imagery. 40 ASTER images, 55 Landsat/TIRS images, both acquired between September 2013 and December 2019;
  - TIR images acquired by permanent thermal cameras installed in *Solfatara* volcano (described in 3.1.1).

- *Parco delle Biancane*:
  - ASTER TIR and Landsat 8/TIRS imagery. 20 ASTER images acquired between May 2002 and February 2020, 40 Landsat 8/TIRS images, both acquired between September 2013 and February 2020
  - TIR images acquired by thermal cameras mounted on drone and collected during three separated field campaigns (described in 4.6).

- *Modena* city:
  - Landsat 8/TIRS imagery. 43 image acquired between September 2014 and September 2019.
  - Air temperature measured at the 4 stations around *Modena* city (*Albareto*, *Marzaglia*, University of Modena and Reggio Emilia Department "Enzo Ferrari" and weather station located in the urban area of *Modena* (described in 3.1.3)).

For all satellite data, the atmospheric soundings have been downloaded from the University of Wyoming [40]. These data are necessary for the surface temperature retrieving that will be better described in chapter 4.

Since Landsat 8 TIRS data are delivered in quantized and scaled Digital Numbers (DN), the images acquired in the band 10 (B_{10}) have been extracted and converted to Top Of Atmosphere (TOA) radiance by using the radiometric calibration equation [41]:

$$L_{TOA} = M_L \cdot DN + A_L$$

where:

L_{TOA} is the TOA radiance in $W\ m^{-2}sr^{-1}\mu m^{-1}$;

$M_L$is the multiplicative rescaling factor ($3.342 \cdot 10^{-4} W\ m^{-2}sr^{-1}\mu m^{-1}$) for Landsat 8 B_{10} ;

$A_L$is the additive rescaling factor ($0.1\ W\ m^{-2}sr^{-1}\mu m^{-1}$) for Landsat 8 B_{10} .

M_L and A_L are furnished in the metadata file of the images.

3.3 References of chapter 3

25. Chiodini, G., Avino, R., Caliro, S., & Minopoli, C. (2011). Temperature and pressure gas geoindicators at the Solfatara fumaroles (Campi Flegrei). Annals of Geophysics, 54(2).
26. Del Gaudio, C., Aquino, I., Ricciardi, G. P., Ricco, C., & Scandone, R. (2010). Unrest episodes at Campi Flegrei: A reconstruction of vertical ground movements during 1905–2009. Journal of Volcanology and Geothermal Research, 195(1), 48-56.
27. Barberi, F., Corrado, G., Innocenti, F., & Luongo, G. (1984). Phlegraean Fields 1982–1984: brief chronicle of a volcano emergency in a densely populated area. Bulletin volcanologique, 47(2), 175-185.
28. Bollettino Campi_Flegrei_2020 https://www.ov.ingv.it/ov/bollettini-mensili-campania/Bollettino_Mensile_Campi_Flegrei_2020_11.pdf (accessed on 29 April 2021)
29. Silvestri, M., Cardellini, C., Chiodini, G., & Buongiorno, M. F. (2016). Satellite-derived surface temperature and in situ measurement at Solfatara of Pozzuoli (Naples, Italy). Geochemistry, Geophysics, Geosystems, 17(6), 2095-2109.
30. Caputo, T., Cusano, P., Petrosino, S., Sansivero, F., & Vilardo, G. (2020). Spectral analysis of ground thermal image temperatures: what we are learning at Solfatara volcano (Italy). Advances in Geosciences, 52, 55-65.
31. Saccorotti, G., Piccinini, D., Zupo, M., Mazzarini, F., Chiarabba, C., Agostinetti, N. P., ... & Bagagli, M. (2014). The deep structure of the Larderello-Travale geothermal field (Italy) from integrated, passive seismic investigations. Energy Procedia, 59, 227-234.
32. Di Filippo, M., Lombardi, S., Nappi, G., Reimer, G. M., Renzulli, A., & Toro, B. (1999). Volcano–tectonic structures, gravity and helium in geothermal areas of Tuscany and Latium (Vulsini volcanic district), Italy. Geothermics, 28(3), 377-393.
33. Della Vedova, B., Vecellio, C., Bellani, S., & Tinivella, U. (2008). Thermal modelling of the Larderello geothermal field (Tuscany, Italy). International Journal of Earth Sciences, 97(2), 317-332.

34. Batini, F., Brogi, A., Lazzarotto, A., Liotta, D., & Pandeli, E. (2003). Geological features of Larderello-Travale and Mt. Amiata geothermal areas (southern Tuscany, Italy). Episodes, 26(3), 239-244.
35. Bellani, S., Brogi, A., Lazzarotto, A., Liotta, D., & Ranalli, G. (2004). Heat flow, deep temperatures and extensional structures in the Larderello Geothermal Field (Italy): constraints on geothermal fluid flow. Journal of Volcanology and Geothermal Research, 132(1), 15-29.
36. Barelli, A., Ceccarelli, A., Dini, I., Fiordelisi, A., Giorgi, N., Lovari, F., & Romagnoli, P. (2010, April). A review of the Mt. Amiata geothermal system (Italy). In Proceedings world geothermal congress (Vol. 2010, pp. 1-4).
37. Barbieri, T., Despini, F., & Teggi, S. (2018). A multi-temporal analyses of Land Surface Temperature using Landsat-8 data and open source software: The case study of Modena, Italy. Sustainability, 10(5), 1678.
38. Osservatorio Geofisico. Available online: http://meteo.unimore.it/meteo/ (accessed on 29 April 2021).
39. Magli, S., Lodi, C., Lombroso, L., Muscio, A., & Teggi, S. (2015). Analysis of the urban heat island effects on building energy consumption. International Journal of Energy and Environmental Engineering, 6(1), 91-99.
40. Atmospheric profile Web Site: http://weather.uwyo.edu/upperair/sounding.html (accessed on 29 April 2021).
41. Landsat 8 Data User Handbook available on line https://www.usgs.gov/media/files/landsat-8-data-users-handbook (accessed on 29 April 2021).

4 LAND SURFACE TEMPERATURE (LST) FROM SATELLITE

Satellite sensors measure TOA radiances from which it is possible to obtain the corresponding TOA brightness temperatures. In the TIR region of the electromagnetic spectrum, brightness temperature is also known as equivalent blackbody temperature T_B. In the 10-12 μm region, the difference between these temperatures ranges generally from 1 to 5 K depending on the atmospheric conditions [42]. The atmospheric effect varies with the vertical temperature and humidity profiles. LST can be retrieved from observed T_B using various algorithms which account for the atmospheric effect and for the surface spectral emissivity. Surface temperature is an important quantity for many environmental models, e.g. energy and water exchange between atmosphere and surface, numerical weather prediction, global ocean circulation, climatic variability, etc. [43]. Only by remote sensing from satellites it is possible to measure LST on a regional or global scale.

4.1 Radiative Transfer Equation

The Radiative Transfer Equation (RTE) in the TIR range is based on the following assumptions: (a) the atmosphere is at local thermodynamic equilibrium, which is approximately valid up to about 50-70 km [44], (b) no scattering occurs, which means only cloud free and non-hazy conditions are considered and (c) Earth's surface is a Lambertian reflector. RTE can be expressed as eq. 1:

$$L_{\lambda\theta}^{sat} = \frac{\varepsilon_{\lambda\theta}\,\tau_{\lambda\theta} B_\lambda(T_S)}{\pi} + L_{\lambda\theta}^{\uparrow} + [1 - \varepsilon_{\lambda\theta}\,]\tau_{\lambda\theta}\, L_\lambda^{\downarrow} \qquad (1)$$

where all quantities refer to a spectral integration over the band width of band λ (central wavelength), ε is the surface emissivity, τ is the total transmission of the atmosphere (transmissivity), B is the radiance emitted by a blackbody, that is the Planck's function (eq. 2), T_s is the LST, $L_\lambda^{\uparrow}$ is the up-welling atmospheric radiance, θ is the zenith observation angle, $L_\lambda^{\downarrow}$ is downwelling atmospheric irradiance divided by π.

$$B(\lambda, T) = \frac{c_1}{\lambda^5[exp(c_2/\lambda T) - 1]} \qquad (2)$$

where:

B(λ,T) spectral excitance of a black body ($Wm^{-2}\mu m^{-1}$) (Planck's function),

λ wavelength (μm),

T temperature (K),

c1 = 3.7411 x 10^{8}W μm^{4} m^{-2},
c2 = 1.4388 x 10^{4} μm K.

The first term of eq. 1 denotes the emission from the surface, and is least affected by the atmosphere in an atmospheric window; the second term of eq. 1 varies strongly with the vertical structure of the atmosphere – warm/moist layers increase this contribution; the third term describes the reflection of downwelling radiation.

However, most natural objects are non-black bodies ($0 < \varepsilon(\lambda) < 1$), where the spectral emissivity ε(λ) is the ratio between the radiance emitted by an object at wavelength λ and that emitted by a black body at the same temperature. For non-black bodies, Planck's function of eq. 2 is multiplied by ε(λ), [45] as reported by eq. 3:

$$L\,(\lambda,T) = \varepsilon(\lambda)\,B(\lambda,T) = \varepsilon(\lambda)\frac{c_1}{\lambda^5[exp(c_2/\lambda T)-1]} \qquad (3)$$

where $L(\lambda,T)$ spectral radiance of a non-black body ($Wm^{-2}\mu m^{-1}\ sr^{-1}$),

Kirchhoff's law of radiation states that a body is as good an absorber as an emitter, this leads to:

$$\alpha(\lambda) \approx \varepsilon(\lambda) \qquad (4)$$

where α(λ) is the body absorptivity. This law holds well for systems at local thermodynamic equilibrium, i.e. the system can be characterised by a single thermodynamic temperature. If atmospheric effects (upwelling radiance and reflected downwelling irradiance) are separated, and emissivity is known, the temperature of a Lambertian reflector can be determined by reversing eq. 3:

$$T = \frac{c_2}{\lambda \, ln\left[\frac{\varepsilon(\lambda)\, c_1}{\pi\, \lambda^5\, L(\lambda)} + 1\right]} \qquad (5)$$

Different algorithms to retrieve surface temperature from mostly TIR data have been proposed in the last years. Accurate LST retrievals require a good characterization of the surface emissivity, so algorithms and methods for Land Surface Emissivity (LSE) retrieval should be also included in any discussion on optimal LST algorithms. Literature includes an exhaustive review of LST and LSE methods [46, 47] as well as an optimal selection of LST algorithms to be applied to the main TIR sensors with minimum bands configuration [48]. Main LST algorithms can be classified according to the number of TIR bands used:

a) Single-channel algorithms (SCA), using only one TIR band;
b) Two-channel (split-window) algorithms, using two TIR bands;
c) Temperature and Emissivity Separation (TES) algorithms, using three (or more) TIR bands.

One of the main differences between the LST approaches is that methods (a) and (b) require a priori knowledge of the emissivity typically from other spectral range than TIR, whereas method (c) provides both LST and LSE from TIR data.

For this study the Temperature and Emissivity Separation (TES [49], for ASTER data) and single-channel algorithm (for Landsat 8, inverting RTE of eq. 1) have been considered. In particular, even if Landsat 8 has two thermal bands, considering the USGS announced caution in the use of $Band_{11}$ of Landsat 8 due to the calibration uncertainties [50], the single-channel algorithm on $Band_{10}$ has been applied.

4.2 Atmospheric corrections

As already considered, the atmospheric correction is an important step in order to remove the effect of the atmosphere and to estimate correctly the LST. For this reason the well tested CIRILLO software [51] is used for the correction of spaceborne images acquired in the TIR spectral regions. The atmospheric terms needed by CIRILLO are computed by the radiative transfer models MODTRAN (MODerate resolution atmospheric TRANsmission) [52, 53].

Atmospheric corrections and topographic corrections of remote sensing images are very important in order to obtain reliable values for many surface

parameters (reflectance, vegetation indexes, ocean chlorophyll maps, temperature…) but represent a very difficult pre-elaboration step. The choice of methods and approaches commonly used to apply these corrections depends mainly on the spectral interval considered, on the precision of the results required, and on the complexity of the algorithms. The first factor depends on the considered electromagnetic radiating sources and on the interaction phenomena between electromagnetic waves and atmosphere modeled. The other two factors are in opposition: simple algorithms, fast and easy to use, in general produce poor atmospheric corrections, and vice versa. Difficulties facing when using powerful correction algorithms are mainly those linked to the complexity of the algorithm and those linked to the user. In the first case, difficulties are due to the fact that often the algorithms are based on the use of radiative transfer models, that often consist on software not easy to use. Moreover, often the user does not have specific knowledge of the physical phenomena and of the mathematical modelling involved: this generates the second kind of difficulties. On the basis of the above mentioned aspects, a procedure that makes use of radiative transfer modelling but, at the same time, it is use friendly has been developed [51].

The spectral values of atmospheric terms, i.e. transmittances, reflectance contribution due to solar radiance scattered by the atmosphere and downward spherical albedo of the atmosphere, are computed using the radiative transfer models MODTRAN, embedded in CIRILLO. MODTRAN is used to evaluate absorption effects of gaseous constituent of the atmosphere. Moreover, the effect of the altitude is corrected by using a Digital Elevation Model (DEM).

Correcting Earth Observation (EO) spaceborne remote sensed data the variability of sensor viewing angles is negligible; this assumption can be considered acceptable for most of satellite borne sensor, for which CIRILLO has been done, but it is very questionable for sensor on board of airplane.

The atmospheric profiles, used in CIRILLO, in terms of pressure, temperature, geopotential height, relative humidity needed for obtaining the atmospheric components were downloaded from the University of Wyoming (WYO) website [40].

4.3 Temperature and Emissivity Separation (TES) technique for ASTER data

The TES algorithm was originally designed for application with the ASTER instrument, with five TIR bands [49]. It estimates land surface emissivity ε_i and

temperature T_S from land leaving radiance and down-welling atmospheric irradiances, related by the following eq. 6:

$$L_i = \varepsilon_i B_i(T_S) + [1 - \varepsilon_i]L_i^{\downarrow} \quad (6)$$

In order to decouple temperature and emissivity, the TES algorithm uses a semi-empirical relation determined from laboratory spectra, between the minimum emissivity and spectral contrast (maximum – minimum difference, MMD). Taking into account that L_i and $L_i^{\downarrow}$ are the input data, from an initial value of emissivity it is possible to obtain a first value for LST (Figure 12).

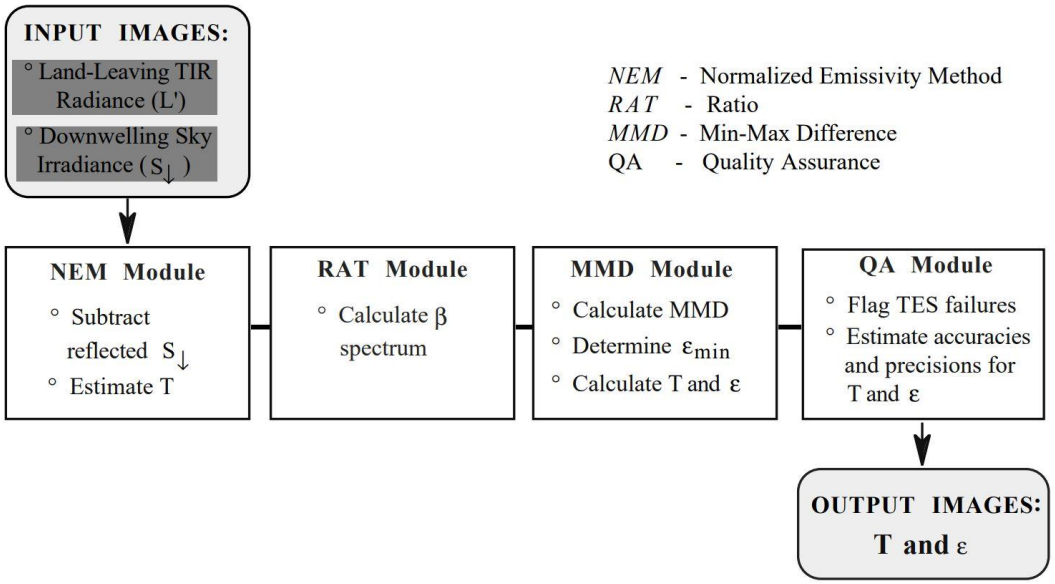

Figure 12. Basic design of the TES algorithm [54].

In fact, for N TIR bands, N different values will be obtained for T_s by inversion of Planck's law in Eq. 3. The final value for T_s is chosen as the maximum value between the N different values. Then, T_s can be used again in Eq. 6 and obtain the emissivity values for the N TIR bands. This methodology can be repeated again in order to obtain another value for T_s and other emissivity values. The described iterative procedure is called as NEM (Normalized Emissivity Method) module, and constitutes itself a method for retrieving surface emissivities and temperature [55]. To obtain more accurate emissivity values, another two modules are applied: the RATIO and the MMD (Maximum-Minimum Difference) modules.

The RATIO module obtains relative emissivities (ε_i) by rationing the NEM emissivities to their average value:

$$\beta_i = \frac{\varepsilon_i}{\frac{1}{N}\sum_{i=0}^{N}\varepsilon_i} \quad (7)$$

whereas in the MMD module final emissivity values are obtained according to the following expression:

$$\varepsilon_i = \beta_i \left(\frac{\varepsilon_i}{\min(\beta_i)}\right) \quad (8)$$

The min is the minimum emissivity obtained from the following empirical relationship:

$$\varepsilon_{min} = 0.994 - 0.687\ MMD^{0.737} \quad (9)$$

with MMD the spectral contrast calculated as

$$MMD = \max(\beta_i) - \min(\beta_i) \quad (10)$$

Note that Equation was obtained for ASTER characteristics from different laboratory spectra (86 samples), and it needs to be recalculated for other sensors. The TES method is capable of recovering surface emissivity within about 0.015 and surface temperatures within about 1.5 K. A detailed description of the algorithm is given in [49].

The performance of the TES algorithm was initially evaluated through extensive numerical simulation, and after launch by comparison to selected field sites. In simulations the TES algorithm was able to retrieve to within an accuracy of 1.5 K in 95% of the spectral library materials for a surface at 300 K [49]. The emissivity errors were found co-dependently with the LST, in the case of a surface at 300 K and a 1 K LST overestimate was found to correspond to an emissivity underestimate of around 0.017 [56]. Overall the numerical simulations showed a performance across the majority of tests comparable to the design specifications of ±1.5 K and ±0.015 emissivity, which are often the values quoted when looking at the uncertainty of the TES product [57].

4.4 Single channel algorithm (SCA) for Landsat 8 data

The previous described TES method is not operational to obtain surface emissivity for Landsat data due to the limitations presented in many studies, such as the requirement of more than two TIR bands [58-63] (Landsat/TIRS has only two bands). As already considered in 4.1, due to the USGS announced caution in the use of $Band_{11}$ of Landsat 8 due to the calibration uncertainties [50], the single-channel algorithm on $Band_{10}$ has been applied.

The radiance acquired by TIR sensor of Landsat 8 is used to evaluate the surface temperature by Planck's equation after applying the radiometric calibration to convert the digital number first and the atmospheric corrections later. While the radiometric calibration is obtained following [41] in terms of TOA radiance, the atmospheric correction is necessary to retrieve the emitted radiance by removing the atmospheric transmission effect and the down welling and upwelling radiances. To remove these effects atmospheric corrections described in 4.2 are applied. Moreover, since the surface emissivity is also an important variable to consider for the surface temperature retrieval, the Advanced Spaceborne Thermal Emission and Reflection Radiometer (ASTER) Global Emissivity Dataset (GED) emissivity data downloaded for free by USGS web site [64] is used. ASTER-GED land surface temperature and emissivity data products are generated using the ASTER-TES algorithm with a Water Vapor Scaling (WVS) atmospheric correction method using Moderate Resolution Imaging Spectroradiometer (MODIS) MOD07 atmospheric profiles and the MODTRAN radiative transfer model [52, 53]. This dataset is computed from all clear-sky pixels of ASTER scenes acquired from 2000 through 2008 [65] and has a spatial resolution of 100 meters [66]. For this study, considering that Landsat 8 data are delivered at 30 m but acquired at 100 m, ASTER-GED emissivity is opportunely resized to the Landsat 8 pixel spatial resolution.

4.5 LST Time Series data analysis

In the next paragraphs the time series considered for this study are reported. The classical definition of time series is: "a set of regular time-ordered observations of a quantitative characteristic of an individual or collective phenomenon taken at successive, in most cases equidistant, periods / points of time". According to this sentence, it seems that LST time series are not available because the orbiting sensors are not compliant both in terms of GSD and revisit time. In this study, it will demonstrate that the number of data acquired by ASTER and Landsat 8 are large enough to generate a very interesting

production of LST maps and series. It is interesting to see in the next sections that the ASTER time series is longer than Landsat 8 but at the same time is not continuous (missing acquisition), while Landsat 8 offers better continuity in acquisition. Moreover, LST maps, estimated both ASTER and Landsat 8, have been re-projected into the unique map projection (i.e., UTM with WGS84 datum and Zone 33N or 32N, for *Solfatara-Campi Flegrei* and *Parco delle Biancane - Modena* respectively). Then, the LST maps are co-registered to allow for accurate geographic comparisons and reduce the potential geometric errors (e.g., position and orientation) and to have a unique stack of data.

For the purpose of this analysis to eliminate temperature measurements inaccuracies due to the solar radiation, nighttime ASTER and Landsat 8 acquisitions were considered.

All LST estimated using ASTER and Landsat 8 have been co-registered and have the same pixel spatial resolution (90 m).

One important effect visible working with LST time series is the seasonality. This effect illustrates annual insolation variations and is typically modeled as a sinusoidal function (Figure 13 and Figure 15). For such reason, in the chapter 5 the PCA methodology has been used for thermal anomalies detection and the removal of seasonality from LST time series is not necessary.

4.5.1 LST on *Solfatara-Campi Flegrei* test site

For this test site ASTER and Landsat 8 cloud-masked and nighttime estimated LST have been collected. In particular for long period, from September 2013 to December 2019, 40 ASTER data and 55 Landsat 8 data have been processed and 95 LST have been estimated (Figure 13, Table 4).

Nighttime Data	Number of processed images
LST-ASTER	40
LST-Landsat 8	55
TOTAL LST	95

Table 4. LST processed for *Solfatara-Campi Flegrei* test site from 2013 to 2019.

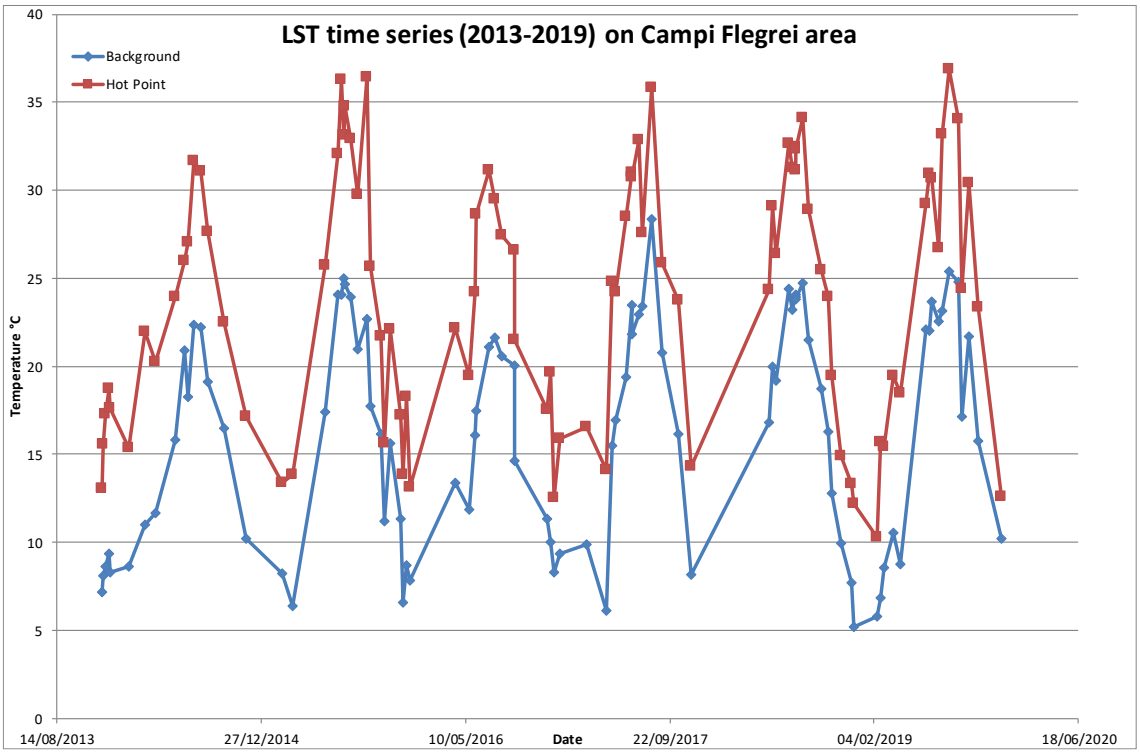

Figure 13. LST Time series on *Solfatara-Campi Flegrei* test site.

In Figure 13 two representative points, hot and background, are reported. The hot point has been selected inside the *Solfatara* caldera, near the very hot area of the volcano. The background point has been selected outside the *Solfatara* caldera, where thermal anomaly is not present (Figure 14).

In Figure 13 the seasonal behavior is easily detectable for both points: during summer high values of temperature occur, during winter low values of temperature is evident.

Once obtained the LST time series for *Solfatara* volcano, the next step was the validation of these measurements with ground measurements collected near to satellite measurements.

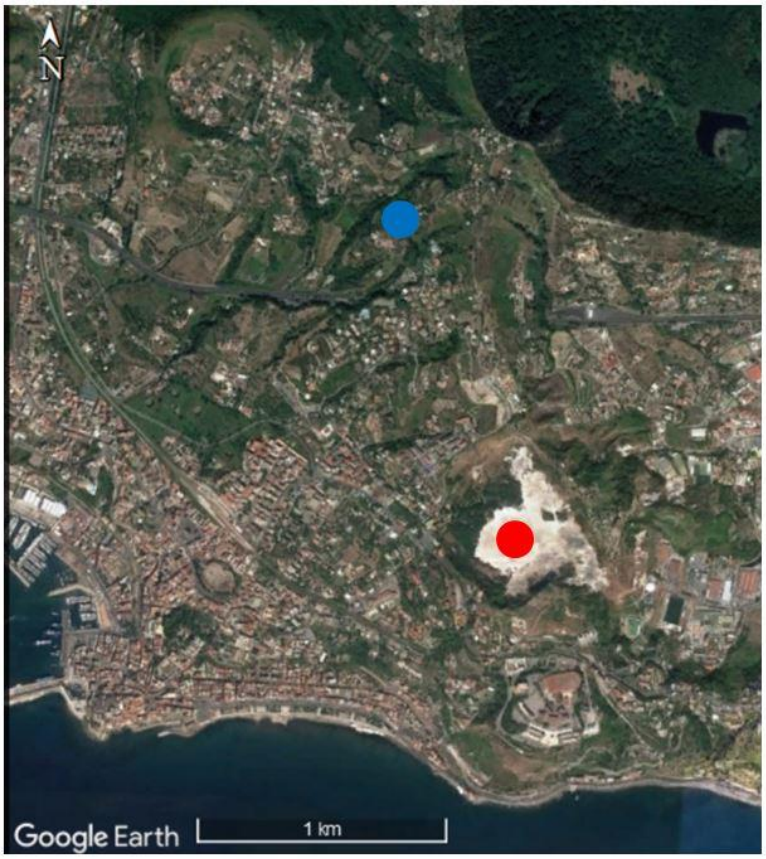

Figure 14. Hot (red) and background (blue) points selected on *Solfatara* area.

4.5.2 LST on *Parco delle Biancane* test site

For this test site ASTER and Landsat 8 estimated LST have been collected (Figure 15 and Figure 16). In particular, for a long period, from May 2002 to February 2020, 20 ASTER data and, from September 2013 to February 2020, 40 Landsat 8 data have been processed and 60 LST have been estimated (Table 5).

Nighttime Data	Number of processed images
LST-ASTER	20 (from 2002 to 2020)
LST-Landsat 8	40 (from 2013 to 2020)
TOTAL LST	60

Table 5. LST processed for *Parco delle Biancane*.

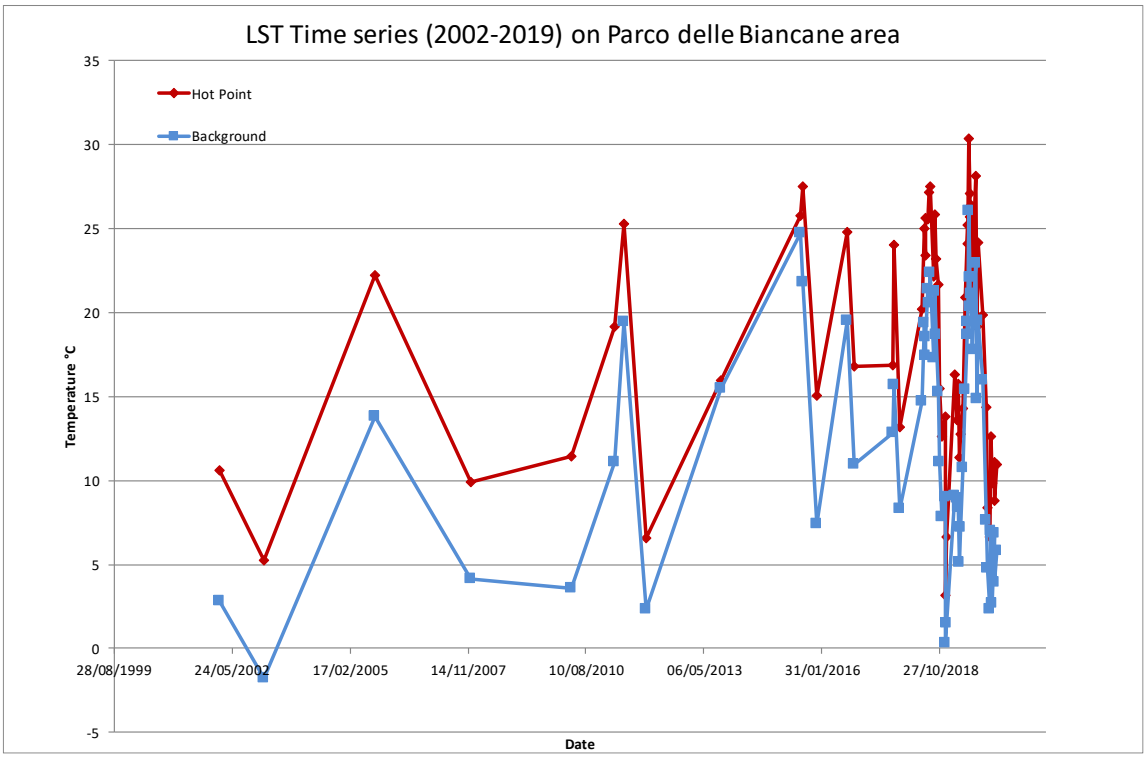

Figure 15. LST Time series on *Parco delle Biancane* test site. Zoom for 2018- 2019 is reported in Figure 16.

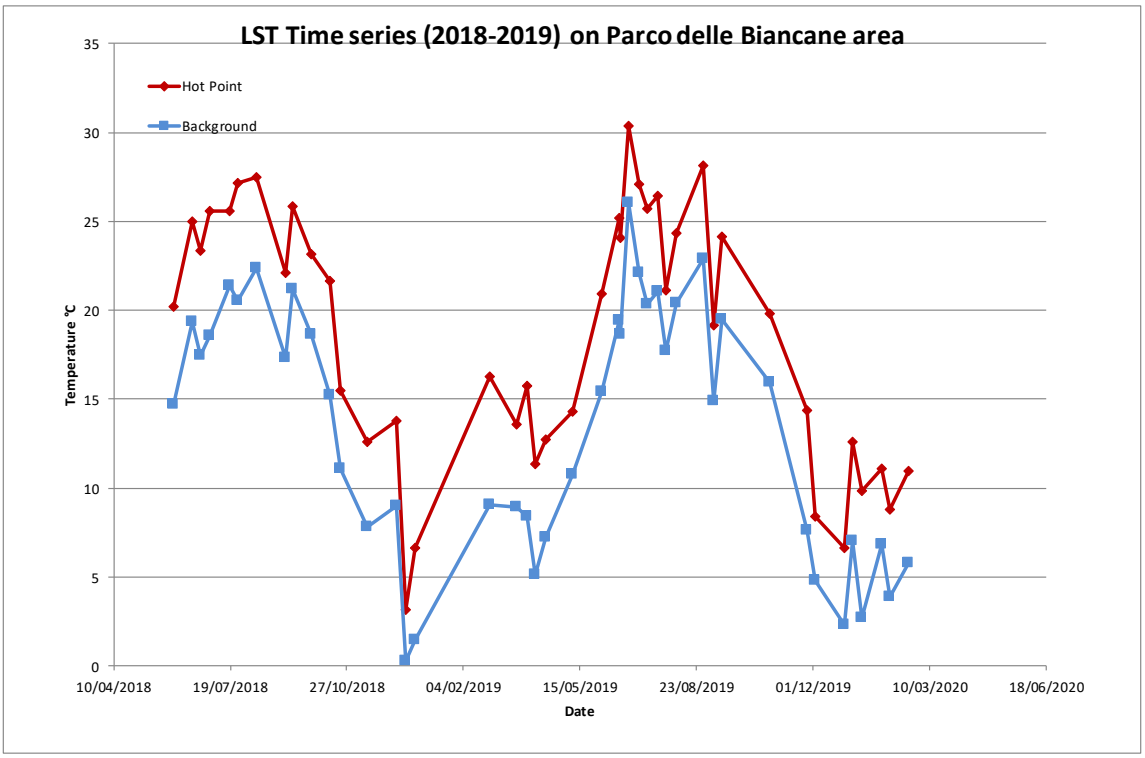

Figure 16. LST Time series on *Parco delle Biancane* test site: zoom on 2018-2019.

Also in this case, as for the *Solfatara-Campi Flegrei*, two representative points, hot and background, are reported. The hot point has been selected near the hot area of the *Parco delle Biancane*. The background point has been selected outside the *Parco delle Biancane*, where thermal anomaly is not present (Figure 17). The background area is predominantly covered by vegetation with strong presence of trees. This leads that temperature in background area is affected by the vegetation cover (i.e. cold during the summer and warm in the winter respect to soil). Despite this, the hot point (red in Figure 17) is always higher than the background (blue in Figure 17), as reported in Figure 15 and Figure 16.

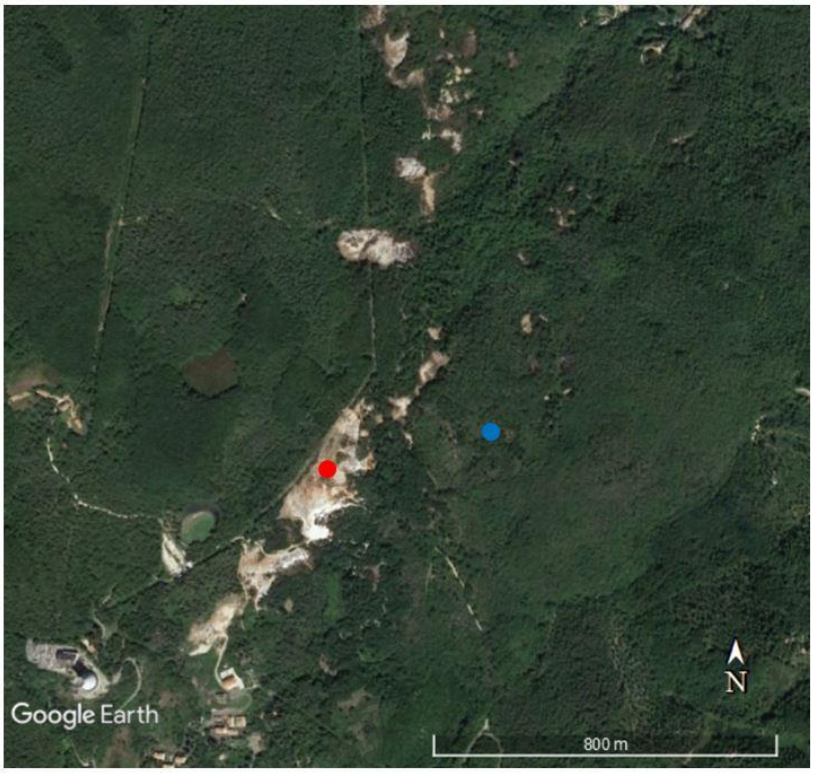

Figure 17. Hot (red) and background (blue) points selected on *Parco delle Biancane* area.

Once obtained the LST time series for *Parco delle Biancane* geothermal area, the next step was the validation of these measurements with ground measurements collected near to satellite measurements.

4.5.3 LST on *Modena* city

The methodology previously considered has been applied to investigate the UHI. This phenomenon consists on urban atmospheric temperature increase respect to the surrounding rural areas and is mainly due to growing

urbanization. Many researchers have used LST in studies concerning the UHI [67-69].

The LST Landsat 8 time series has been computed and validated using the weather stations installed in three different sites.

For this test site only nighttime and cloud masked Landsat 8 LST have been collected. This choice is due to the fact that not enough nighttime ASTER data were available to generate an available LST time series. In particular for the period from September 2014 to September 2019 43 Landsat 8 data have been processed and the for this reason 43 night time LST have been estimated (Table 6).

Nighttime Data	**N° of processed data**
LST-ASTER	Not Applicable
LST-Landsat 8	43
TOTAL LST	43

Table 6. LST processed on *Modena* site from 2014 to 2019.

Also in this case, the next step was the validation of LST time series with ground measurements collected by the meteorological stations near to satellite measurements.

4.6 Validation of LST

The relative accuracy of LST estimates can be assessed to ground measures provided by the ground network which operates independently by the satellites. In alternatively, the accuracy can be estimates by cross-validation between products obtained with different LST retrieval algorithms and/or for different sensors, even if largely complicated by the spatial scale mismatch between satellite sensors and/or ground based sensors. In fact, areas observed by ground radiometers usually cover small areas, whereas satellite measurements in the thermal infrared typically cover between 1 km^2 and 100 km^2. In this case, the ground measurements collected by fixed thermal cameras or mounted on UAV can be used for validation aims. Despite the scale difference, the good agreement obtained by comparing same areas with ground, UAV and satellite measurements offers the possibility to be confident of LST estimated by satellite for the whole acquired frame.

In the next sections the validations test of LST are described.

4.6.1 Validation of LST on *Solfatara-Campi Flegrei* area

In order to validate 95 LST estimates on *Solfatara–Campi Flegrei* area (Table 4), the permanent Thermal Infrared Surveillance Network (TIRNet) has been considered [70, 71].

The TIRNet managed by Istituto Nazionale di Geofisica e Vulcanologia – Sezione Osservatorio Vesuviano (NA) is aimed to volcanic surveillance of the Neapolitan area. In the *Solfatara-Campi Flegrei* caldera five stations are installed and they acquire daily thermal infrared frames of diffuse degassing areas characterized by significant thermal anomalies inside the *Solfatara* crater, on the southern slope of Mt. Olibano lava dome and in the *Pisciarelli* area (Figure 18 and Table 7). The infrared sensors are FLIR SC645/655 cameras, with a Focal Plane Array (FPA) uncooled microbolometer detector whose resolution is 640x480 pixel, spectral range is 7.5 - 14 μm, accuracy is ± 2 °C and thermal sensitivity is < 0.03°C @ +30°C [72].

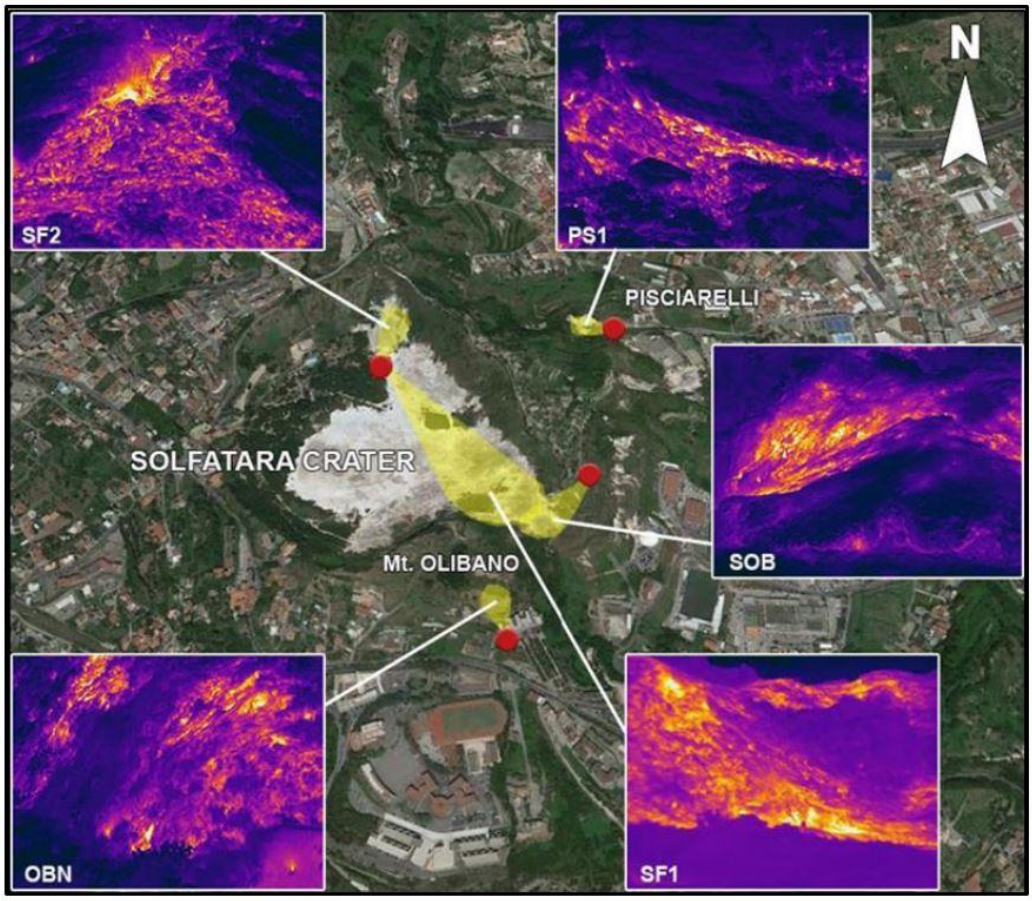

Figure 18. Location of the TIRNet permanent stations (red dots) and the investigated regions (yellow areas) with the IR frames at *Solfatara-Campi Flegrei*. SF1 = *Solfatara* Station 1; SF2 = *Solfatara* Station 2; SOB = *Solfatara* OB Station; OBN = *Olibano* Station; PS1 = *Pisciarelli* Station.

Remote Station	Camera model	Resolution (pixel)	Station UTM Coordinates (m)	Sensor-Target average distance (m)	Average pixel size (cm)
SF1	FLIR A655SC	640 x 480	X: 427.460 Y: 4.520.154	340	23.1
SF2	FLIR A645SC	640 x 480	X: 427.460 Y: 4.520.154	114	4.6
PS1	FLIR A645SC	640 x 480	X: 428.081 Y: 4.520.117	140	5.6
OBN	FLIR A645SC	640 x 480	X: 427.695 Y: 4.519.530	65	5.4
SOB	FLIR A655SC	640 x 480	X: 427.810 Y: 4.519.878	90	5.5 ÷ 6.7

Table 7. Main specifications of TIRNet stations. Refer to Figure 18 for stations' names and locations.

The TIRNet stations involved in the study are SF1, SF2, PS1, OBN and SOB (Figure 18). In order to compare the satellite and ground images it is necessary that ground images have similar field of view of satellite data. For this reason, the ground images have been orthorectified in the UTM WGS84 coordinate system using a set of Ground Control Points (GCP) identified both on the ground images and on a Digital Surface Model (DSM).

It is important to remark that the average pixel size of TIRNet has a very high resolution respect to the satellite data, less than one meter and 90 meter respectively. For this reason, to compare the spatial thermal anomalies of both ground measurements and satellite, common areas have been identified using polygons which were constructed on the basis of a regularly spaced, 30 m × 30 m large grid (that represents a good compromise for the comparison). Figure 19 shows polygons covering areas where high values of temperature are present. The average of all temperature measurements of TIRNet data included in the polygons are compared with the LST estimated with satellite data.

Time-series of temperature values inside the analysis areas were created by using the zonal statistical function (ArcGIS© algorithm [73]) which calculates the mean, minimum and maximum temperature values of the analysis areas belonging to all ground TIRNet measurements and satellite surface temperature. Figure 20 and Table 8 evidence the good agreement between mean temperature values of analysis areas in the ground TIRNet measurements and mean temperature values of the same areas in the satellite data. In particular, Pearson linear correlation coefficients (r) have been considered for agreement estimation.

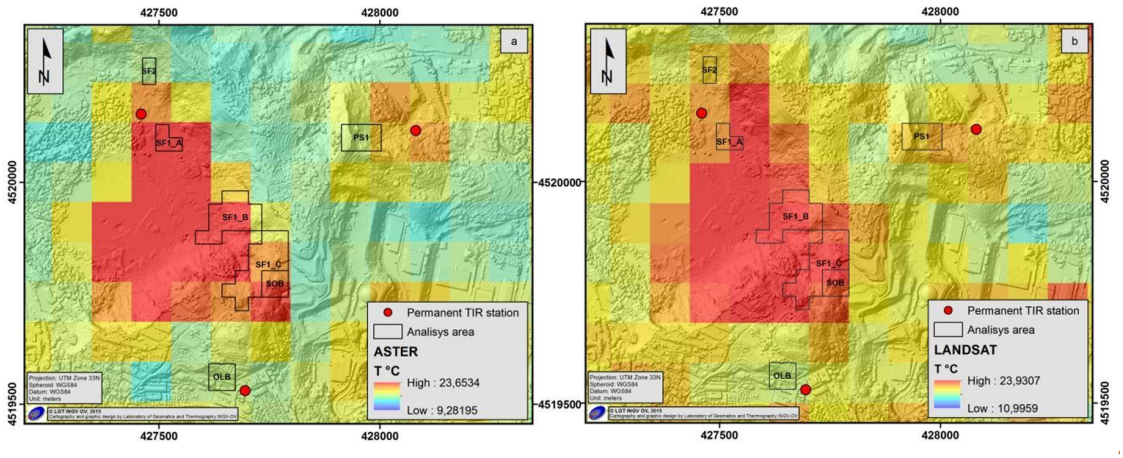

Figure 19. LST estimated by using ASTER (left) and Landsat 8 (right) on 20th June and 28th June 2019 respectively. Polygons are areas covered by TIRNet stations.

One exception is the SF2 site; in this case satellite temperatures are lower than TIRNet measurements, this is due to the high number of TIRNet measurements included in the polygon as showed in Figure 21. Moreover, in Table 8, the bias values indicating mean deviations between temperatures from satellites and TIRNet are also reported.

Areas	Landsat 8		ASTER	
	r	Bias (°C)	r	Bias (°C)
SF1_A	0.99	0.06	0.87	1.35
SF1_B	0.92	-0.65	0.88	-1.28
SF1_C	0.93	-0.20	0.91	-1.15
SOB	0.98	0.47	0.89	-0.17
PS1	0.94	-3.04	0.95	-3.04
OBN	0.98	-2.97	0.96	-2.35
SF2	0.96	-5.76	0.93	-6.07

Table 8. r and bias for comparison between satellite LST and TIRNet temperature. Positive and negative values of bias represent satellite overestimation and underestimation, respectively.

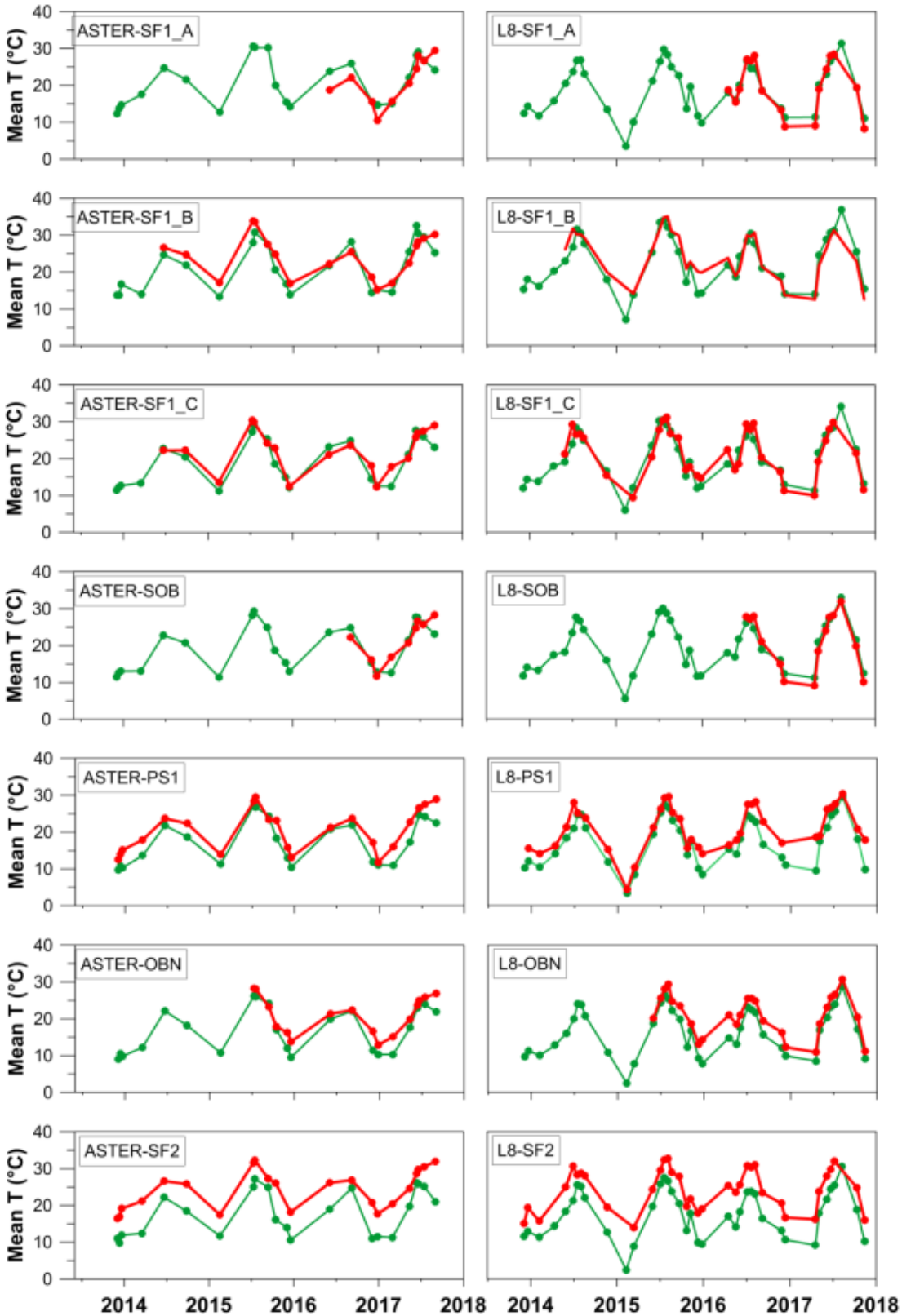

Figure 20. Comparison among temperature time series extracted from satellite and TIRNet analysis areas. Green line = mean temperature of satellite data; red line = mean temperature of TIRNet data.

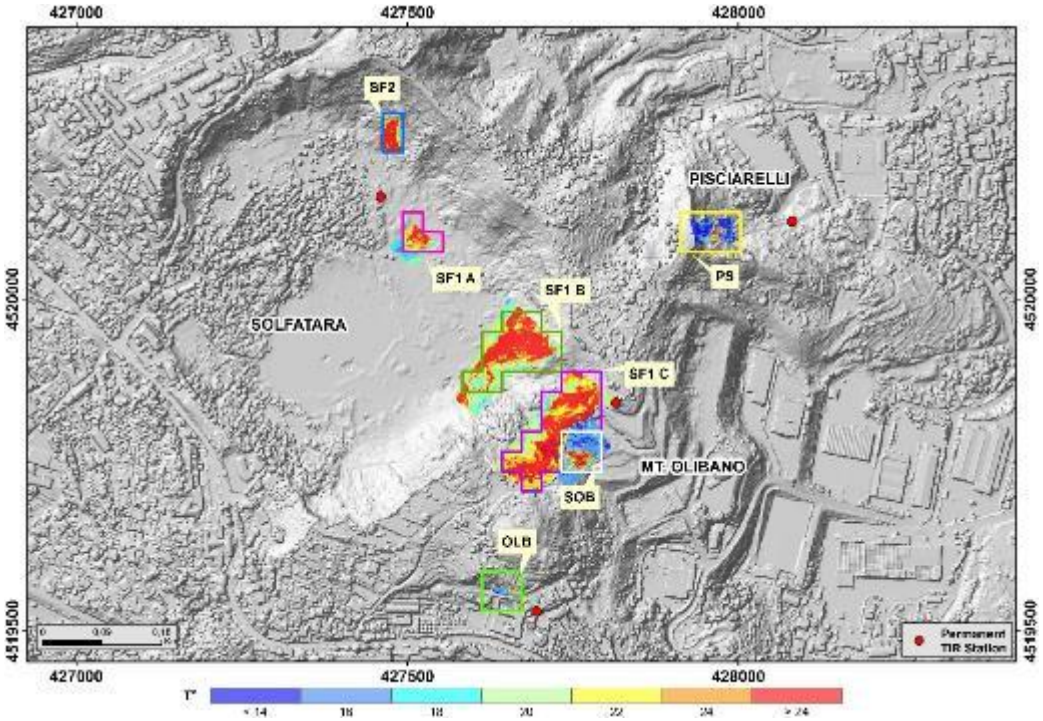

Figure 21. Main thermal anomalies detected by TIRNet. Each polygon represents the investigated area.

4.6.2 Validation of LST on *Parco delle Biancane*

In the next sub-paragraphs, three cross-comparison will be described using different sensors.

4.6.2.1 Nighttime acquisitions: UAV - Landsat 8 data

For validation on *Parco delle Biancane*, because no fixed thermal cameras were installed, in 2018 and 2019 three separated nighttime field campaigns on this test site held, in the frame of a research project of Istituto Nazionale di Geofisica e Vulcanologia (INGV-FISR 2016 Fondo integrativo speciale per la ricerca (FISR): Riparto per gli anni 2015 e 2016 a progetti di ricerca (Delibera CIPE n. 71/2016) per l'INGV: "Centro di studio e monitoraggio dei rischi naturali dell'Italia Centrale").

During these three field campaigns, surface temperatures in sync with the satellite pass were collected by a thermal camera mounted on a drone (UAV). It is important to remark that medium (UAV) to long (satellite) spatial range thermal images are affected by errors due both to the distance and to atmospheric absorption and they require to be calibrated with short range field measurements in order to accurately correct for these effects. Systematic detection and validation of thermal anomalies as measured from high spatial resolution space borne thermal sensors and acquired with thermal cameras installed on UAVs are still in their infancy [74].

A FlyBit octocopter [75] was used to carry out surveys from UAVs (Figure 22). It was equipped with a Sony Alpha 6000 camera (Figure 22A) for photogrammetric surveys and with a FLIR VUE PRO R thermal imaging camera (Figure 22B) in order to gather thermal infrared measurements.

Figure 22. FlyBit octocopter and its equipment.

Flight plan was carried out (Figure 23a) to obtain a good coverage of the investigated area (Figure 10). Flight plans were always performed in the "scheduled and assisted flight" mode [75] and were split in two phases shown in Figure 23a and Figure 23b which indicate the northern sector and the southern sector respectively. These sectors are characterized by a low elevated morphology in the south. Zenithal images were collected by using the single grid option of the autopilot software (mission planner, Figure 23a and Figure 23b) with an 80%-60% overlap between the image footprints (80% in width and 60% in height).

Both flights have been performed during nighttime to reduce the effect of solar radiation and to acquire thermal data at an hour close to the night pass of Landsat 8 satellite. Thermal flights were preceded by the acquisition of visible images during daylight hours. In Figure 23 the UAV acquired visible and thermal images are showed.

Thermal surveys were composed from set of shots for each flight. The internal software of the FLIR camera allows to correct each thermal shot for the

effects of distance, emissivity, atmospheric temperature and relative humidity. The effects of distances are corrected using the height of the set flight plan. The emissivity was set to value fixed of 0,96 considering the surface conditions and in accordance with the value of emissivity used in the Eq. 3 for satellite data (ASTER-GED emissivity around *Parco delle Biancane* area reaches value around 0.96-0.97 within the 10.6–11.2 μm range). Moreover, temperature and relative humidity were recorded with a thermo-hygrometer before the flight.

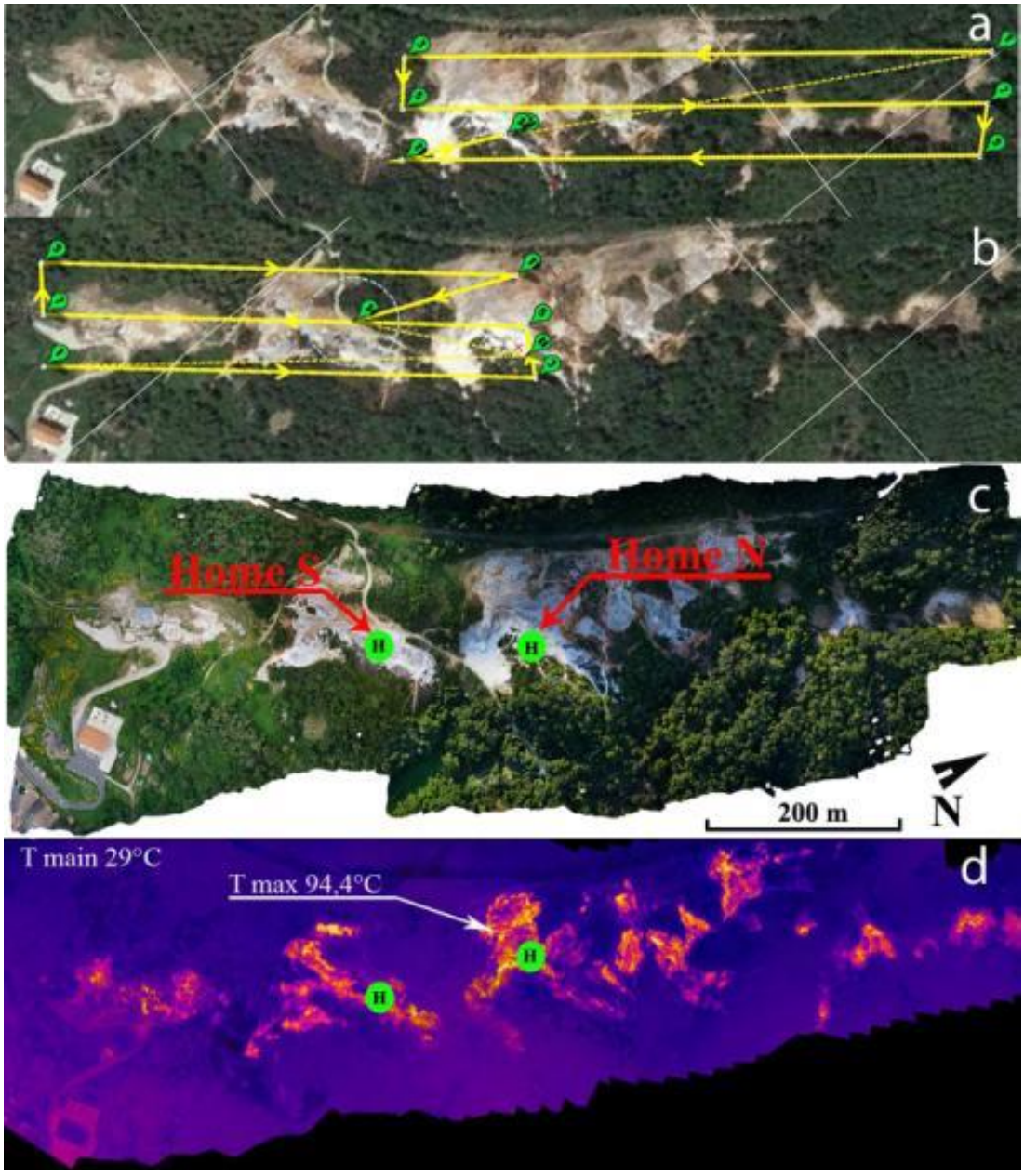

Figure 23. UAV flight of 19th June 2019 on the *Parco delle Biancane*: a) flight plan for the northern sector; b) flight plane for the southern sector c) visible mapping; d) thermal mapping. The "Home" (H) indicates the take-off point of the UAV which has a ground elevation of 621m and 610m in the northern and southern sector respectively.

The images collected by UAV were processed with bundle adjustment 3D-recostruction algorithm that allows to obtain an orthomosaic. All the reconstructions (both visible and thermal) were performed with the use of the Pix4D software (version 4.4.12) [76].

Date	Type of Flight Sector of Fligh	Flight Height (m)	Pixel Size at Ground (cm)	FH (m)	FV (m)	Ground Elev. (m ASL)	N° Image	Flight Duration (Min)
20/06/2018	V–N	110	2.2	129.3	85.8	611–658	105	15:58
20/06/2018	V–S	110	2.2	129.3	85.8	537–644	78	10:38
20/06/2018	T–N	120	22.7	145.1	116.1	606–660	47	07:28
20/06/2018	T–S	120	22.7	145.1	116.1	534–631	58	08:38
27/09/2018	T–N	150	28.3	181.3	145.1	602–695	59	09:10
27/09/2018	T–S	120	22.7	145.1	116.1	514–664	41	08:28
19/06/2019	T–N	120	22.7	145.1	116.1	597–691	164	22:01
19/06/2019	T–S	100	18.9	120.9	96.7	531–633	214	23:03

Table 9. Date of each measurement campaign; the type of flight if visible (V) or thermal (T) and relative sector of flight (N=North; S=South); the flight height and the relative parameters of the image that is pixel, Horizontal Field of View (FH), Vertical Field of View (FV), Range of Ground Elevation, number of pictures and flight duration.

In order to compare spatial thermal anomaly both of UAV and Landsat 8, polygons were defined around the anomaly based on the spatial resolution of the satellite data, with a regularly spaced 30mx30m grid. These polygons define the common thermal area of the analysis as shown in Figure 24. The temperature values inside the considered areas were extracted by using the zonal statistical function (ArcGIS© algorithm [73]). This algorithm allows to extract the main statistical information as the T average, Standard deviation, Range (T max - T min) and number of pixels per area (Table 10 and Table 11).

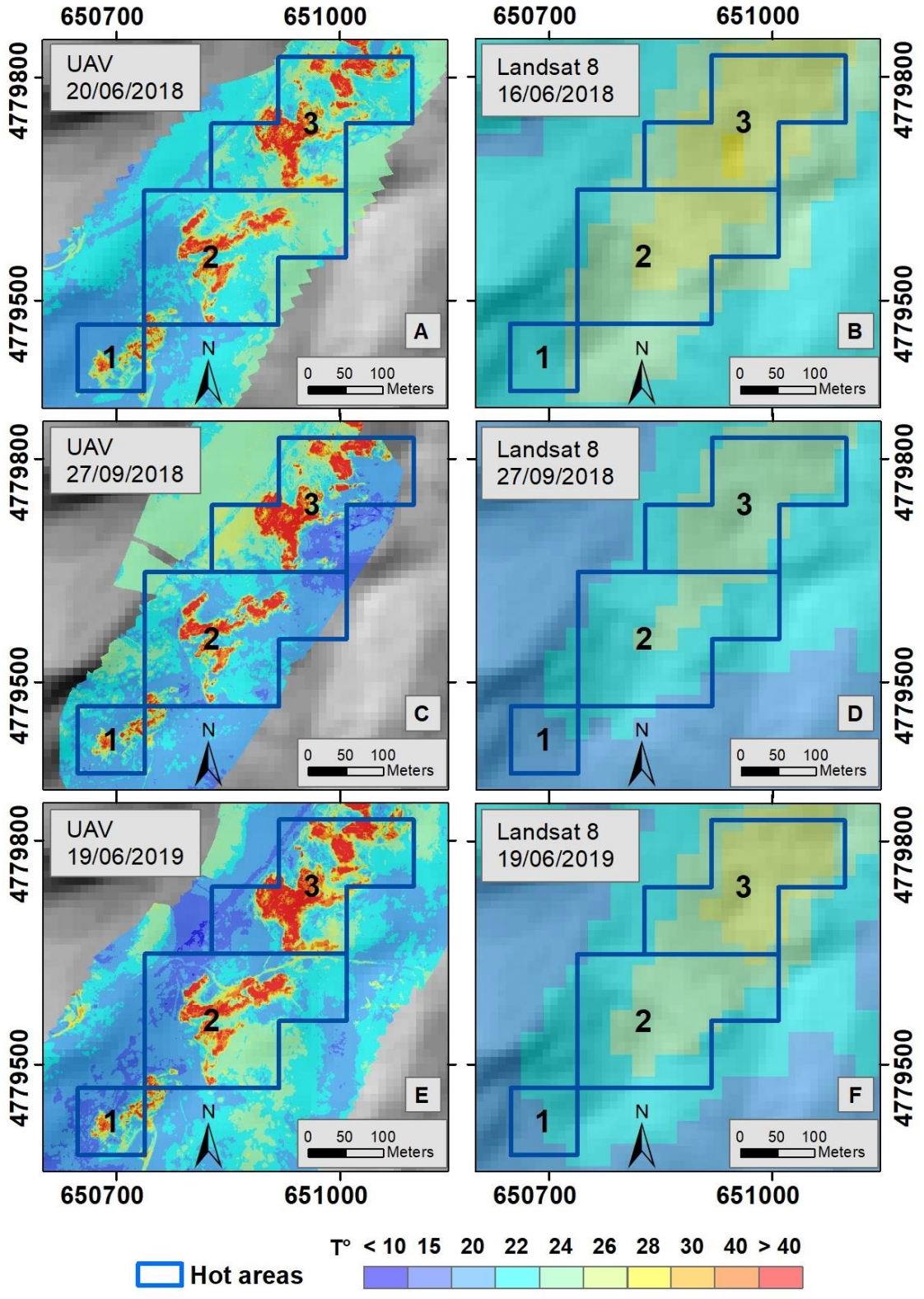

Figure 24. Maps of land surface temperature of UAV (A, C, E) and Landsat 8 (B, D, F).

Considering area 1 in Figure 24, for all three field campaigns, there is a high correlation between Landsat 8 and UAV average temperatures despite the fact that on June 2018 the UAV survey was not in sync with the satellite acquisition

data. Area 1 is the smallest (about 8100 m²) and the number of UAV pixels included in this area varies to the different flight heights (from 100 m to 120 m, as reported in Table 9). Moreover, the high spatial resolution of UAV thermal maps offers high accuracy in measurements, in agreement with the high number of pixels, the range and standard deviation reported in Table 10 and Table 11.

Area	T average °C	STD	Range	Pixels	Data and time
1	21.9	0.3	0.8	9	Landsat 8 16/06/2018 20:52 UTC
2	23.8	1.0	4.3	45	
3	25.1	0.9	3.2	36	
1	20.0	0.1	0.4	9	Landsat 8 27/09/2018 20:59 UTC
2	21.3	0.8	2.1	45	
3	22.6	0.6	2.4	36	
1	20.3	0.3	1.1	9	Landsat 8 19/06/2019 20:53 UTC
2	22.3	0.8	3.5	45	
3	24.3	1.1	4.3	36	

Table 10. Statistical analysis for Landsat 8.

Area	T average °C	STD	Range	Pixels	Data and time
1	21.3	5.5	56.8	99623	UAV 20/06/2018 22:25 UTC
2	23.7	6.8	67.8	495654	
3	26.4	9.6	64.0	398500	
1	21.4	5.9	63.4	107584	UAV 27/09/2018 22:30 UTC
2	22.2	8.4	89.4	520636	
3	26.1	12.7	79.0	402738	
1	19.8	6.4	58.1	152100	UAV 19/06/2019 20:52 UTC
2	22.6	8.6	71.4	762451	
3	26.7	13.0	77.7	608790	

Table 11. Statistical analysis for UAV.

The same considerations apply to area 2 (about 40500 m²): very good agreement with satellite data considering also the high number of UAV pixels covering the area.

With regard to area 3 (about 32400 m²), the UAV survey conducted on September 2018 unfortunately did not cover the same area (Figure 24c). This resulted in fewer UAV measurements included in this area (Table 11), missing the cold areas; this could explain the difference of satellite and UAV temperature (22.6°C, 26.1°C respectively).

For all three UAV surface temperature maps, the high variance of temperature range and the standard deviation reported in Table 10 and Table

11 demonstrate the strong capacity of the UAV measurements to obtain very detailed temperature maps.

4.6.2.2 Daytime acquisition: UAV – HyTES - ASTER and Landsat 8 data

A second cross-comparison test has been conducted using the comparison between LST estimated by ASTER and Landsat 8, surface temperature estimated by NASA HyTES and UAV survey. During the last field campaign (June 2019), data acquired by Twin-Otter Aircraft of HyTES project (NASA/JPL/ESA) have been collected thanks to a collaboration with NASA/JPL. Considering that HyTES flew on *Parco delle Biancane* during the morning of 18 June 2019 (approximatively at 9:15 UTC), even if no satellite passages were in synchronous with the flight, there are ASTER and Landsat 8 acquisition two and one day before. Since the methodology to retrieve LST is the same for daytime and nighttime data (even if it is better use nighttime data for analysis on thermal anomalies to eliminate temperature measurements inaccuracies due to the solar radiation) a cross-comparison can be considered with a further sensor.

Hyperspectral Thermal Emission Spectrometer (HyTES) is an airborne imaging spectrometer with 512 pixels across track with pixel sizes in the range of 5 to 50 m depending on aircraft flying height and 256 spectral channels between 7.5 and 12 μm [77]. It provides an opportunity to retrieve high spectral resolution emissivity and LST. Deriving LST and spectral emissivity from HyTES is an underdetermined problem since there are more unknowns (256 band emissivities, 1 temperature) than the total number of measurements available (256 radiances). To solve the underdetermined problem, HyTES uses an adapted version of the TES algorithm [49, 54].

HyTES flew in sync with several satellite overpasses (ASTER, Landsat 8). In particular, on 18 June 2019 HyTES flew in sync with UAV.

Data	Day and time acquisition	Pixel Spatial Resolution (m)
ASTER	16/06/2019, 10:22 UTC	90
Landsat 8	17/06/2019, 09:35 UTC	30*
HyTES	18/06/2019, 09:18 UTC	0.8
UAV	18/06/2019, 10:00 UTC	0.2

Table 12. Sensors, data and time of acquisition, pixel spatial resolution. *TIRS Landsat 8 has 100 m nominal pixel spatial resolution but the data are delivered at 30 m.

Figure 25 shows eight representative areas, selected at the ASTER and Landsat 8 pixel spatial resolution, used for the comparison. The areas have been selected considering the following features: a) pixels with the presence of thermal anomaly (the pixel is completely covered by the thermal anomaly, in figure the n.1); b) pixels with mixed features (presence of thermal anomaly and vegetation, pixel n. 4, 5, 6 and 8 in figure); c) pixels covered by vegetation (no presence of thermal anomaly, pixel n. 2, 3 and 7).

All HyTES and UAV temperature measurements contained in each representative area have been considered as single subset. For each of these subsets the HyTES and UAV averaged temperature have been calculated and compared with temperature estimated by both satellites (ASTER and Landsat 8).

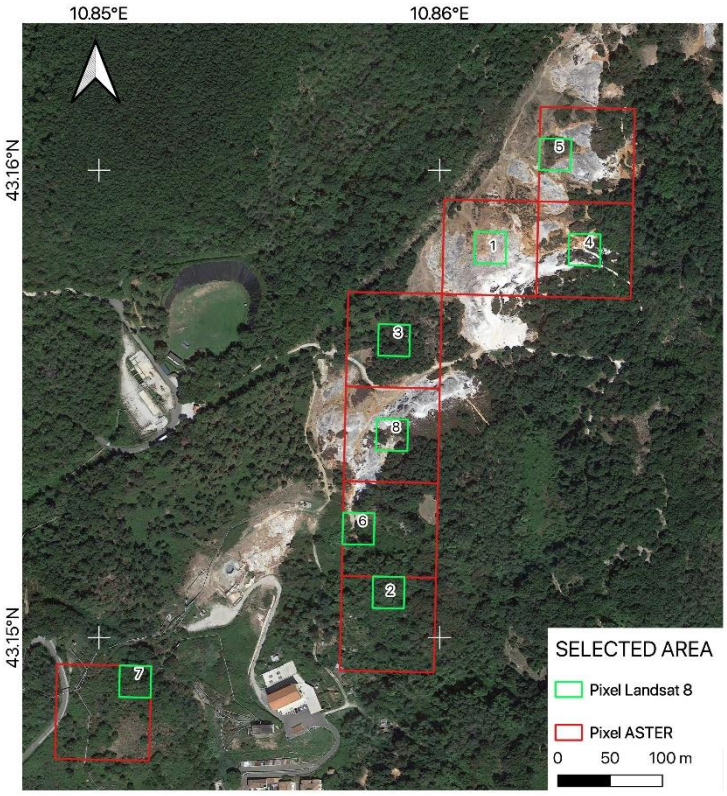

Figure 25. Representative areas at pixel spatial resolution: ASTER (red line), 90 m; Landsat 8 (green line), 30 m (even if 100 m is the nominal acquisition). The pixels are over plotted on ESRI Satellite Map.

Figure 26 and Figure 27 show the LST map obtained by using UAV (0.2 m pixel spatial resolution), HyTES (0.8 m pixel spatial resolution) and ASTER LST product (90 m pixel spatial resolution and acquired on June 16th 2019).

Table 13 reports the comparisons of LST using the three different sensors. Large difference is evident, especially in the areas where thermal anomaly covers whole pixel or in mixed pixels, while in representative pixels, where no thermal anomaly is present (vegetation), the three LTS estimated have good agreement.

# Area	Description	ASTER June 16th 2019	HyTES June 18th 2019		UAV June 18th 2019	
		T	T	St. Dev.	T	St. Dev.
1	Thermal anomaly	37.7	45.6	10.4	51.8	13.5
2	Vegetation	25.6	26.4	1.0	24.9	2.3
3	Vegetation	34.8	31.1	4.8	32.3	7.5
4	Mixed	30.2	34.2	9.4	39.1	8.8
5	Mixed	34.1	41.4	11.6	45.4	13.8
6	Mixed	26.3	29.0	5.7	30.2	6.9
7	Vegetation	28.7	32.6	5.3	20.1	4.1
8	Mixed	31.2	40.7	9.4	39.3	10.2

Table 13. Temperature comparison: ASTER LST vs HyTES and UAV LST. All values are in °C.

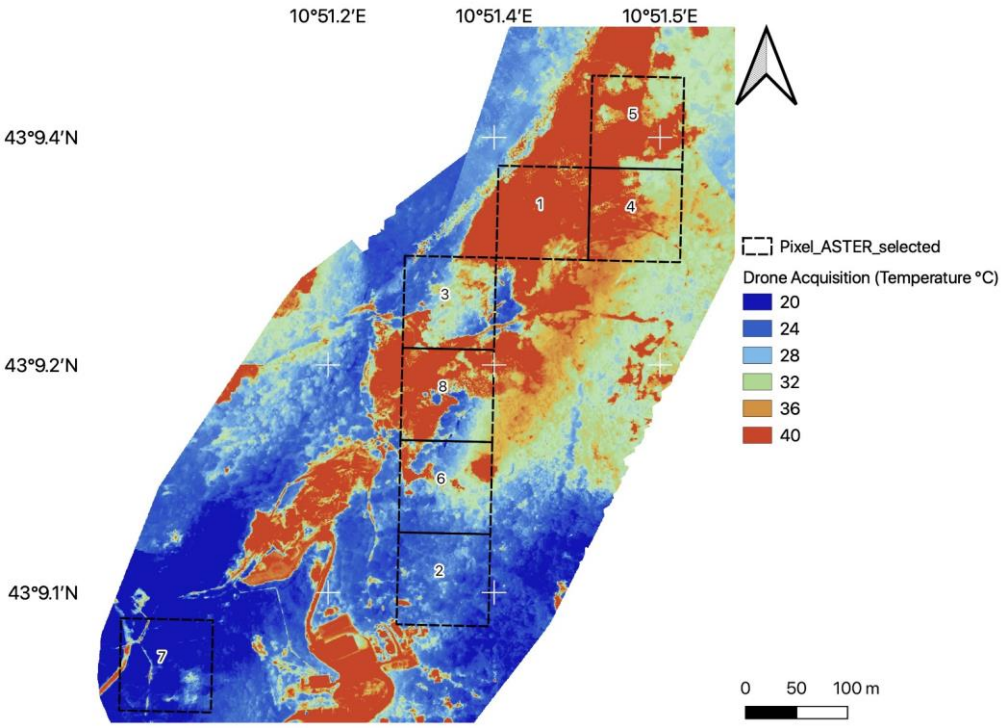

Figure 26. LST products of the UAV(drone)-TIR camera flight acquired on June 18th 2019. The area of pixels used for comparison of ASTER and UAV surface temperature has 90 m resolution (pixel included in dashed squares). The ASTER data was acquired on June 16th 2019.

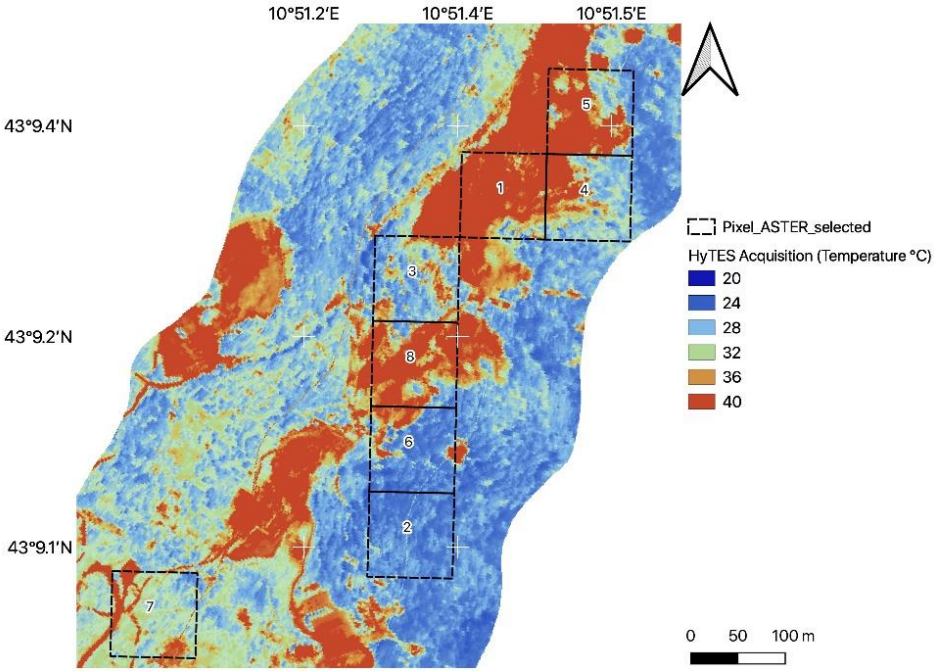

Figure 27. LST products of the HyTES flight acquired on June 18th 2019. The area of pixels used for comparison of ASTER and HyTES surface temperature has 90 m resolution (pixel included in dashed squares). The ASTER data was acquired on June 16th 2019.

Moreover, in order to better understand the correlation between the temperature estimates, the r is used.

r: ASTER LST vs HyTES LST = 0.79 (P-value = 0.019659)

r: ASTER LST vs UAV LST = 0.77 (P-value = 0.025412)

Analysing the Figure 26, Figure 27 and the associated Table 13, some considerations can be done:

1) ASTER data was acquired two days before the HyTES and UAV flights. The difference in day acquisition can influence the estimation of temperature by ASTER especially considering different weather conditions in two days (i.e. humidity or rain influence the surface temperature).
2) ASTER pixel spatial resolution (90 m) does not offer the possibility to discriminate the temperature differences as HyTES and UAV (0.8 m and 0.2 m pixel spatial resolution respectively) and for this reason there is an underestimation of temperature.

3) Area 1 (Figure 26, Figure 27 and Table 13) has been selected as pixel with high presence of thermal anomalies. Because the number of measurements collected by HyTES and UAV corresponding to the Area 1 is very high (about 12000 and 110000 respectively), the contribute of these measurements moves the mean temperature toward higher value. Despite this, the ASTER pixel 1 has higher value of temperature than the mixed and vegetation ASTER pixels selected for the analysis. This confirms the capability of ASTER to detect thermal anomalies.
4) Mixed areas show large temperature differences between ASTER and HyTES/UAV measurements, probably as a result of the presence of thermal anomalies and the coarse spatial resolution of ASTER.
5) Areas with no presence of thermal anomaly (2, 3 in Figure 26, Figure 27 and Table 13) show a very good agreement taking in account the difference of spatial resolution; exception is for area 7 where the UAV measurements are probably affected by errors.
6) r have a value greater than 0.7 that means a strong positive linear relationship (p-values are less than 0.05 that means statistically significant).

Same considerations can be done to Figure 28 and Figure 29, that show the comparison between LST estimated by Landsat 8 (acquired on June 17th 2019) and both HyTES and UAV sensors.

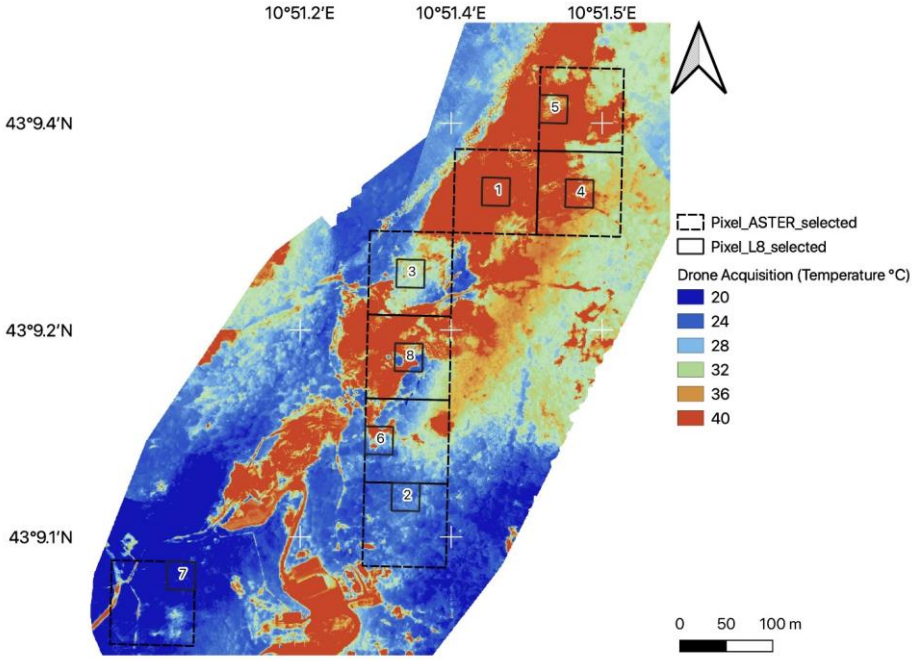

Figure 28. LST products of the UAV(drone)-TIR camera flight acquired on June 18th 2019. The area of pixels used for comparison of Landsat 8 and UAV surface temperature has 30 m resolution (pixel included squares). The Landsat 8 data was acquired on June 17th 2019.

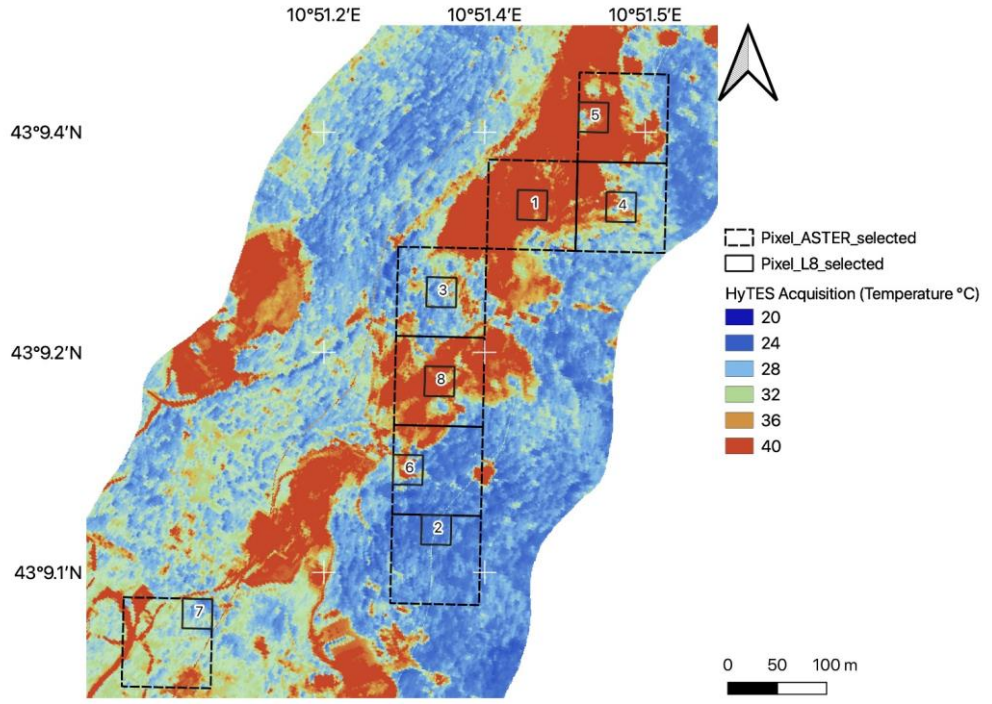

Figure 29. LST products of the HyTES flight acquired on June 18th 2019. The area of pixels used for comparison of Landsat 8 and HyTES surface temperature has 30 m resolution (pixel included in squares). The Landsat 8 data was acquired on June 17th 2019.

# Area	Description	Landsat June 17th 2019	HyTES June 18th 2019		UAV June 18th 2019	
		T	T	St. Dev.	T	St. Dev.
1	Thermal anomaly	38.2	49.0	7.8	58.2	11.6
2	Vegetation	30.0	26.0	0.8	25.5	1.0
3	Vegetation	33.5	29.3	3.2	30.7	1.7
4	Mixed	34.6	34.1	5.7	41.7	4.8
5	Mixed	36.0	45.6	12.2	45.2	13.2
6	Mixed	32.9	31.8	5.8	31.8	8.6
7	Vegetation	31.3	28.7	1.7	18.5	1.2
8	Mixed	33.6	44.4	7.3	35.5	9.4

Table 14. Landsat 8 LST vs HyTES and UAV LST. All values are in °C.

r: Landsat 8 LST vs HyTES LST = 0.86 (p-value = 0.00616)

r: Landsat 8 LST vs UAV LST = 0.95 (p-value= 0.000301)

Also in this case, same considerations can be done:

1) Landsat 8 data was acquired one day before the HyTES and UAV flights. As for ASTER, the difference in day acquisition can influence the estimation of temperature by Landsat 8 especially considering different weather conditions in one days (i.e. humidity or rain influence the surface temperature).
2) Landsat 8 pixel spatial resolution (30 m considering the delivered data, even if the nominal spatial acquisition of TIRS is 100 m) does not offer the possibility to discriminate the temperature as HyTES and UAV (0.8 m and 0.2 m pixel spatial resolution respectively) and for this reason there is a underestimation of temperature.
3) Area 1 (Figure 28, Figure 29 and Table 14) has been selected as pixel with high presence of thermal anomalies. Because the number of measurements collected by HyTES and UAV corresponding to the Area 1 is very high (about 1400 and 12000 respectively), the contribute of these measurements moves the mean temperature toward higher value. Despite this, the Landsat 8 pixel 1 has higher value of temperature than the mixed and vegetation Landsat 8 pixels selected for the analysis.
4) Mixed areas (4, 6 and 8) have comparable values between Landsat 8 and HyTES/UAV measurements, while the only one not comparable is area 5.
5) Areas with no presence of thermal anomaly (2, 3) show a very good comparison taking in account the difference of spatial resolution; exception is for area 7 where the UAV measurements are probably affected by errors.
6) r have a value greater than 0.8 that means a strong positive linear relationship (p-values are less than 0.05 that means statistically significant).

To conclude, even if the measurements have been collected during the day (at 10:00 UTC) and this can introduce the effect of "noise" due to the solar irradiation, there are very comparable results, especially considering also that satellite data have a pixel spatial resolution coarser than HyTES and UAV.

4.6.2.3 *ASTER vs Landsat 8*

Last consideration on LST cross-validation can be done comparing ASTER and Landsat 8 LST estimated with different methodology (TES for ASTER, SCA for Landsat 8).

ASTER pixel spatial resolution is 90 m respect to Landsat 8 (delivered at 30 m, even if the TIRS instrument acquires at 100 m). In Figure 30 two surface

temperature maps estimated with ASTER and Landsat 8 are showed. In particular, temperature over 34.5° C estimated both by ASTER and Landsat 8 are considered The detection of the same areas with high temperature (both in presence of thermal anomalies and in presence of city) is the same for two sensors, even if the methodology used for LST estimation is different (TES for ASTER, SCA for Landsat 8). Also in this case r between Landsat 8 LST vs ASTER LST (0.88) shows the good agreement.

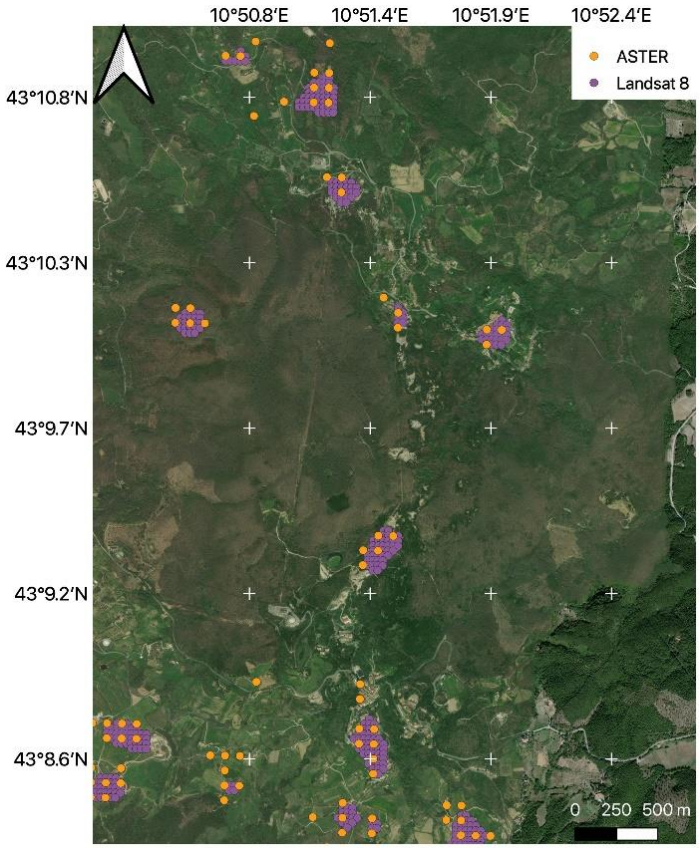

Figure 30. LST products obtained by processing ASTER (16 June 2019, in orange) and Landsat 8 (17 June 2019, in violet) both acquired at 10:00 UTC approximately. Orange points represent ASTER pixels (90 m) and violet points represent Landsat 8 pixels (30 m) where thermal anomalies are detected.

4.6.3 Validation of LST on *Modena* city

The 43 LST maps have been averaged to obtain the mean LST map (Figure 31).

The mean LST range from 10.3 °C to 22.9 °C, with an average of 15.8 °C. The three quartiles (25%, 50%, 75%) are 14.8 °C, 15.4 °C (close to the average) and 16.3 °C respectively (see also Table 15). Since the studied area comprises rural

and urban environments the median value 15.4 °C has been assumed as the reference that separates warm and cold surfaces.

Class	Pixel	Area	Min	Max	Mean	St.Dev.	Q1	Q2	Q3
A	39810	35.5 km²	13.8	20.0	17.7	0.9	17.0	17.8	18.4
B	205086	184.6 km²	10.3	18.9	15.2	0.7	14.7	15.1	15.6
C	3582	3.2 km²	16.9	22.9	19.7	1.6	18.2	19.9	21.1
All	248478	223.3 km²	10.3	22.9	15.8	1.4	14.8	15.4	16.3

Table 15. Temperature statistics of classes (temperature in °C)

The isoline corresponding to this reference have been added to in Figure 31 and marked as "0" (solid line). Similarly, the isoline corresponding to +2 °C of difference (higher than the reference) has been added and marked as "2" (dashed line). The main observations emerging from this analysis is that built areas (e.g. b1-b4 points of interest) and water surfaces (e.g. w1-w5 points of interest) are totally included inside the "0" isoline, i.e. they are warmer than rural areas.

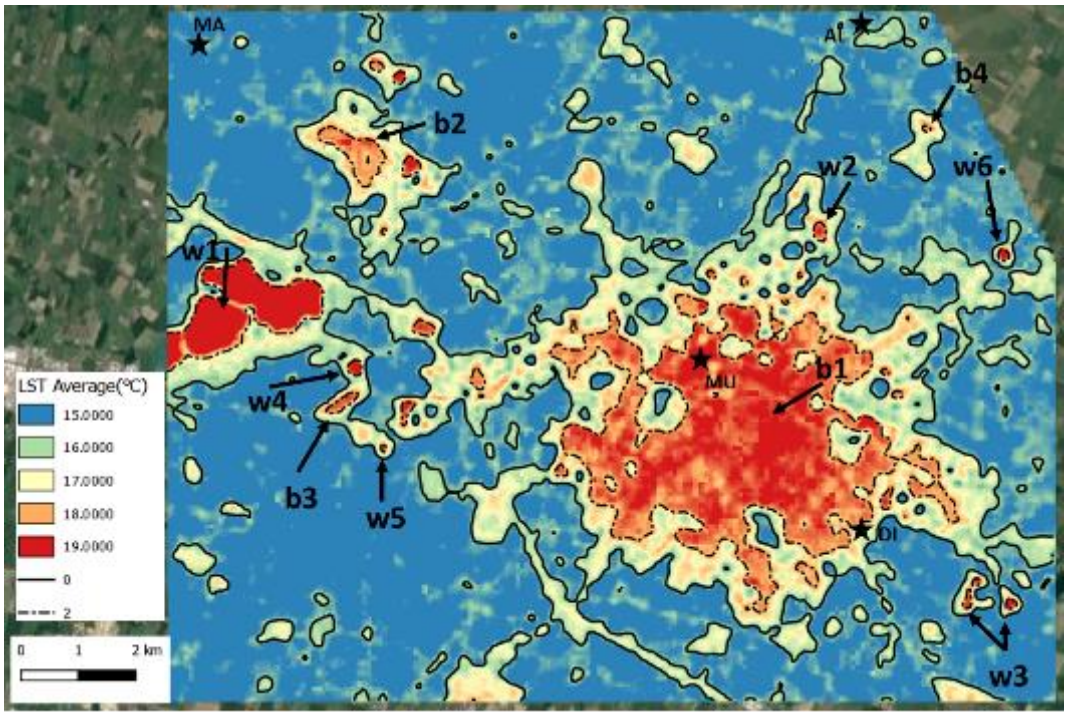

Figure 31. Average LST, "0" and "2" isolines (see text)**.** Stars indicate weather stations: AL-*Albareto*, MU-*Modena Urbana*, DI-DIEF campus, MA-*Marzaglia*. Some particulars cited 5.4. Waters: w1, *Secchia* river natural reserve (lakes); w2-*Modena* sewage treatment tanks; *Panaro* river natural reserve (lakes); w4 and w5, artificial pounds. Built: b1, *Modena* historic center; b2; *Campogalliano* town; b3, freight yard/storage area; b4; *Albareto* town.

To asses if LST temperature describes near ground air temperature (2m), four meteorological stations have been used (Figure 32 and Figure 33): *Albareto* (AL), *Marzaglia* (MA), *Modena Urbana* (MU) and Campus DIEF (DI). For each station, air temperatures measured at satellite overpass times has been compared to LST extracted from the pixel corresponding to the location of the stations.

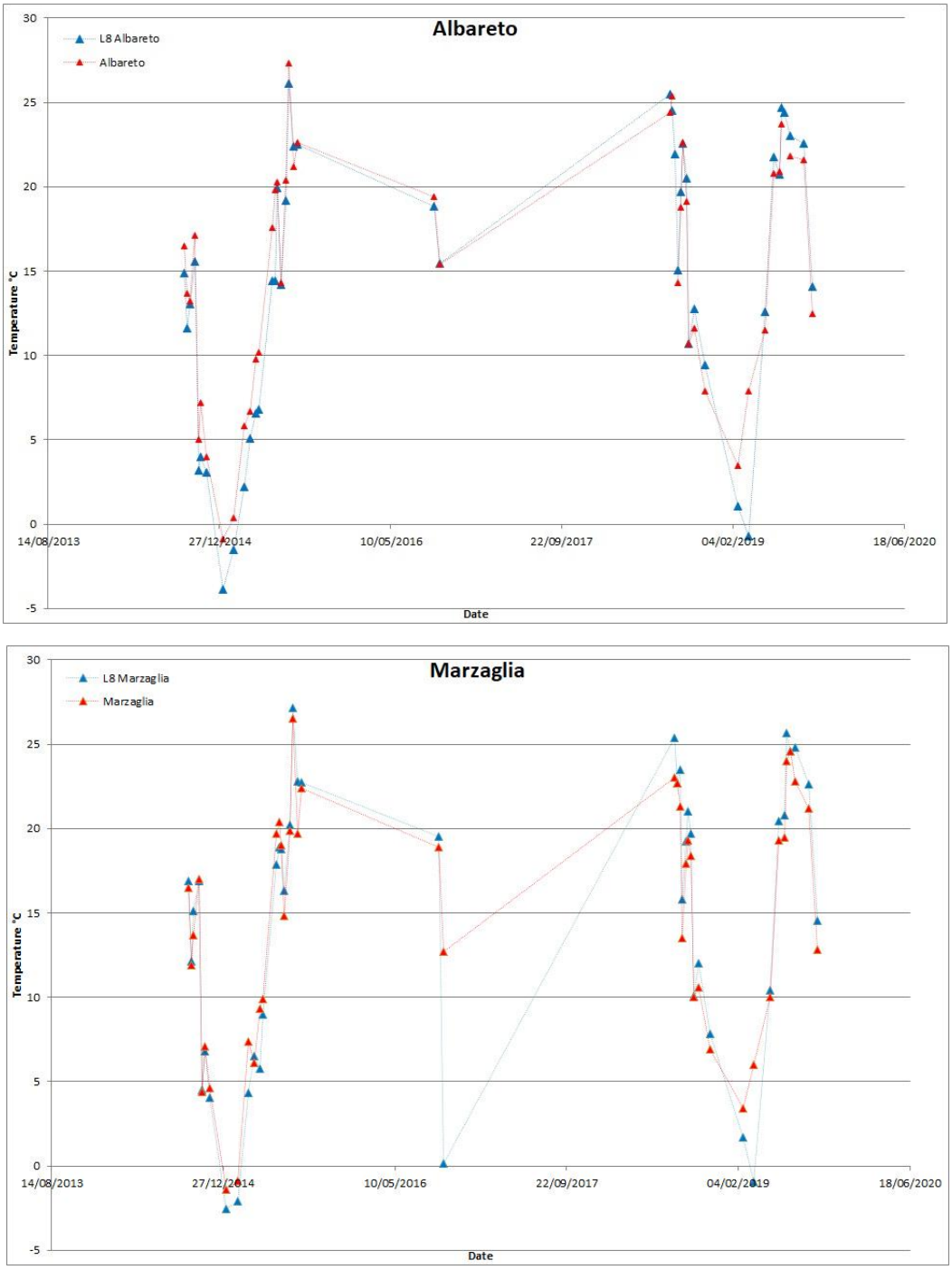

Figure 32. Time series of LST derived by Landsat 8 and of air temperature measured by the weather stations of *Albareto* and *Marzaglia*.

Figure 32 and Figure 33 show the time series of LST computed by remote sensing data and the air temperature (2m) measured by the four meteorological stations are compared. The LST used in the comparisons are those of the pixel nearest to the location of the ground measurements.

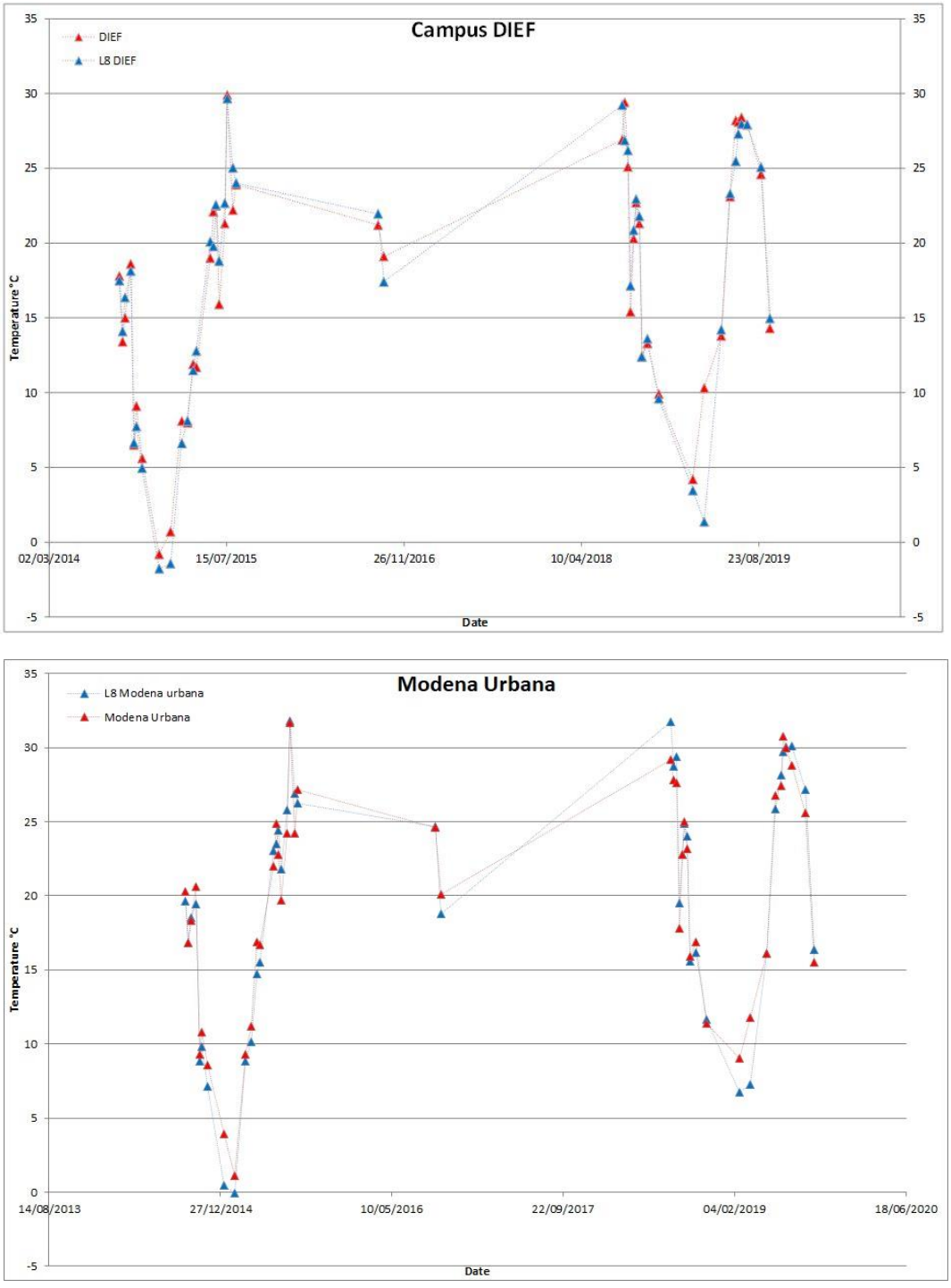

Figure 33. Time series of LST derived by Landsat 8 and of air temperature measured by the weather stations of Campus DIEF and *Modena* urban.

In Figure 34 the scatter plots of this comparison are also shown. This figure indicates the good agreement between the two kind of measurements.

Figure 32, Figure 33 and Figure 34 evidence the good agreement between LST and ground air temperature. This agreement is also supported by the statistics reported in Table 16. Mean values are lower than 0.5 °C in all cases. Air temperature seems to be slightly higher than LST but the differences are too low to make any inference, while standard deviation shows that LST is more variable than air temperature.

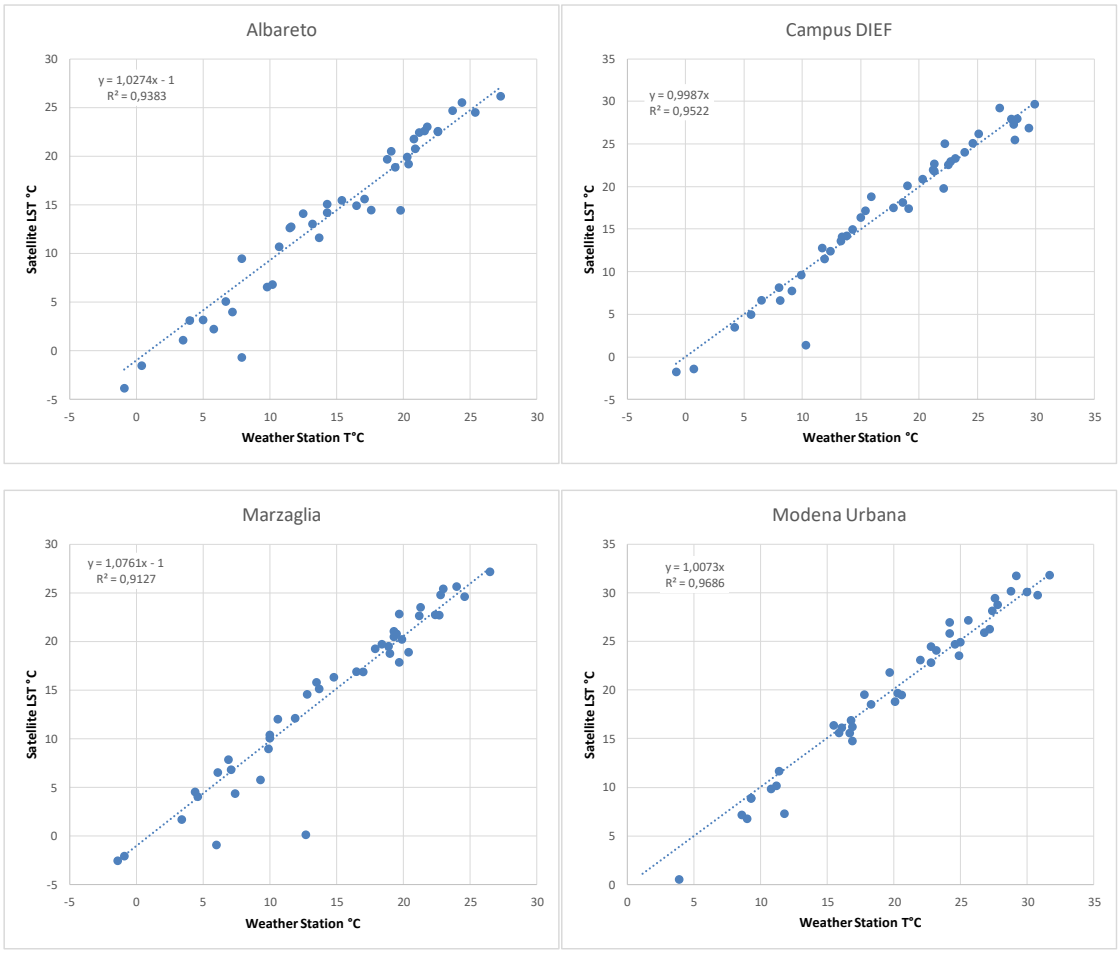

Figure 34. Scatter plots of LST Time series derived by Landsat 8 and air temperature measured by the weather stations. Linear trend line and R2 are included.

This is a confirmation that LST well describes near ground air temperature and then can be used to analyze air temperature time series where direct measurements are not available.

Measurements	Mean (°C)	St.Dev. (°C)	Correlation
MU	19.6	7.6	0.99
LST at MU	19.5	8.5	
AL	14.8	7.3	0.97
LST at AL	14.3	8.4	
MA	14.6	7.2	0.96
LST at MA	14.5	8.5	
DI	17.3	8.1	0.98
LST at DI	17.1	8.6	
All stations	16.4	8.1	0.98
LST at all s.	16.2	9.0	

Table 16. LST and air temperature comparison at different weather stations.

4.7 References of chapter 4

42. Prata, A. J., Caselles, V., Coll, C., Sobrino, J. A., & Ottle, C. (1995). Thermal remote sensing of land surface temperature from satellites: Current status and future prospects. Remote Sensing Reviews, 12(3-4), 175-224.
43. Valor, E., Caselles, V. (1996). Mapping land surface emissivity from NDVI: Application to European, African, and South American areas. Remote sensing of Environment, 57(3), 167-184.
44. von Clarmann, T., & Echle, G. (1998). Selection of optimized microwindows for atmospheric spectroscopy. Applied optics, 37(33), 7661-7669.
45. Holst, G. C. (2000). Common sense approach to thermal imaging (pp. 90-109). Washington: SPIE Optical Engineering Press.
46. Li, Z.-L., Tang, B.-H., Wu, H., Ren, H., Yan, G., Wan, Z., Trigo, I. F., & Sobrino, J. A. (2013). Satellite-derived land surface temperature: Current status and perspectives. Remote Sensing of Environment, 131, 14-37.
47. Li, Z.-L., Wu, H., Wang, N., Qiu, S., Sobrino, J. A., Wan, Z., Tang, B.-H., & Yan, G. (2013). Land surface emissivity retrieval from satellite data. International Journal of Remote Sensing, 34(9-10), 3084-3127.
48. Sobrino, J. A., & Jiménez-Muñoz, J. C. (2014). Minimum configuration of thermal infrared bands for land Surface temperature and emissivity in the context of potential future missions. Remote Sensing of Environment, 148, 158-167.
49. Gillespie, A., Rokugawa, S., Matsunaga, T., Cothern, J. S., Hook, S., & Kahle, A. B. (1998). A temperature and emissivity separation algorithm for advanced spaceborne thermal emission and reflection radiometer (ASTER) images. IEEE Transactions on Geoscience and Remote Sensing, 36(4), 1113-1126.
50. USGS. Landsat 8 OLI and TIRS Calibration Notices. Available online: https://www.usgs.gov/land-resources/nli/landsat/landsat-8-oli-and-tirs-calibration-notices (accessed on 29 April 2021).

51. Musacchio, M., Amici, S., Silvestri, M., Teggi, S., Buongiorno, M. F., Silenzi, S., & Devoti, S. (2007, November). Application of CIRILLO: a new atmospheric correction tool on Castel Porziano Beach (CPB). In Remote Sensing for Environmental Monitoring, GIS Applications, and Geology VII (Vol. 6749, p. 674935). International Society for Optics and Photonics.
52. Berk, A., Conforti, P., Kennett, R., Perkins, T., Hawes, F., & Van Den Bosch, J. (2014, June). MODTRAN® 6: A major upgrade of the MODTRAN® radiative transfer code. In 2014 6th Workshop on Hyperspectral Image and Signal Processing: Evolution in Remote Sensing (WHISPERS) (pp. 1-4). IEEE.
53. Berk, A., Conforti, P., & Hawes, F. (2015, May). An accelerated line-by-line option for MODTRAN combining on-the-fly generation of line center absorption within 0.1 cm-1 bins and pre-computed line tails. In Algorithms and Technologies for Multispectral, Hyperspectral, and Ultraspectral Imagery XXI (Vol. 9472, p. 947217). International Society for Optics and Photonics.
54. Gillespie, A. R., Rokugawa, S., Hook, S. J., Matsunaga, T., & Kahle, A. B. (1999). Temperature/emissivity separation algorithm theoretical basis document, version 2.4. ATBD contract NAS5-31372, NASA.
55. Gillespie, A. R. (1986). Lithologic mapping of silicate rocks using TIMS. JPL Publication 86-38, pp. 29-44.
56. Gillespie, A. R., Abbott, E. A., Gilson, L., Hulley, G., Jiménez-Muñoz, J.-C., & Sobrino, J. A. (2011). Residual errors in ASTER temperature and emissivity standard products AST08 and AST05. Remote Sensing of Environment, 115, 3681-3694.
57. Sabol Jr, D. E., Gillespie, A. R., Abbott, E., & Yamada, G. (2009). Field validation of the ASTER temperature–emissivity separation algorithm. Remote Sensing of Environment, 113(11), 2328-2344.
58. Li, Z. L., Tang, B. H., Wu, H., Ren, H., Yan, G., Wan, Z., ... & Sobrino, J. A. (2013). Satellite-derived land surface temperature: Current status and perspectives. Remote sensing of environment, 131, 14-37.
59. Yu, X., Guo, X., & Wu, Z. (2014). Land surface temperature retrieval from Landsat 8 TIRS—Comparison between radiative transfer equation-based method, split window algorithm and single channel method. Remote sensing, 6(10), 9829-9852.
60. Li, S., & Jiang, G. M. (2018). Land surface temperature retrieval from Landsat-8 data with the generalized split-window algorithm. IEEE Access, 6, 18149-18162.
61. Vlassova, L., Perez-Cabello, F., Nieto, H., Martín, P., Riaño, D., & De La Riva, J. (2014). Assessment of methods for land surface temperature retrieval from Landsat-5 TM images applicable to multiscale tree-grass ecosystem modeling. Remote Sensing, 6(5), 4345-4368.

62. Renard, F., Alonso, L., Fitts, Y., Hadjiosif, A., & Comby, J. (2019). Evaluation of the effect of urban redevelopment on surface urban heat islands. Remote Sensing, 11(3), 299.
63. Walawender, J. P., Szymanowski, M., Hajto, M. J., & Bokwa, A. (2014). Land surface temperature patterns in the urban agglomeration of Krakow (Poland) derived from Landsat-7/ETM+ data. Pure and Applied Geophysics, 171(6), 913-940.
64. USGS data provider, available on line: https://earthexplorer.usgs.gov/ (accessed 29 April 2021).
65. ASTER Global Emissivity Dataset GED, available on line: https://lpdaac.usgs.gov/products/ag100v003/ (accessed 29 April 2021).
66. Hulley, G. C., Hook, S. J., Abbott, E., Malakar, N., Islam, T., & Abrams, M. (2015). The ASTER Global Emissivity Dataset (ASTER GED): Mapping Earth's emissivity at 100 meter spatial scale. Geophysical Research Letters, 42(19), 7966-7976.
67. Guo, G., Wu, Z., Xiao, R., Chen, Y., Liu, X., & Zhang, X. (2015). Impacts of urban biophysical composition on land surface temperature in urban heat island clusters. Landscape and Urban Planning, 135, 1-10.
68. Weng, Q., Lu, D., & Schubring, J. (2004). Estimation of land surface temperature–vegetation abundance relationship for urban heat island studies. Remote sensing of Environment, 89(4), 467-483.
69. Zakšek, K., & Oštir, K. (2012). Downscaling land surface temperature for urban heat island diurnal cycle analysis. Remote Sensing of Environment, 117, 114-124.
70. Sansivero, F., & Vilardo, G. (2019). Processing Thermal Infrared Imagery Time-Series from Volcano Permanent Ground-Based Monitoring Network. Latest Methodological Improvements to Characterize Surface Temperatures Behavior of Thermal Anomaly Areas. Remote Sensing, 11(5), 553.
71. Caputo, T., Bellucci Sessa, E., Silvestri, M., Buongiorno, M. F., Musacchio, M., Sansivero, F., & Vilardo, G. (2019). Surface temperature multiscale monitoring by thermal infrared satellite and ground images at *Campi Flegrei* volcanic area (Italy). Remote Sensing, 11(9), 1007.
72. FLIR A655sc High-Resolution Science Grade LWIR Camera | FLIR Systems. Available online: https://www.flir.com/products/a655sc/ (accessed on 29 April 2021).
73. Environmental Systems Research Institute. (2011). ArcGIS desktop: release 10.
74. García-Santos, V., Cuxart, J., Jiménez, M. A., Martínez-Villagrasa, D., Simó, G., Picos, R., & Caselles, V. (2018). Study of Temperature Heterogeneities at Sub-Kilometric Scales and Influence on Surface–Atmosphere Energy Interactions. IEEE Transactions on Geoscience and Remote Sensing, 57(2), 640-654.

75. Marotta E., Avvisati G., Belviso P., Carandente A., Peluso R., Sansivero F., Vilardo G., Sangianantoni A., Santiccioli G., Sacchetta E. & Pessah P. (2017) Gestione operativa dei SAPR OV-INGV per monitoraggio e ricerca, INGV Rapporti Tecnici 2017, n. 365, ISSN 2039-7941.
76. Pix4DMapper User Manual, available on line: https://support.pix4d.com/hc/en-us/sections/360003718992-Manual (accessed on 24 April 2021).
77. Hook, S. J., Johnson, W. R., & Abrams, M. J. (2013). NASA's hyperspectral thermal emission spectrometer (HyTES). In Thermal Infrared Remote Sensing (pp. 93-115). Springer, Dordrecht.

5 THERMAL ANOMALY DETECTION

The identification of thermal anomalies from LST maps is very interesting for many environmental applications. For example, its detection and monitoring can be useful for observation on volcanoes behavior [78,79] or for detecting geothermal activity for geothermal exploration [5, 80-82]. However, LST time series are often difficult to interpret due to the presence of seasonality, other trends and residuals. Considering that the removing seasonality is a bit complicated specially if the time series is not continuous and since in this study the detection of the thermal anomaly is the main task, the use of Principal Component Analysis (PCA) will be considered.

5.1 PCA utility

PCA is a technique for reducing the dimensionality of datasets, transforming a number of correlated variables into a number of uncorrelated variables called principal components (PC) [83-88]. PCA increases interpretability of the data but at the same time minimizing information loss. In particular, in this study, the use of PCA does not require the removal of seasonality in the LST time series. The first PC band contains the largest percentage of data variance and the second PC band contains the second largest data variance, and so on. The last PC bands appear noisy because they contain very little variance, much of which is due to noise in the original data. A high and positive value of a pixel in the first PC represents that the values of this pixel have been large and unchanged over time, while a low and more negative value of a pixel in the first PC indicates that the values of that pixel have been low and unchanged over time. If the value of first PC is close to zero it indicates that changes in the values of the pixel have been high over time. Usually, the first PC accounts for the maximum proportion of data variance, but also PC2 and PC3 account for the majority of the variance found within the dataset. Moreover, since one PC is insufficient to model the systematic variation of LST dataset, the second PC is also considered. Following the approach of Muller et al, (2014) [89], PCA has been applied to LST time series of TIR remote sensing data of the three test sites (*Campi Flegrei, Parco delle Biancane* and *Modena* City).

In this contest, the most dominant patterns, in terms of thermal anomaly, can be extracted from LST time series using PCA. The mathematical concepts on PCA are better reported in the main scientific works and they are not included in this work.

5.2 Application on *Solfatara-Campi Flegrei* area

The Figure 35 shows the studied area and the main features that will be analysed in the next.

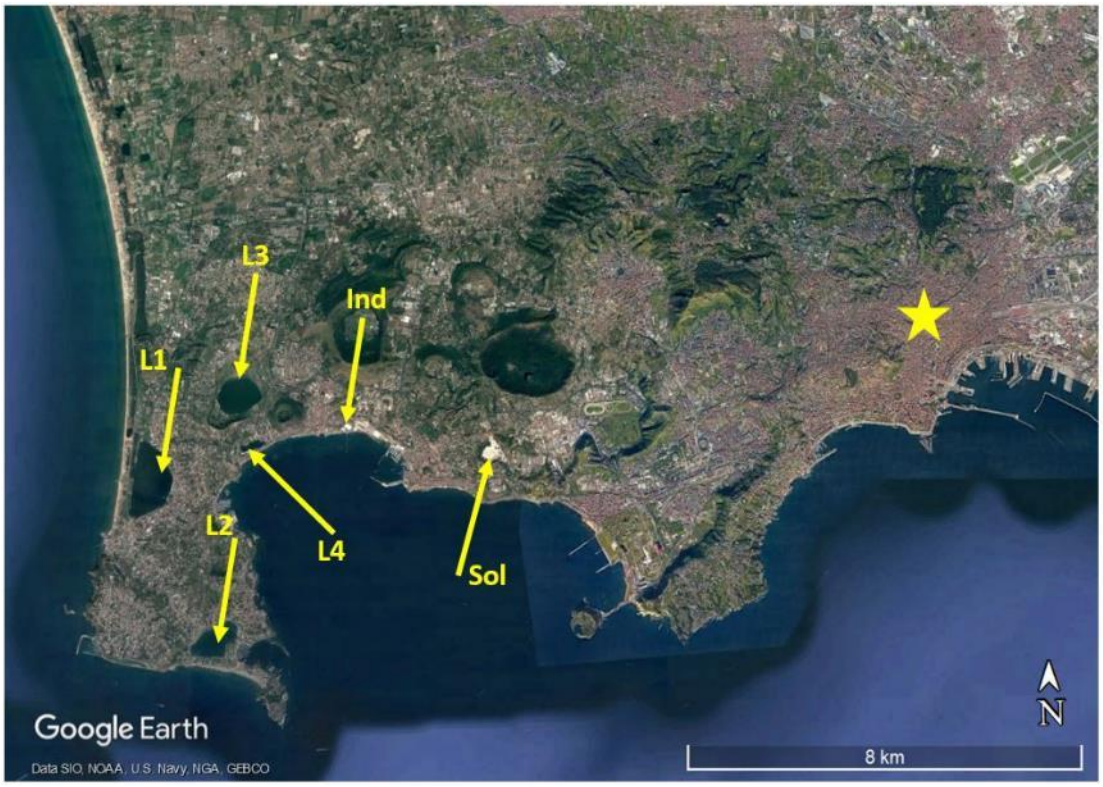

Figure 35. Studied area. Lakes: L1-*Fusaro*; L2-*Miseno*; L3-*Averno*; L4-*Lucrino*; Sol-*Solfatara* volcano; Ind-industrial area; star *Napoli* City Center.

Two maps have been obtained by averaging the 55 LST maps for Landsat 8 and 40 LST maps for ASTER data respectively (Figure 36).

Both mean LSTs range from 15 °C to 25 °C, with an average of 17 °C and a maximum of about 25 °C inside the *Solfatara* volcano area. Since the studied area comprises sea and land surface, the mean sea temperature (that is about 23°C) is not included in this analysis. For this reason, the surface where thermal anomalies are present corresponds to the land.

To refine this analysis, the PCA of the Landsat 8 and ASTER LST image has been applied using the Forward PC Rotation on ENVI software [90], calculating statistics information using covariance matrix, and the two separated Landsat 8 and ASTER LST time series (already described in the previous chapter) have been considered. The PCA of the LST pattern time series allows the identification of dominant independent patterns within the time series, ranked by the ability to explain the temporal variation in the LST time series.

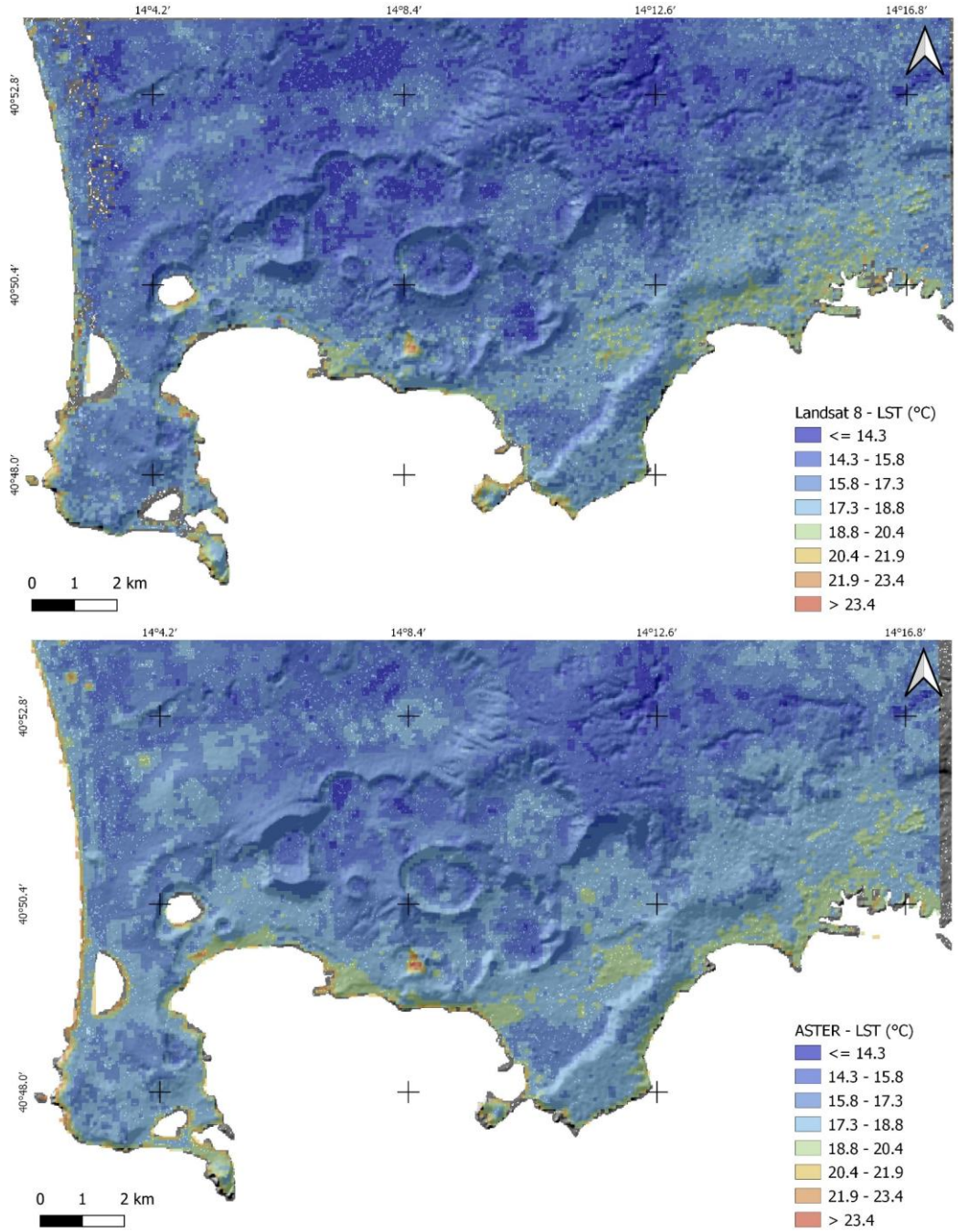

Figure 36. Mean LST obtained by processing Landsat 8 (up) and ASTER (down) LST data.

For both ASTER and Landsat 8 LST time series, the eigenvalues and eigenvectors of the covariance matrix are found. The covariance matrix is computed by ENVI in order to obtain the eigenvalues, which are in the same number of the input variables. Statistics required by PCA were computed excluding water surface (sea) using a sea/land mask defined as a binary image that consists of values of 0 (sea) and 1 (land).

Concerning Landsat 8 data, the eigenvalues of the transformation show that the majority, 73%, of the information across time is described by PC1, PC2 and PC3 contributions are 15 and 3% (Figure 37), the other PCs have a very low weight.

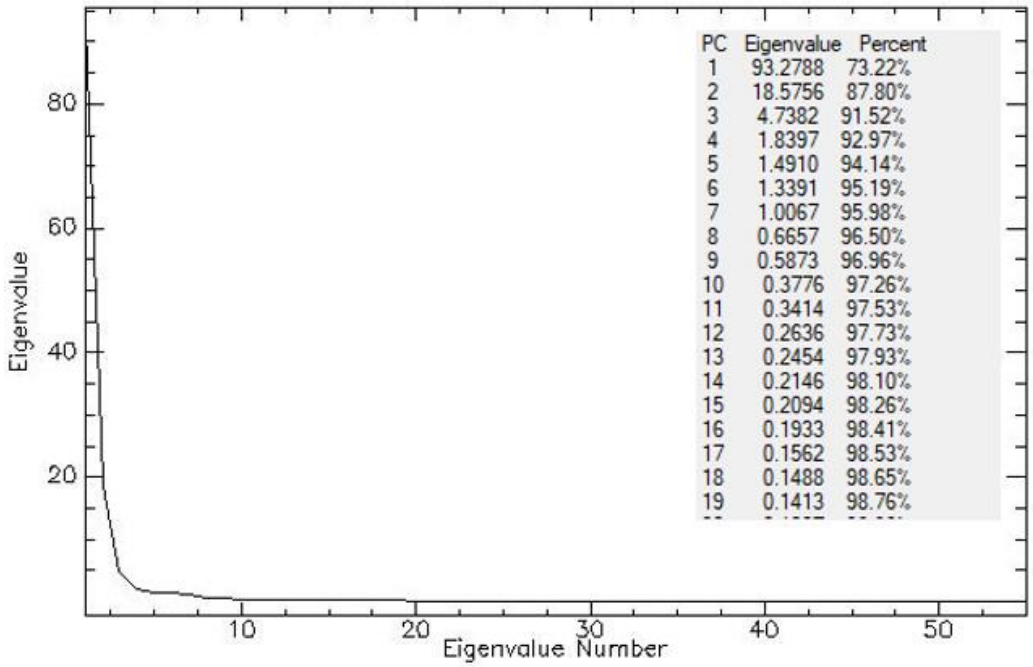

PC	Eigenvalue	Percent
1	93.2788	73.22%
2	18.5756	87.80%
3	4.7382	91.52%
4	1.8397	92.97%
5	1.4910	94.14%
6	1.3391	95.19%
7	1.0067	95.98%
8	0.6657	96.50%
9	0.5873	96.96%
10	0.3776	97.26%
11	0.3414	97.53%
12	0.2636	97.73%
13	0.2454	97.93%
14	0.2146	98.10%
15	0.2094	98.26%
16	0.1933	98.41%
17	0.1562	98.53%
18	0.1488	98.65%
19	0.1413	98.76%

Figure 37. PCA scree plot obtained considering 55 LST Landsat 8 data. In the table the value of each eigenvalue and the cumulative percentage.

In Figure 38 and Figure 39 the first three PCs for both LST time series are showed.

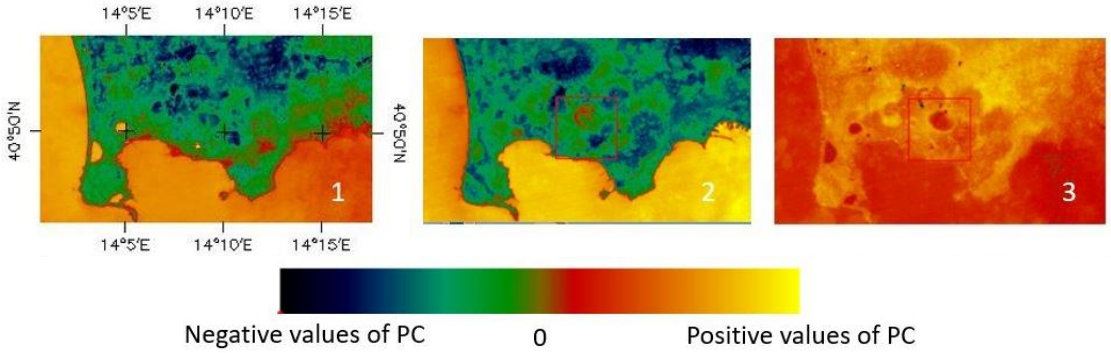

Figure 38. PCA images 1 through 3 derived from LST ASTER time series from 2013 to 2019.

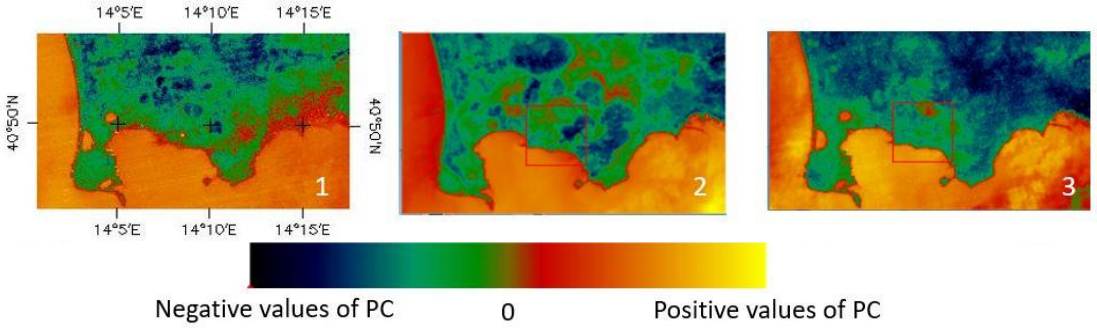

Figure 39. PCA images 1 through 3 derived from LST Landsat 8 time series from 2013 to 2019.

The scatter plot, with density slice colours (Figure 40), of PC1 vs average LST map shows that PC1 furnishes information on mean temporal variation (r=0.999).

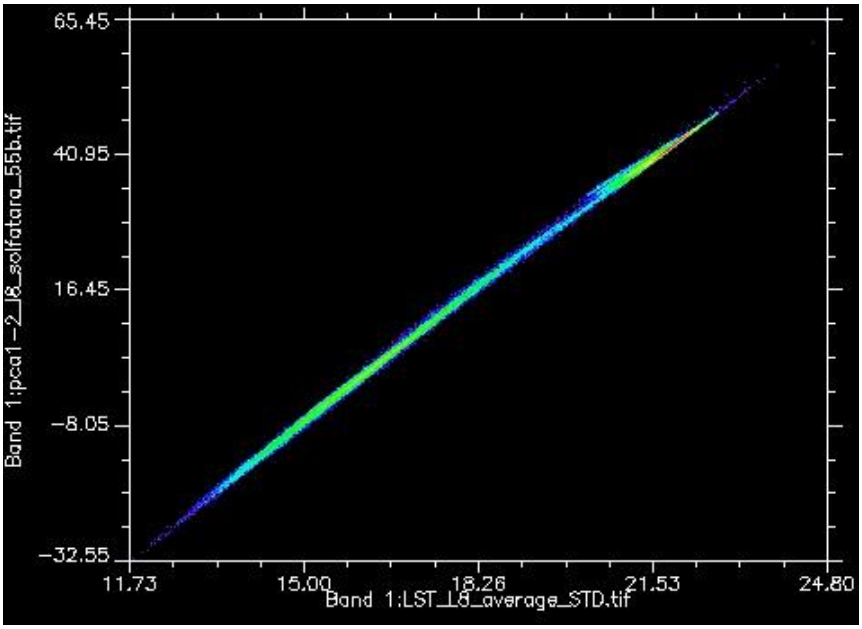

Figure 40. LST average vs PC1 (r = 0.999).

Figure 41 shows the correlation between each of the time-steps with the components being diagrammed as well as the mean temperature at each time-step. No seasonality can be observed for the PC1 (green line in Figure 41) and the loadings are consistent over the entire period. The distribution of the PC2 loadings seems to show a seasonal cycle (positive value during autumn/winter and negative during summer/spring).

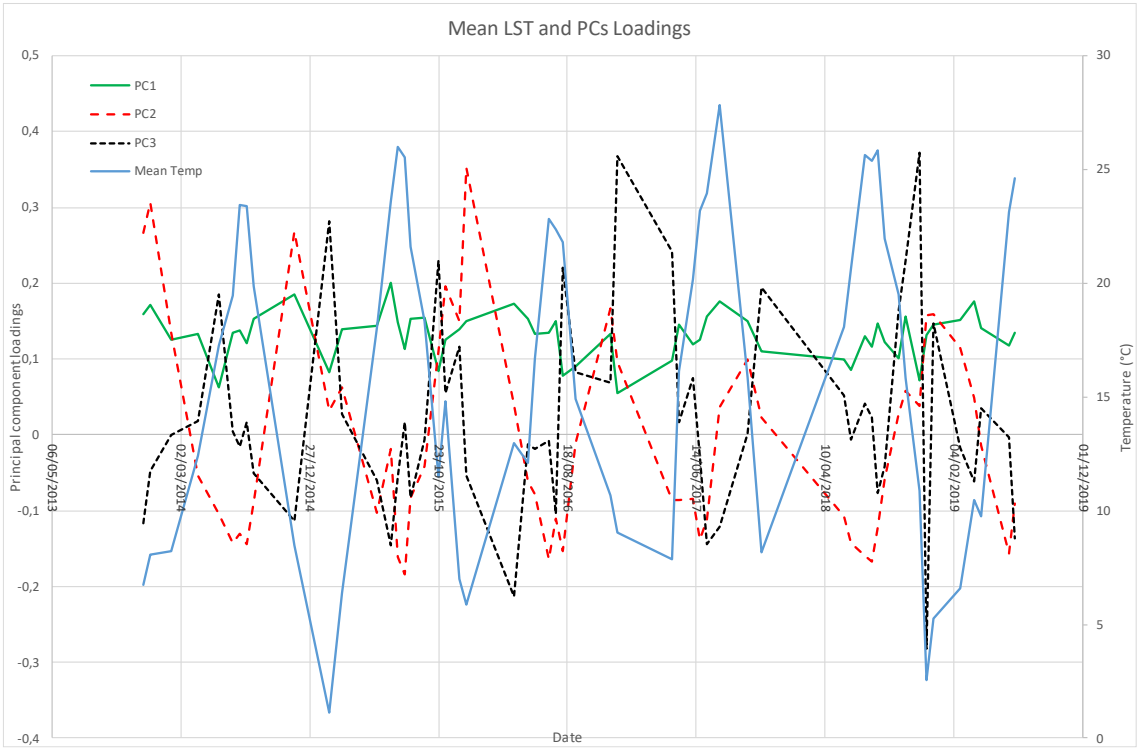

Figure 41. Mean Temperature and Component Loadings (Y-axis) on the original 55 LST Landsat 8 images (X-axis) of the first three principal components. Mean temperature was calculated for each acquisition date.

Moreover, a visual comparison between PC2 and DEM of *Campi Flegrei* area suggests a strong relation between this component and the morphology of the site (Figure 42). In fact, PC2 shows the rims of the main craters visible in the DEM.

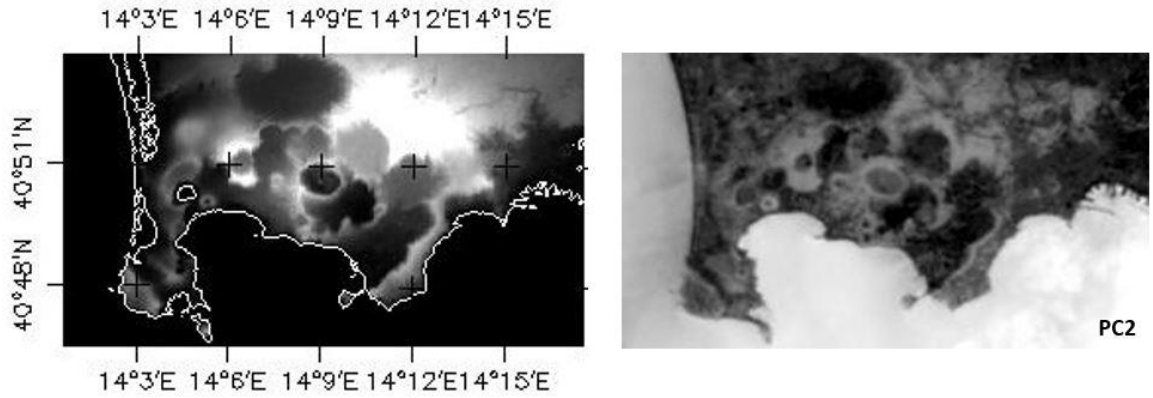

Figure 42. DEM of *Campi Flegrei* area (left) and second principal component of the PCA for the LST time series data (right).

PC1 vs PC2 scatter plot (Figure 43), with density slice colour, evidences an area of sparse points (A in Figure 43) and two main clusters (B and C in Figure 43). The analysis of this plot showed that the sparse area A indicates lake

surface (warm) and *Solfatara* volcano pixels, cluster B is mainly composed by land pixels (urbanized areas and not) and C is mainly composed by sea (warm) pixels.

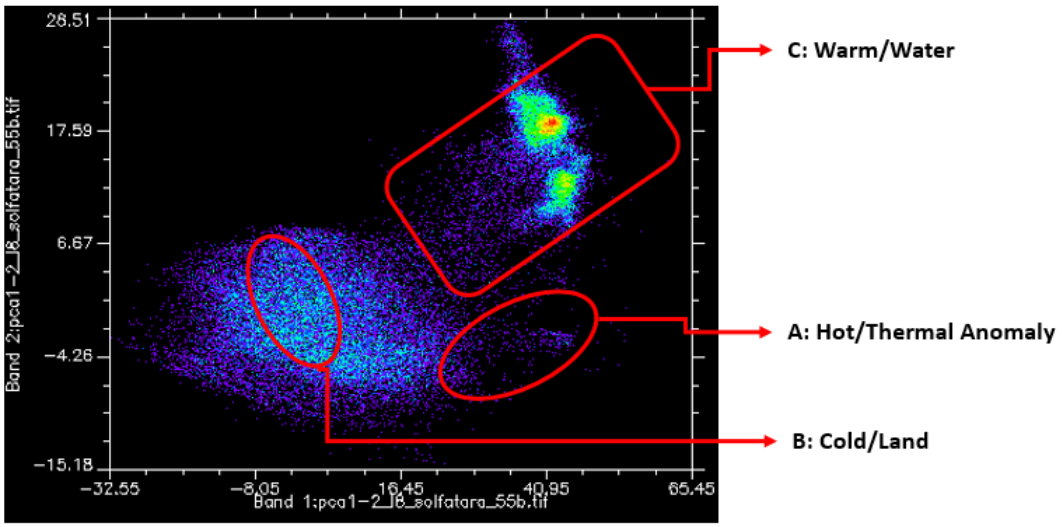

Figure 43. PC1 vs PC2 for Landsat 8 data. The temperature of clusters A is greater than temperature of cluster C that is greater of temperature of cluster B.

Three set of pixels were extracted from the clusters A, B and C, all used as endmembers for the maximum likelihood classification. The points of A class cover the *Solfatara* volcano area and the lake area (*Fusaro*, *Lucrino*, *Miseno* and *Averno*) and they have a temperature greater than the land during the night (Figure 44). The B and C classes obtained by the classification represent the land and sea, respectively, where C appears hotter than B.

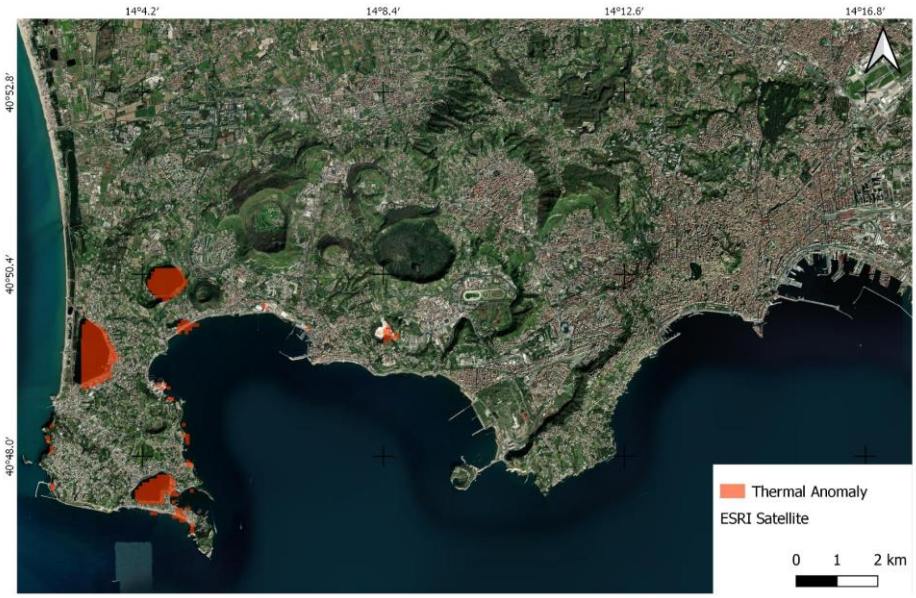

Figure 44. The areas represent the results of the maximum likelihood classification using the cluster A on Landsat 8 data.

For what concerns the LST estimated by ASTER data, similar considerations can be done (Figure 45), considering also the fact that the mean temperature is very close to the one estimated with Landsat 8 (Figure 36). Also in this case, points of A class cover the *Solfatara* volcano area and the lake area (Figure 46).

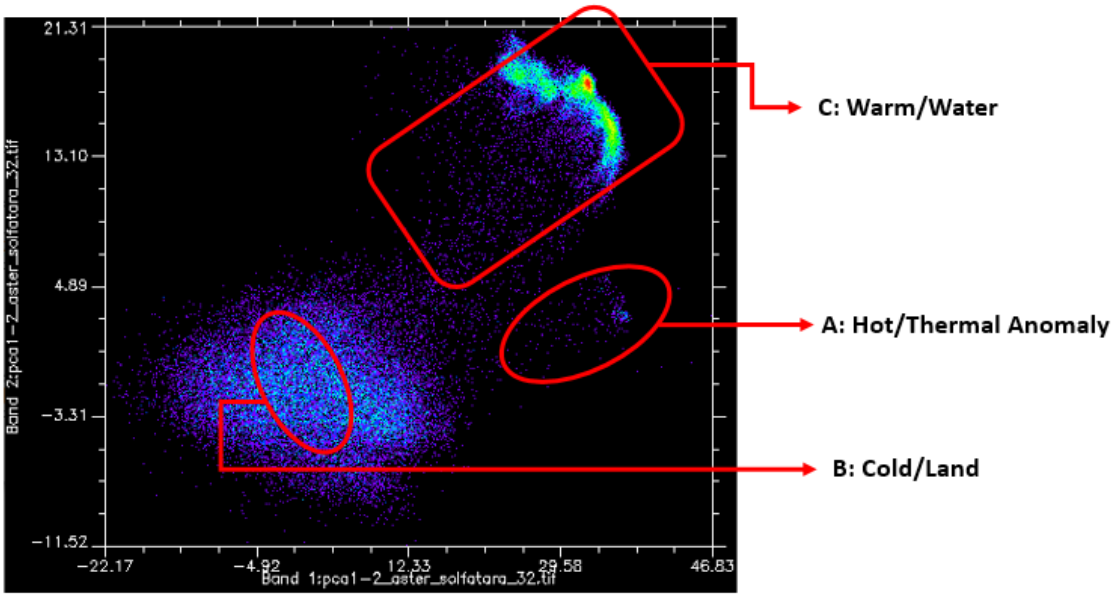

Figure 45. PC1 vs PC2 for ASTER data. The temperature of clusters A is greater than temperature of cluster C that is greater of temperature of cluster B.

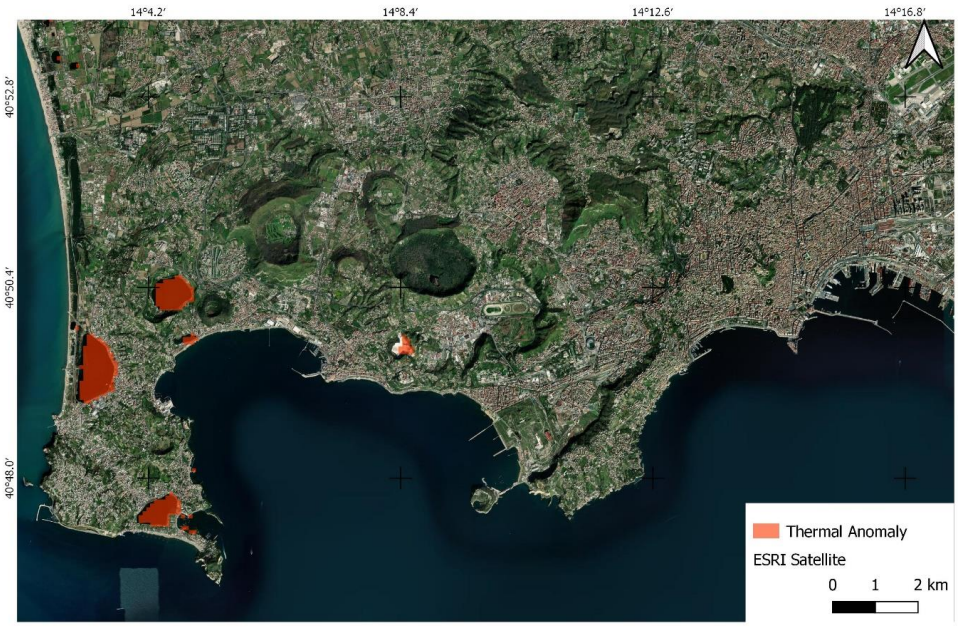

Figure 46. The areas represent the results of the maximum likelihood classification using the cluster A on ASTER data.

Analysing the result obtained, the comparison with soil temperature monitored by INGV [91] during dedicated field campaign, is presented. In particular, it is important to underline that the soil temperatures collected during these surveys have been sampled at a depth of 10 cm using a thermocouple sensor while the LST estimated by satellite for each pixel has referred to a spatial resolution of 90m. Moreover, the soil temperature is not inferred by any external influences while LST could include noises despite they have been atmospherically corrected.

Observing the result obtained, it is evident that the mean LST area (Figure 36) in *Solfatara* area is coherent with the mean of soil temperature (Figure 47) [91] in the same temporal range (2016-2019). LST surface temperatures (20–25°C) are coherent with those measured in the soil (10–85°C at 10 cm depth) in consideration with the limitations of estimation method. Remotely sensed temperatures result lower than measured ones, the latter being measured at a depth of 10 cm and hence increased by high thermal gradients of the soil in the hottest zones. Moreover, as showed in Figure 47, the analysis of thermal anomalies spatial distribution for both satellite and soil temperature is similar.

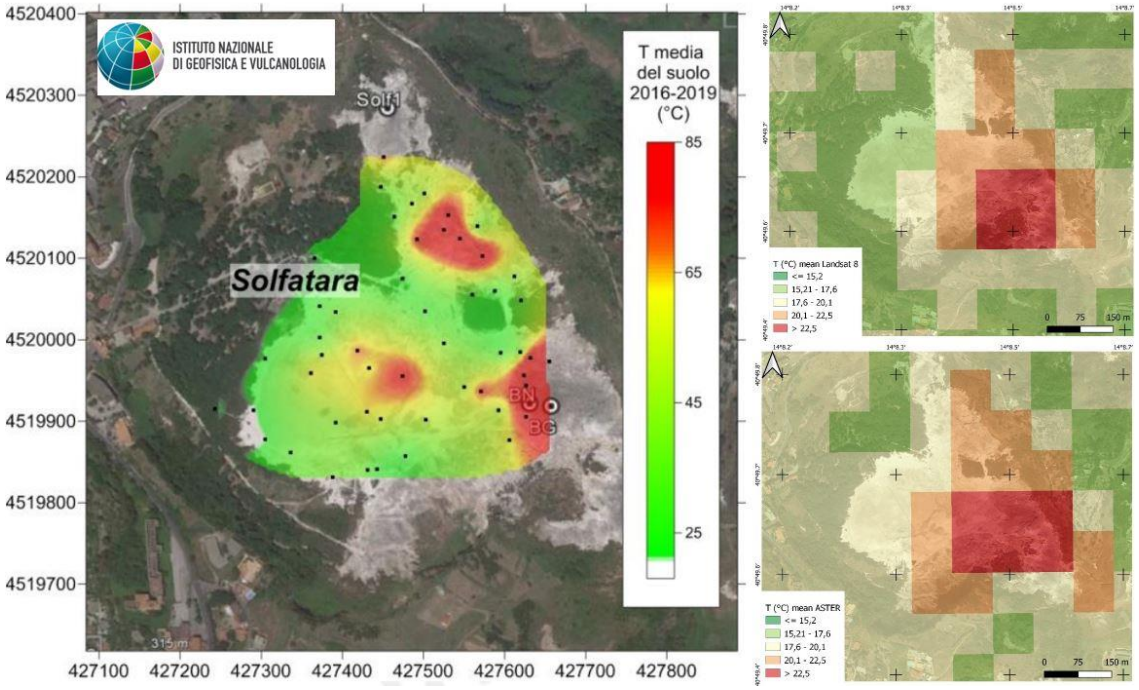

Figure 47. Soil temperature on *Solfatara* test site [91] and LST averages for Landsat 8 (up) and ASTER (down) data.

These observations indicate that in the *Campi Flegrei* area the *Solfatara* volcanic center is characterized by the higher temperatures of the area. These

evidences agree with the intense volcanic degassing activity which is strongly clustered in the *Solfatara* area. Finally, in the observed period, no unknown thermally anomalous areas related to volcanic activity are highlighted in other sectors of *Campi Flegrei*.

The result obtained by using PCA (Figure 44 and Figure 46) are in agreement with the ones obtained using a different methodology as described in [71]. In particular, in [71], the process of removing the seasonal component of temperature time-series is considered. The existence of thermally anomalous area in the *Campi Flegrei* site is analysed by considering the land surface Median Temperature values greater than a Threshold Value (MTTV) on de-seasonalised time series. In [71], the threshold values of +1σ (16.36 °C for ASTER and 17.01 °C for Landsat 8) , +1.5 σ (17.19 °C for ASTER and 18.02 °C for Landsat 8) and +2σ (18.03 °C for ASTER and 19.04 °C for Landsat 8) allowed to obtain the results showed in Figure 48.

The use of PCA confirms that the process of removing seasonality, applied in MTTV (Figure 48), is not necessary. The spatial distribution of thermal anomalies detected using PCA and MTTV is coincident as showed in Figure 44, Figure 46 and Figure 48.

A further consideration demonstrating that satellite data can be a very powerful tool to study surface thermal anomalies quantitatively can be done by comparing the radiant power output estimated using LST time series and with the one estimated in Marotta et al, 2019 [92].

In particular, for *Solfatara* volcano area the total radiant power Q (W) was calculated from the Stefan-Boltzmann law on a pixel-by-pixel basis.

$$Q = A * \sigma * \varepsilon * T^4 \qquad (11)$$

where A is the satellite pixel size (8100 m^2), σ = 5.67 * 10^{-8} W $m^{-2}K^{-4}$ (Stefan-Boltzman constant), ε is the surface emissivity and T (K) the mean of LST estimated by remote sensor from the 2013 to 2019 (Figure 36).

In their study, [92] computed the heat flux over the investigated area (Figure 49) during nighttime field campaigns and estimate, in the same area, a total radiant power Qtot=22±4MW on the surface. Figure 50 and Figure 51 represent the heat flux estimated by Landsat 8 and ASTER using eq. 11, dividing it for the area A. The two maps of heat flux derived by Landsat 8 and ASTER are over plotted on Figure 49.

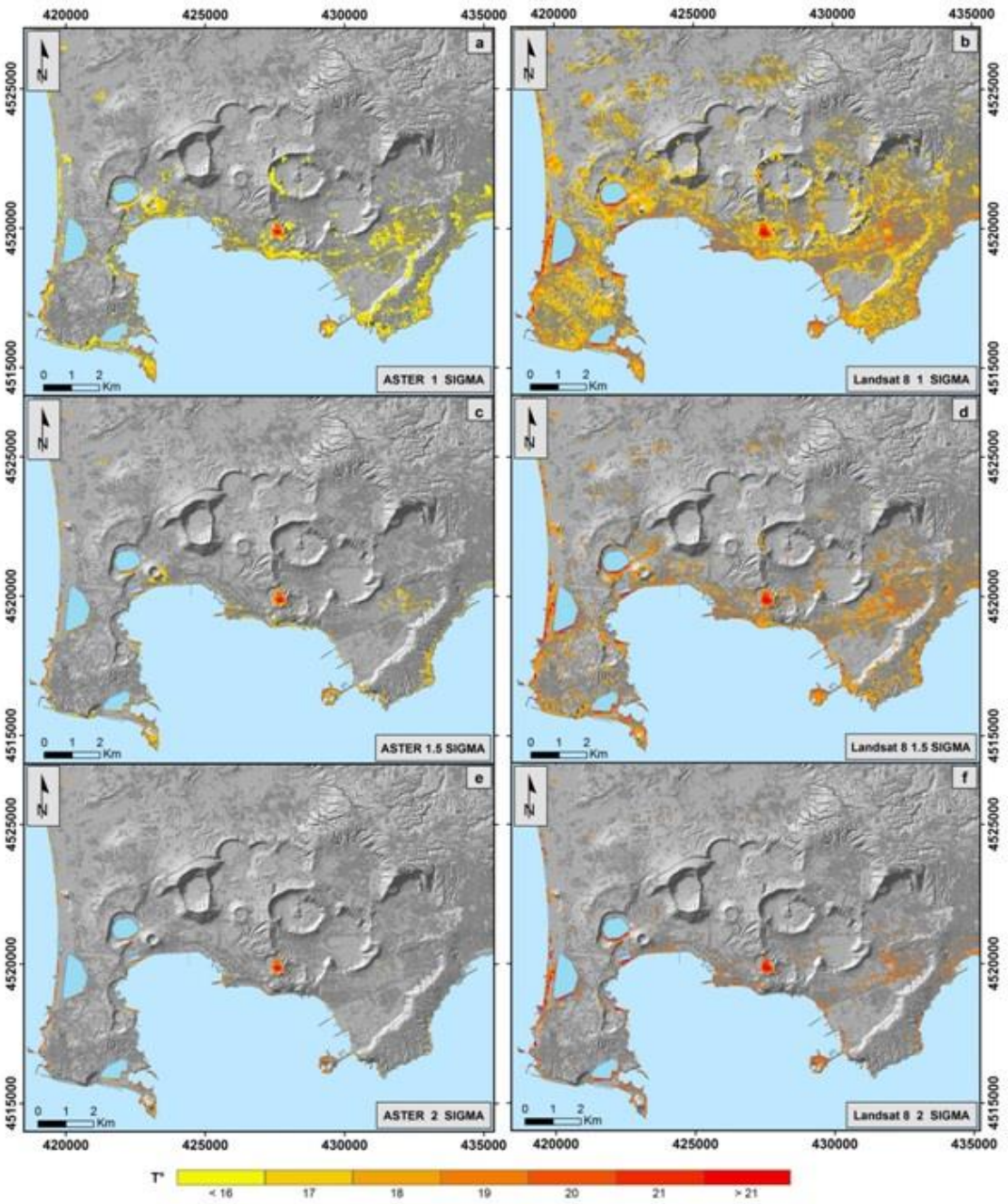

Figure 48. Maps of MTTV of temperature satellite frame with temperature threshold at +1σ (a, b); +1.5σ (c, d); 2σ (e, f), reported in [71].

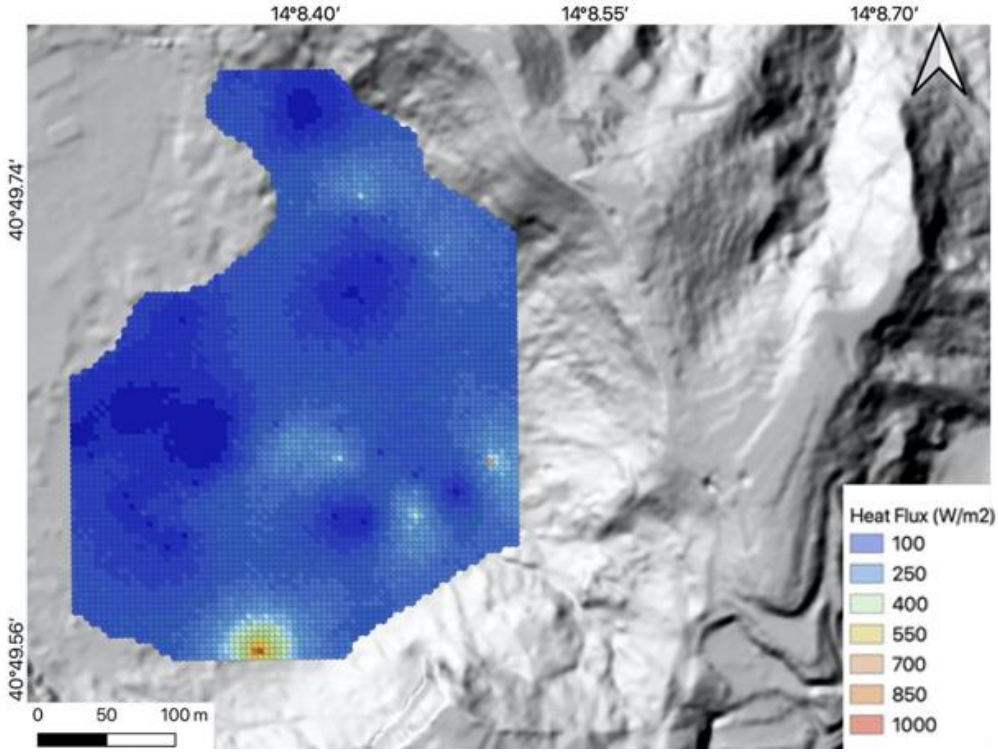

Figure 49. Map of the calculated heat flux distribution over the investigated area using points sampled during nights (modified after [92]).

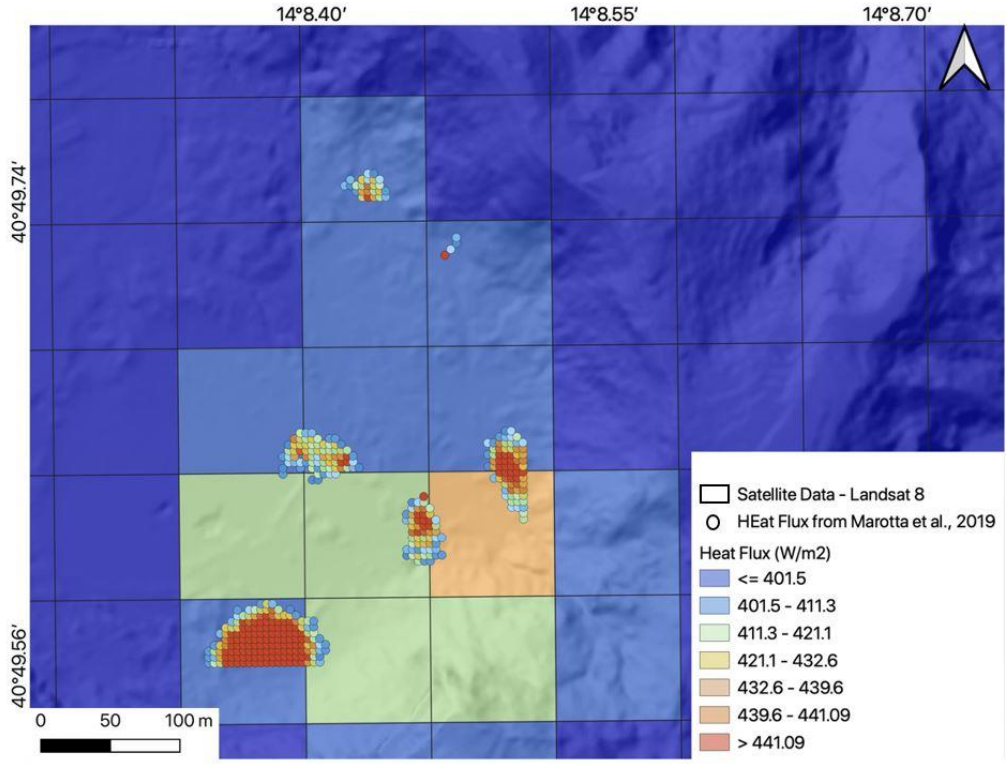

Figure 50. Heat flux distribution estimated by Landsat 8 LST. The satellite map is over plotted on Figure 49. The heat flux measured by [92] is represented in circle. The heat flux value color is referred to in situ and satellite measurements, respectively.

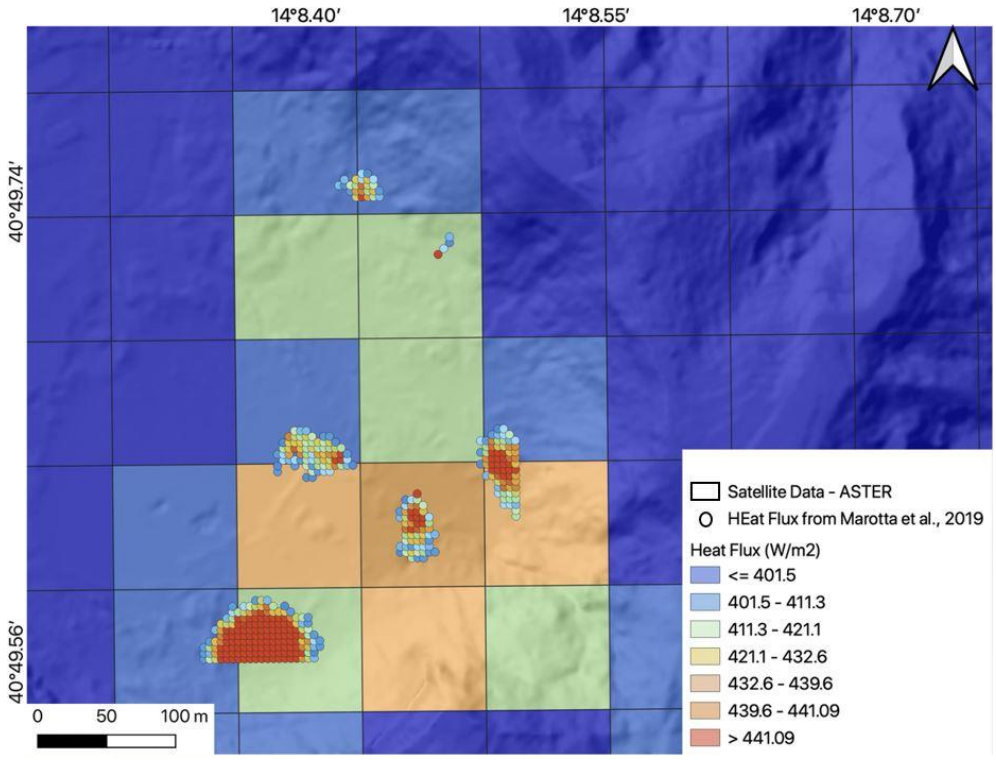

Figure 51. Heat flux distribution estimated by ASTER LST. The satellite map is over plotted on Figure 49. The heat flux measured by [92] is represented in circle. The heat flux value color is referred to in situ and satellite measurements, respectively.

The pixel observed by the sensor includes some (few, may be only one) thermal anomalies (Figure 52). Denoting:

Q_0: Total radiant power emitted by the pixel (W)

Q_a: Total radiant power emitted by the thermal anomalies (W)

Q_b: Total radiant power emitted by the background (surface not covered by thermal anomaly) (W)

A: Total pixel area (the single pixel ASTER area, 8100 m^2)

a: Thermal anomalies area (included in the pixel)

T_0: remote sensing temperature (derived by eq. 5) $[K]$

T_b: background temperature (mean) $[K]$

T_a: anomalies temperature (mean) $[K]$

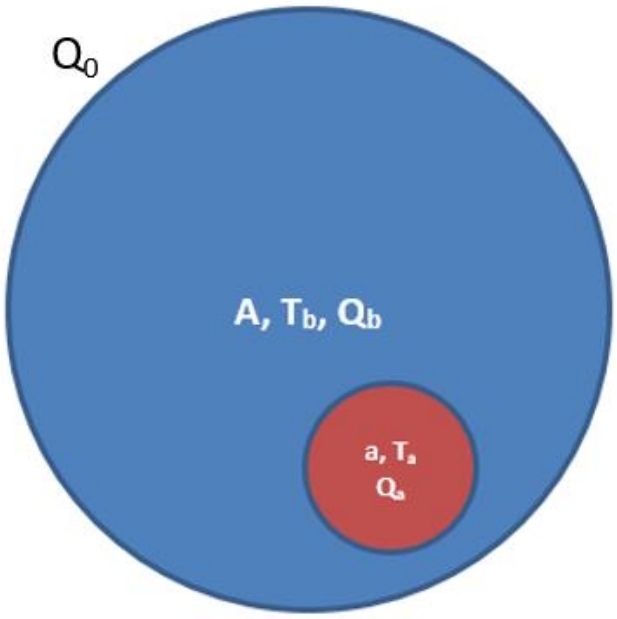

Figure 52. ASTER pixel (blue) and thermal anomaly (red).

Two main investigation can be done:

1) considered that $a \ll A$, do thermal anomalies produce an observable rise of the background temperature?
2) Is it possible to estimate the radiant power emitted by thermal anomalies?

For simplicity, let $\varepsilon = 1$ and assume that $A \gg a$. Q_0 (Figure 53) is so obtained:

$$Q_0 = Q_b + Q_a \qquad (12)$$

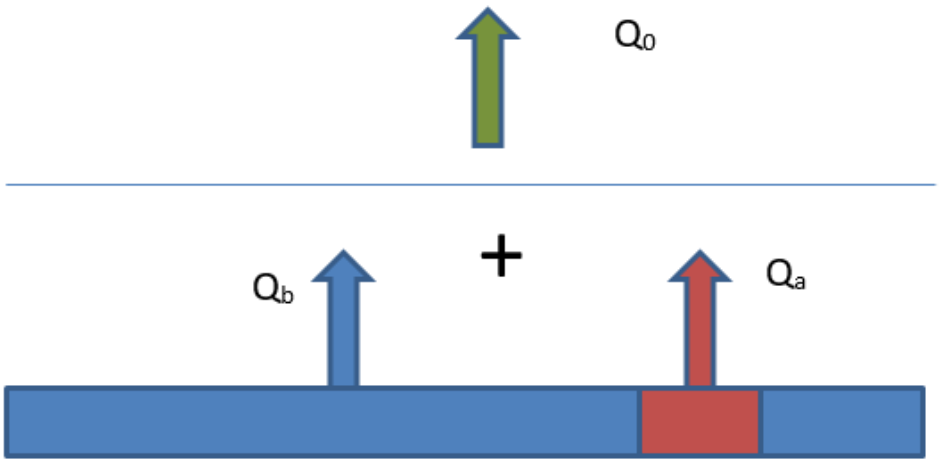

Figure 53. Radiant power estimated by satellite for a single pixel, Q_0, that is the sum of radiant power of background area (Q_b) and radiant power of thermal anomaly(Q_a).

Referring to eq. 11:

$$A\sigma T_0^4 = A\sigma T_b^4 + a\sigma T_a^4 \qquad (13)$$

Dividing for the area A,

$$T_0^4 = T_b^4 + \left(\frac{a}{A}\right) T_a^4 \qquad (14)$$

Using typical values deduced from Figure 36 and considering the two main thermal anomalies in *Solfatara*, *Bocca Grande* and *Bocca Nuova*:

$$T_b = 17°C \simeq 290K$$

$$T_a = 180°C \simeq 453K$$

$$a = 25\ m^2 \text{ (small anomaly, } 5m\ x\ 5m)$$

$$A = 8100\ m^2 \text{ (ASTER pixel)}$$

We obtain:

$$\left(\frac{a}{A}\right) = 3.09 \cdot 10^{-3}$$

$$T_b^4 = 7.07 \cdot 10^9\ K^4$$

$$T_a^4 = 4.21 \cdot 10^{10} K^4$$

$$T_0^4 = 7.07 \cdot 10^9 K^4 + 3.09 \cdot 10^{-3} \cdot\ 4.21 \cdot 10^{10} K^4 =\ 7.20 \cdot 10^9 K^4$$

$$T_0 = 291.3\ K$$

This result gives the answer to the point 1): the presence of a single, small anomaly produces a temperature rise greater than $1K$, i.e. it is observable in the LST maps obtained by ASTER.

The radiant power emitted by thermal anomaly is:

$$Q_a = Q_0 - Q_b$$

$$Q_a = A\sigma T_0^4 - A\sigma T_b^4 = A\sigma(T_0^4 - T_b^4)$$

using the values above:

$$Q_a = 8100\ m^2 \cdot 5.67 \cdot 10^{-8}\ \frac{\mathrm{W}}{\mathrm{m}^2 K^4}(291.3^4 K^4 - 290^4\ K^4) = 5.86 \cdot 10^4 W$$

$$Q_b = 8100\ m^2 \cdot 5.67 \cdot 10^{-8}\ \frac{\mathrm{W}}{\mathrm{m}^2 K^4} 290^4 K^4 = 3.25 \cdot 10^6 W$$

$$Q_0 = 8100\ m^2 \cdot 5.67 \cdot 10^{-8}\ \frac{\mathrm{W}}{\mathrm{m}^2 K^4} 291.3^4 K^4 = 3.31 \cdot 10^6 W$$

That is (point 2), Q_a contributes about 2% to the radiant power estimated by ASTER. This means that radiant power of thermal anomalies can be estimated by ASTER but, given its low contribution, a methodology more accurate than that used above must be used, as, for example, that used in [92].

To compare the results of this investigation with the results obtained [92], the radiant power Q_0 must be summed for all the ASTER pixels included the thermal area. i.e. about 7 pixels (Solfatara area, [92]):

$$Q_{0,7\mathrm{pixel}} = 7 \cdot 3.31 \cdot 10^6 W = 23.17\ MW$$

This estimate is coherent but with the value estimated using the ASTER LST image (Figure 36), i.e. about 25MW and with the estimate of Qtot=22±4MW reported in [92].

The long satellite data set already analysed represents an invaluable resource to investigate the thermal history of active volcanoes and, in particular, of those that recently erupted. At *Solfatara-Campi Flegrei*, where an ongoing heating process has been highlighted by classical monitoring techniques since 2012, the satellite data can provide a supplemental tool to monitor the thermal evolution of this dangerous area.

Concerning the LST time series, it can reasonably state that the strong agreement between the TIRNet stations and satellite data starting from 2013 can validate the methodology for the evaluation of temperature by using satellites. Even if no ground measurements are available before 2013, the agreement showed in Figure 20 allows to extend the validity of the LST time series backward. Moreover, this agreement, even if verified only on *Solfatara* area, offers the possibility to enlarge the LST estimation considering the whole satellite frame. For this reason, it is possible to apply the methodologies described in this thesis also in remote areas or where ground monitoring is not available or absent. A further consideration can be done about the costless of this solution because it is based on data that are free of charge.

5.3 Application on *Parco delle Biancane* area

A similar approach of *Solfatara-Campi Flegrei* has been adopted for *Parco delle Biancane* area.

LST time series images have been obtained and analysed. Two maps have been obtained by averaging the 40 LST maps for Landsat 8 and 20 LST maps for ASTER data respectively (Figure 54).

The mean LSTs estimated with Landsat 8 (Figure 54 right side) ranges from 12 °C to 20 °C, with an average of 14 °C and a maximum of about 20 °C inside the *Parco delle Biancane* area. The mean LSTs estimated with ASTER (Figure 54 left side) range from 9 °C to 18 °C, with an average of 12 °C and a maximum of about 18 °C inside the *Parco delle Biancane* area.

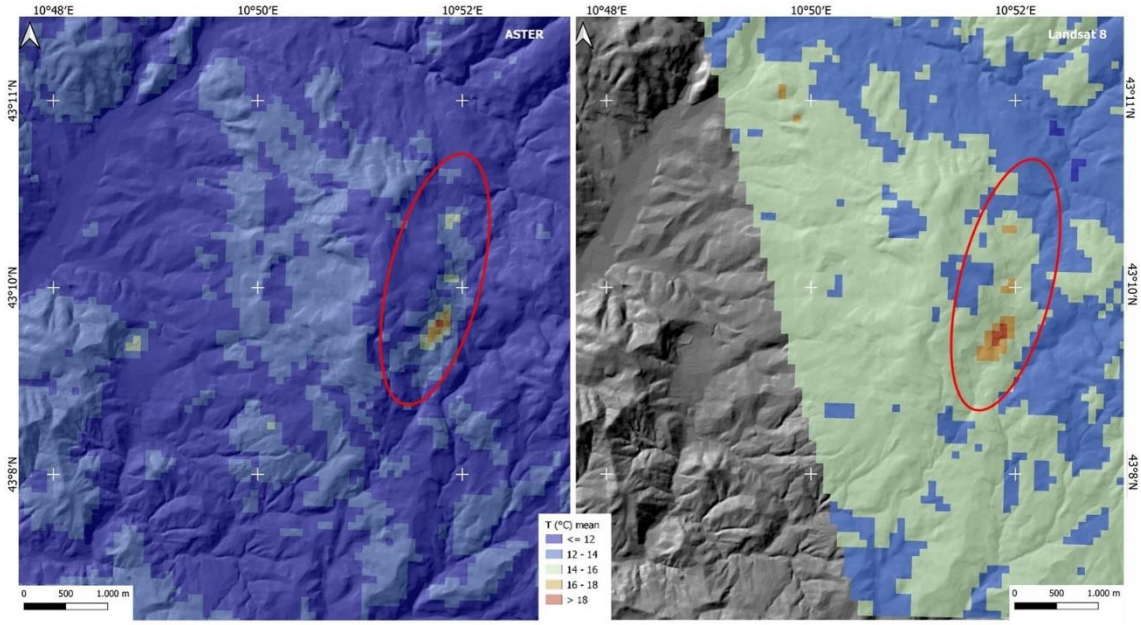

Figure 54. Mean LST obtained by processing ASTER (left) and Landsat 8 (right) LST data. In the red circle the *Parco delle Biancane* area is identified.

In Figure 55 the main areas to investigate are reported.

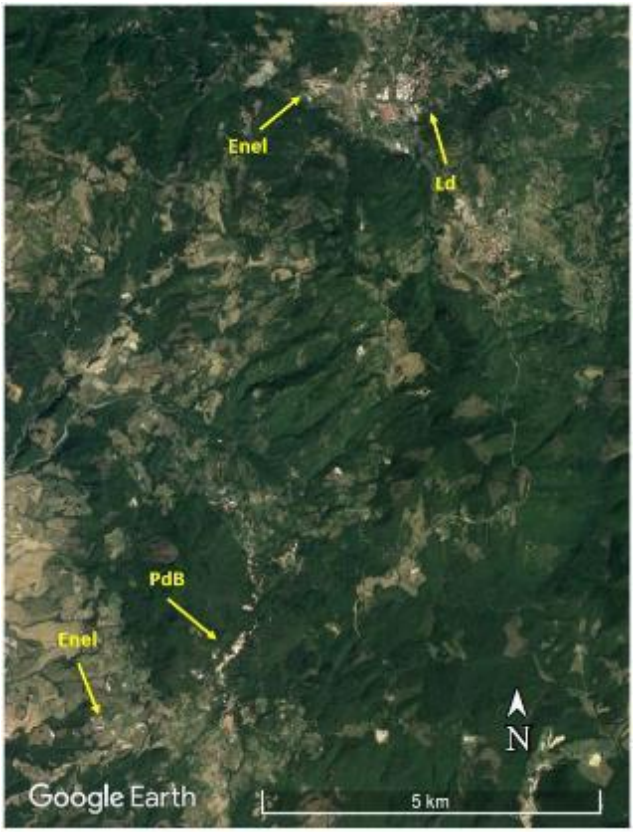

Figure 55. Studied area. Pdb - *Parco delle Biancane* geothermal area; Enel-ENEL GREEN POWER central renewable energy; Ld-*Larderello* area.

To refine this analysis, the same procedure implemented for *Solfatara-Campi Flegrei* in 5.2 and using PCA has been done.

Concerning Landsat 8 LST data, the eigenvalues of the transformation show that PC1 describes the majority, 55% of the information across time, PC2 and PC3 contributions are 13 and 6%, the other PCs have a low weight (Figure 56). In Figure 57 and Figure 58 the first three PC components are reported [93-95].

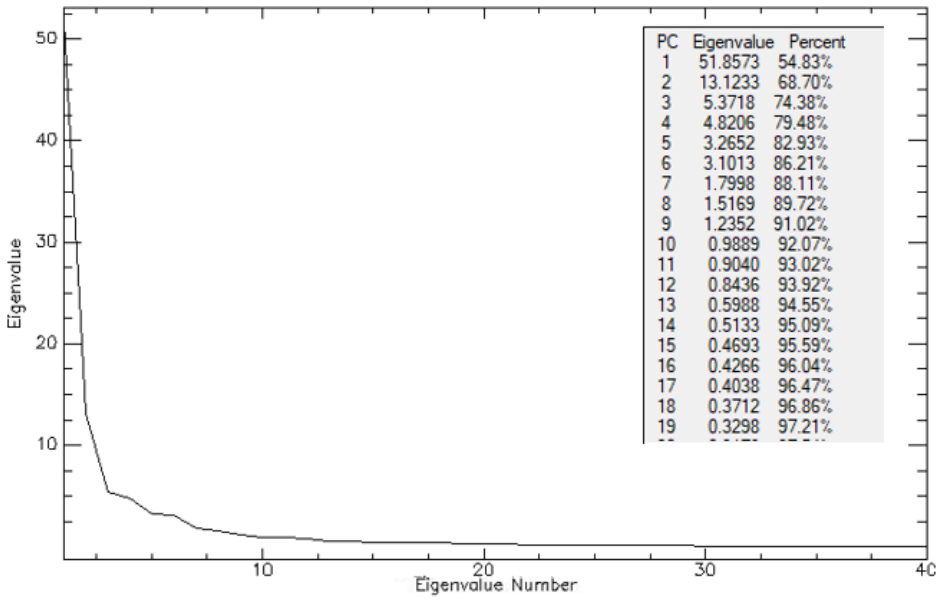

Figure 56. PCA scree plot obtained considering 40 LST Landsat 8 data. In the table the value of each eigenvalue and the cumulative percentage.

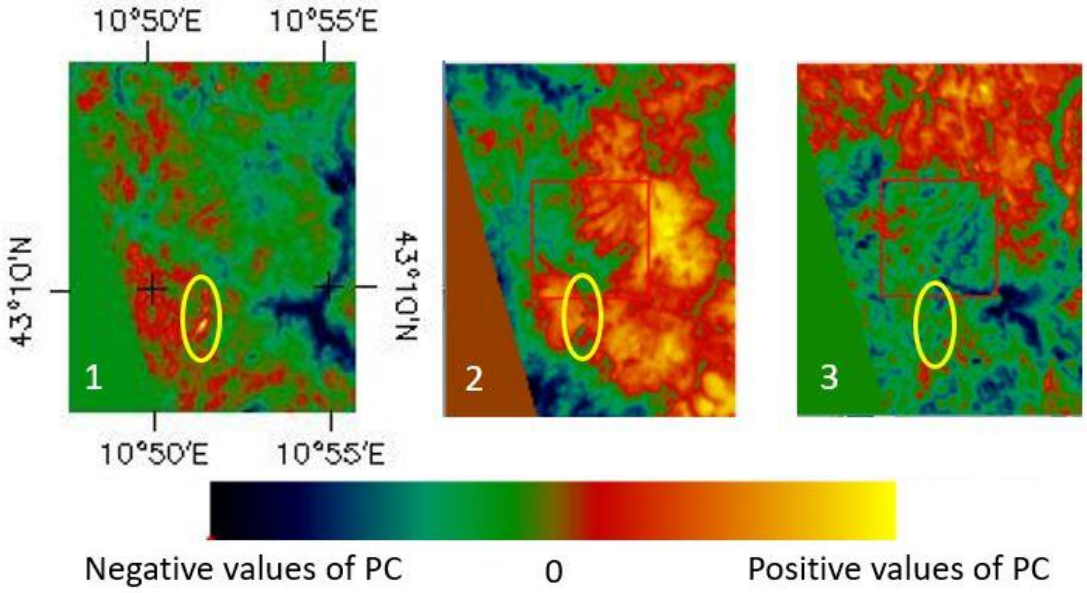

Figure 57. PCA images 1 through 3 derived from LST Landsat 8 time series from 2013 to 2020. In the yellow circle the *Parco delle Biancane* area is identified.

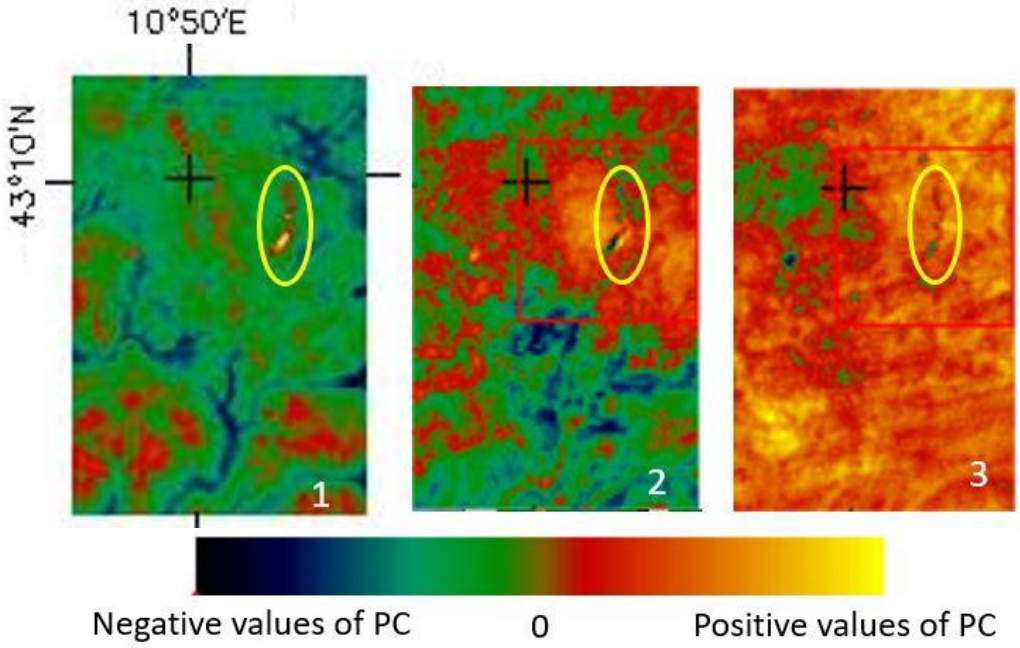

Figure 58. PCA images 1 through 3 derived from LST ASTER time series from 2002 to 2020. In the yellow circle the *Parco delle Biancane* area is identified.

The scatter plot, with density slice colours (Figure 59), of PC1 vs average LST map shows that PC1 furnishes information on mean temporal variation (r=0.995270).

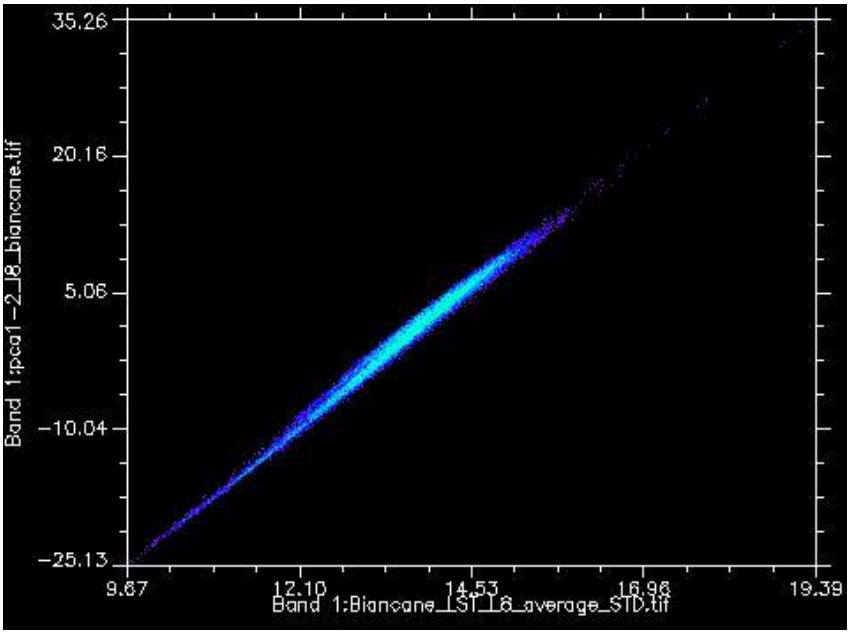

Figure 59. LST average vs PC1 (r = 0.995270).

Also in this case, as analysed in *Campi Flegrei* area, Figure 60 shows the correlation between each of the time-steps with the components being diagrammed as well as the mean temperature at each time-step. Also in this case, no seasonality can be observed for the PC1 (green line in Figure 60) and the loadings are consistent over the entire period. The distribution of the PC2 loadings seems to show a seasonal cycle (positive value during autumn/winter and negative during summer/spring).

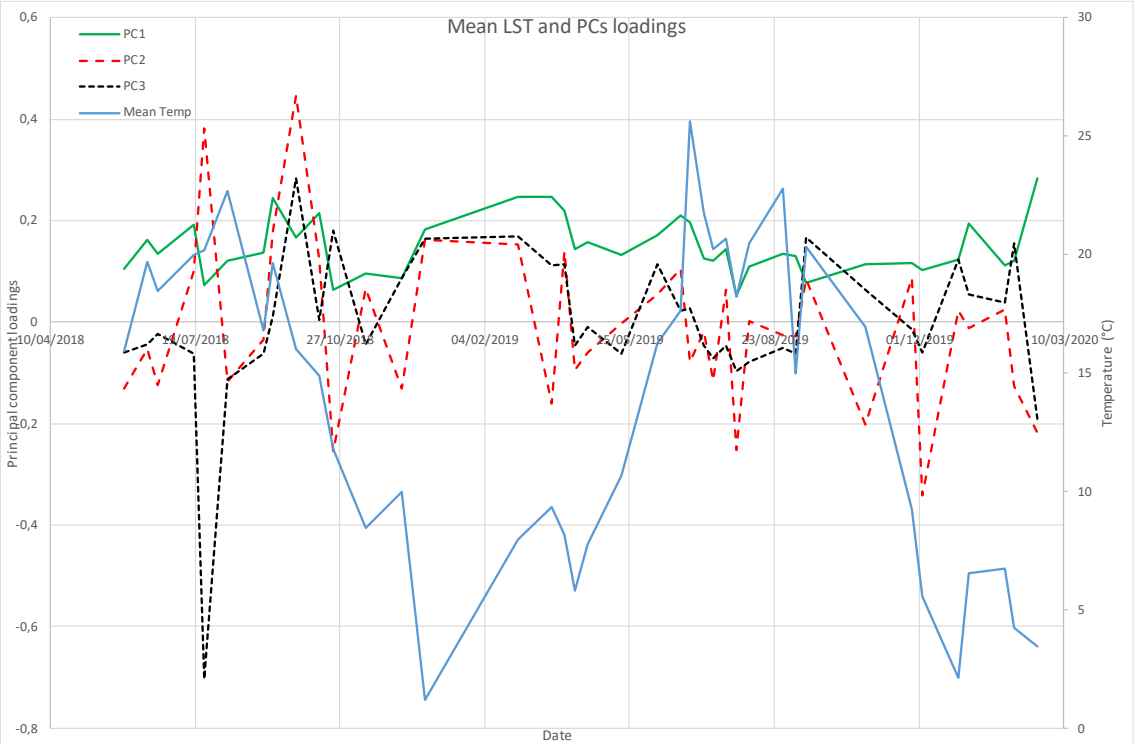

Figure 60. Mean Temperature and Component Loadings (Y-axis) on the original 40 LST Landsat 8 images (X-axis) of the first three principal components. Mean Temperature was calculated for each acquisition date.

Also in this case, as already considered in 5.2, a comparison between PC2 and DEM of *Parco delle Biancane* area suggests a strong dependence between this component and the morphology of the site (Figure 61).

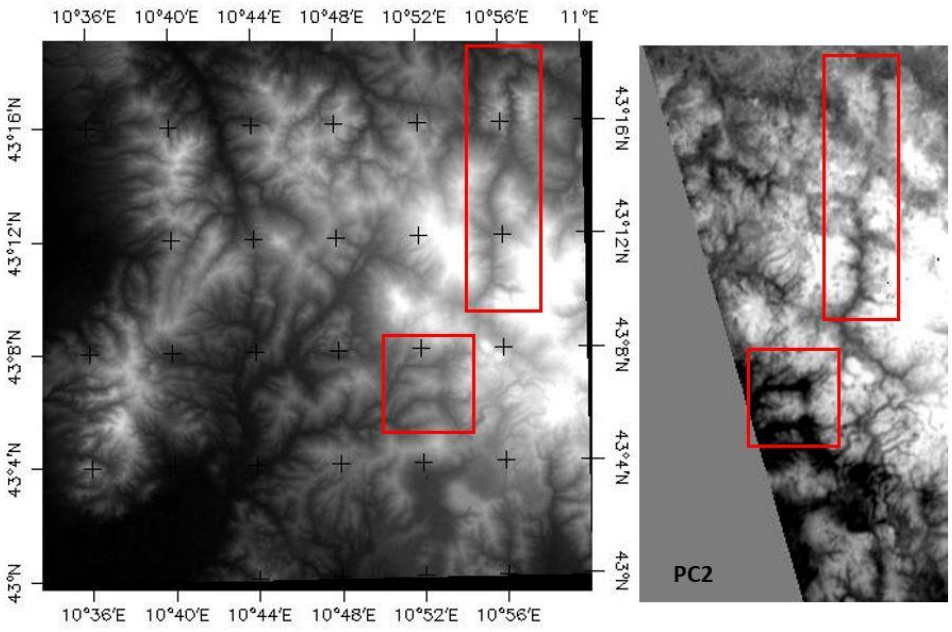

Figure 61. DEM of *Parco delle Biancane* area (left) and second principal component of the PCA for the LST time series data (right). In the red boxes some features are showed for an easily comparison.

PC1 vs PC2 scatter plot (Figure 62), with density slice colour, evidences an area of sparse points (A in Figure 62) and two clusters (B and C in Figure 62). The analysis of this plot showed that the sparse area A indicates hottest surface due to thermal anomalies and bare soil, the cluster B is mainly composed by vegetated areas corresponding to flank and hilltop (and also presence of small villages) and cluster C is mainly attributed to vegetated area with colder temperature typical of gorges and narrower valley.

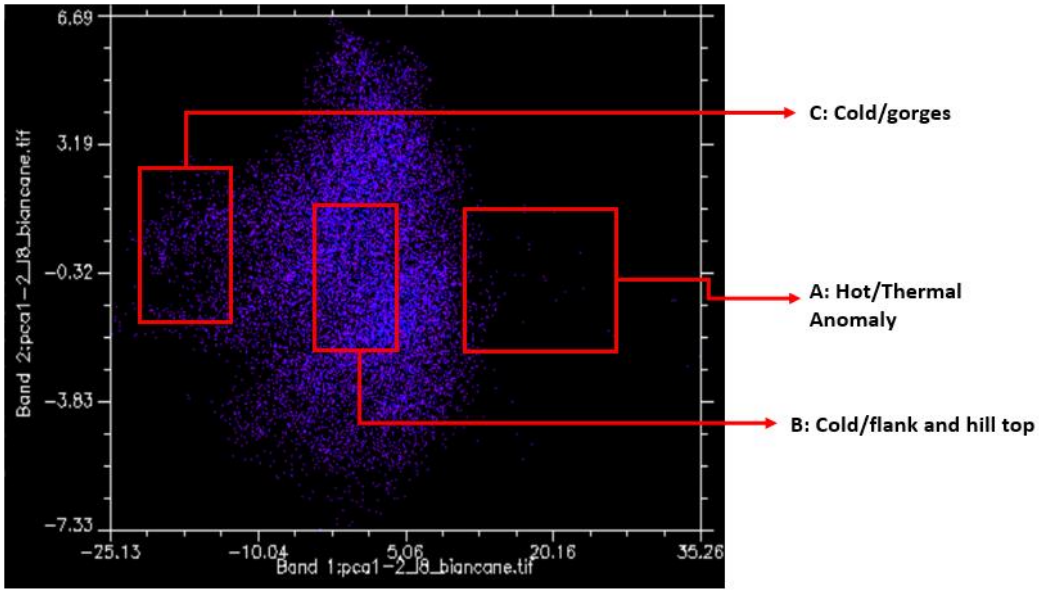

Figure 62. PC1 vs PC2 for Landsat 8 data: Clusters.

Three set of pixels were extracted from the clusters A and B and from the area C and used as endmembers for the maximum likelihood classification. The points of A class cover the *Parco delle Biancane* geothermal areas that has a temperature greater than the surrounding during the night. Moreover, the *Valle Secolo* and *Nuova San Martino* Enel Green Power central are also detected. Even if in the area analysed there are several geothermal centrals [96,97], the two power plants detected as "thermal anomaly" together with *Parco delle Biancane* area are, indeed, those with a high rated power. In the Table 17 the main central in the *Larderello* areas are reported. The B and C classes obtained by the classification have been extracted and confirm the background areas.

Power Plant Name	**Year Commissioned**	**No. of Units**	**Unit Rating** MW_e	**Total Installed Cap.** MW_e	**Annual Energy Produced 2008 GWh/yr**
Valle Secolo	1991	2	60	120	893
Nuova Larderello	2005	1	20	20	126.9
Nuova Sasso	1996	1	20	20	126.5
Le Prata	1996	1	20	20	126.7
Nuova Monterotondo	2002	1	10	10	63.5
Nuova San Martino	2002	1	40	40	332.5
Nuova Molinetto	2002	1	20	20	132.3
Carboli 2	1997	1	20	20	125.6

Table 17. Utilization of geothermal energy for electric power generation as of 31 December 2008. Table modified from [96]. The value of Annual Energy produced are relative to 2008.

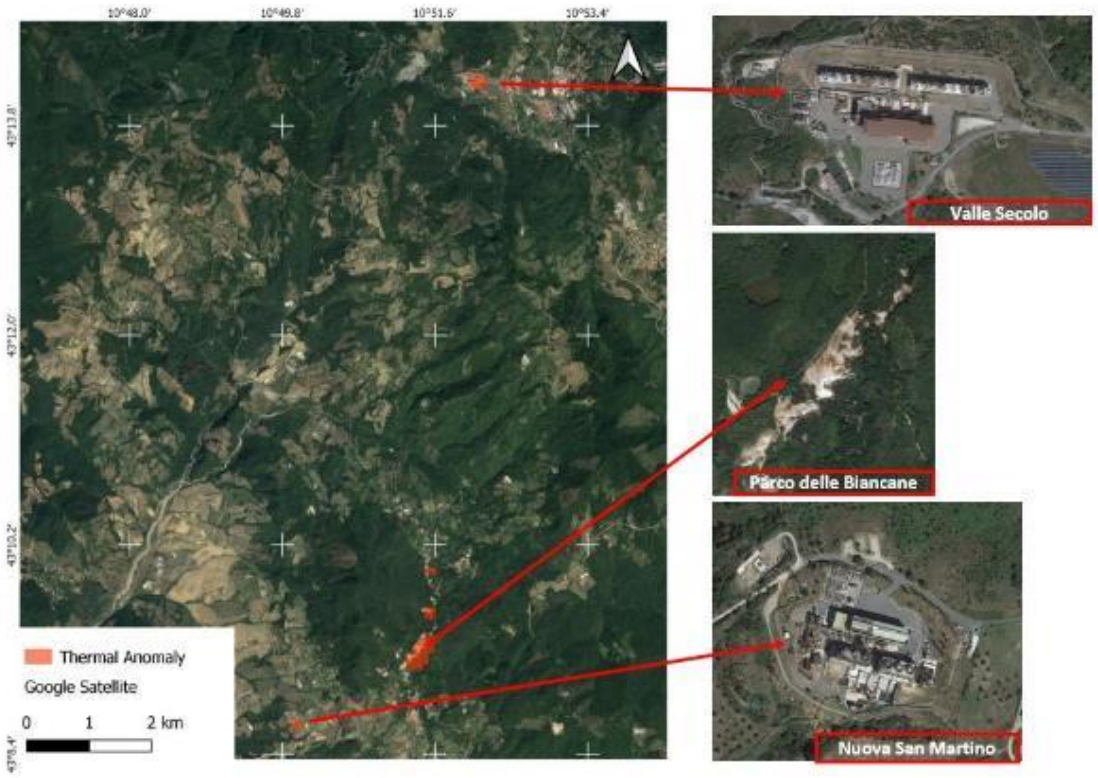

Figure 63. Landsat 8 - The red polygons represent the results of the maximum likelihood classification using the cluster A**.**

For what concerns the LST estimated by ASTER data, similar considerations can be done, considering also the fact that the mean temperature is very close to the one estimated with Landsat 8. For this reason also the PC1 vs PC2 scatter plot (Figure 64) is very similar to Figure 62 . Since the acquisition frame of two sensors is not the same, for ASTER the only *Parco delle Biancane* has been analysed. In Figure 65 the results of analysis are reported.

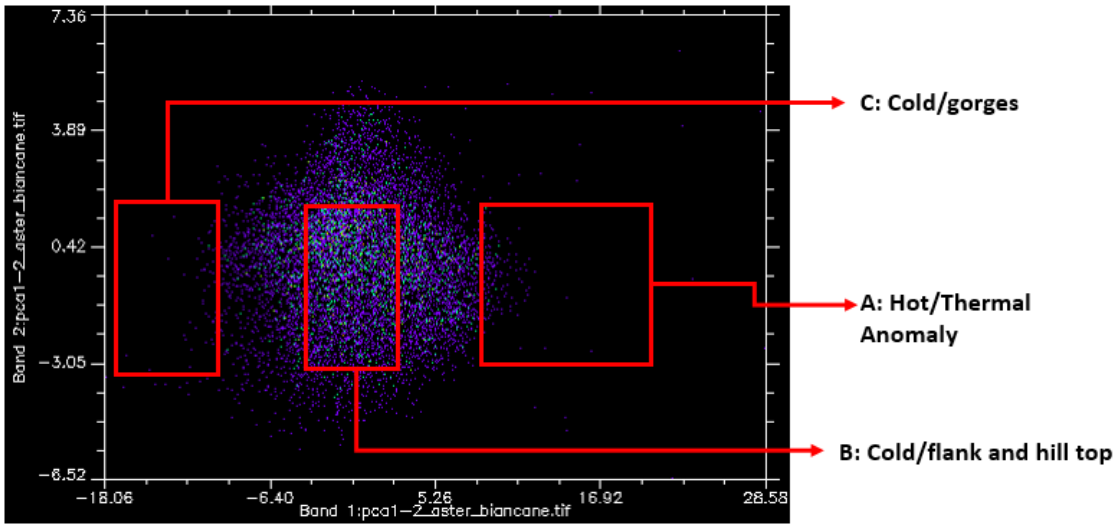

Figure 64. PC1 vs PC2 for ASTER data: Clusters.

The analysis of the LST images furnished indications on the spatial distribution of the mean night time LST. Observing the result obtained, it is evident that the areas are coherent with the known geothermal areas [98]. Considering that all remotely derived values are underestimates, primarily due to sub-pixel thermal mixing and occasional steam interference from venting thermal features, the visual evidence of increasing vegetation stress (e.g., the browning of trees) is likely to be detected sooner than anomalous increases in thermal emission.

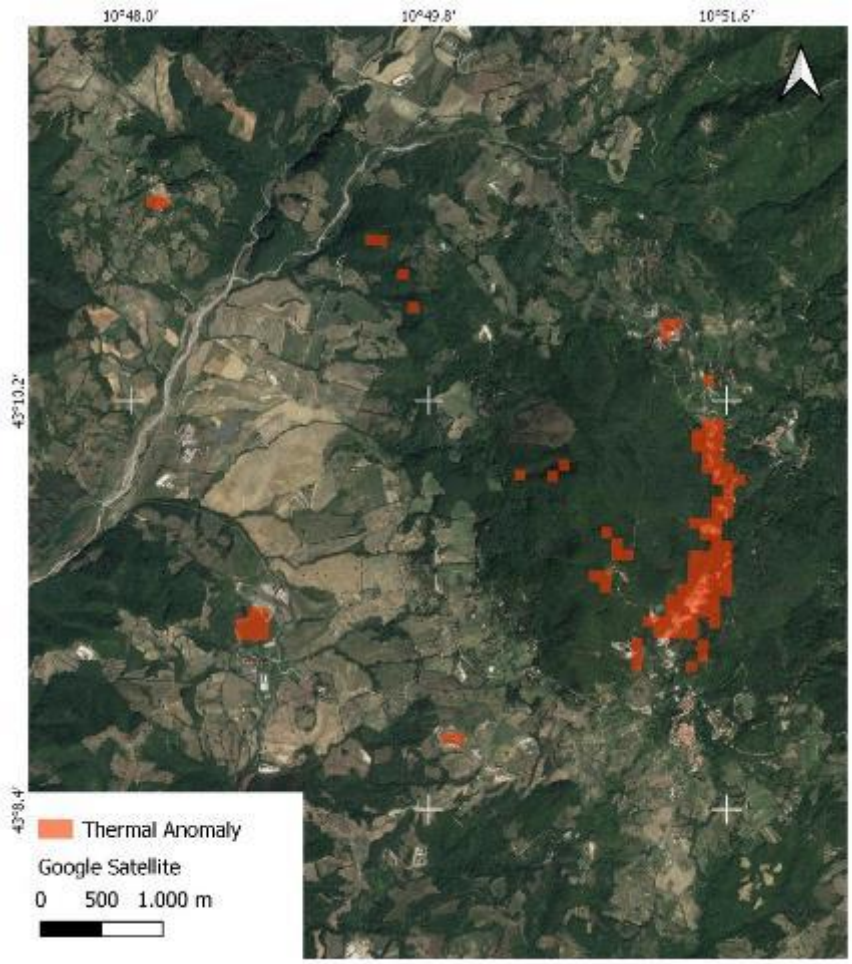

Figure 65. ASTER - The polygons represent the results of the maximum likelihood classification using the cluster A.

Evidence of this aspect can be offered by considering the Normalized Difference Vegetation Index (NDVI). This index is well known and widely used for quantifying green vegetation. It normalizes green leaf scattering in Near Infra-red wavelengths with chlorophyll absorption in red wavelengths. The index range is from -1 to 1. Negative values correspond to water. Values close to zero (-0.1 to 0.1) generally correspond to barren areas of rock, sand, or snow.

Low, positive values represent shrub and grassland (approximately 0.2 to 0.4), while high values indicate temperate and tropical rainforests (values approaching 1). It is a good proxy for live green vegetation. In this case, considering NDVI in four representative maps spanning the 2020 year, it is possible to verify that *Parco delle Biancane* (circled area in Figure 66) is never covered by vegetation. NDVI has been obtained using Copernicus Sentinel 2 satellite that acquires at high spatial resolution (from 10 to 60 meters, in the spectral range from 0.4 to 2.1 μm). In particular, the NDVI has been computed using the two bands at 10 meters. The four dates used as representative for 2020 are 4th March, 8th May, 7th July and 9th November (Figure 66).

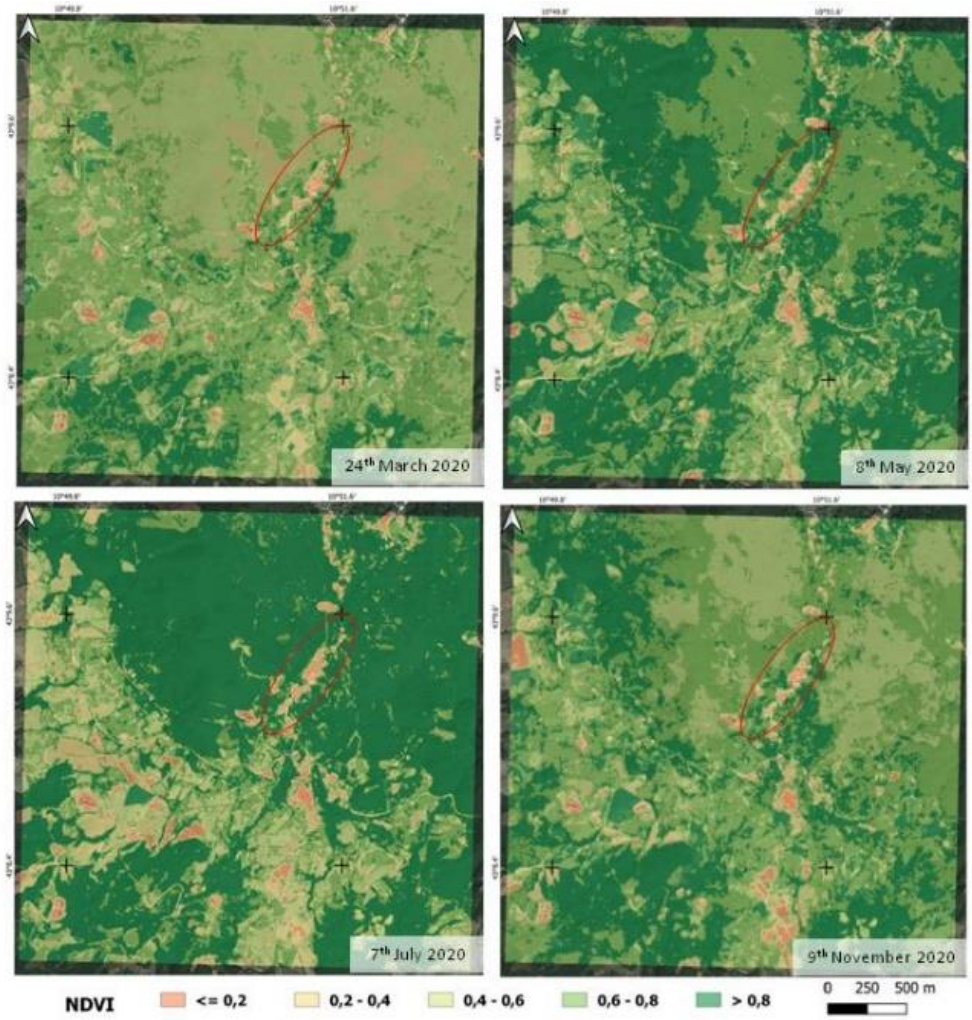

Figure 66. NDVI maps over *Parco delle Biancane* area in four representative dates for 2020. Satellite data used for NDVI estimation are acquired by Sentinel 2 satellite.

In this case, strong thermal anomaly of *Parco delle Biancane* area presents evidence of vegetation stress or absence (Figure 67).

Figure 67. *Parco delle Biancane* area: absence of vegetation is due to the thermal emissions (credits Google Earth).

Analysis on thermal anomalies on *Parco delle Biancane* using LST is not common in literature and no scientific papers are available. For this reason, no comparison with the obtained results are available but, considering the results showed for *Solfatara-Campi Flegrei* test site and thanks to the good agreement with the LST results compared with data collected during field campaigns (see previous Chapter), the confidence on these results is high.

Also in this case, the results of this study demonstrate that satellite data can be a very powerful tool to study surface thermal anomalies quantitatively in remote area even with smaller (wrt *Solfatara-Campi Flegrei*) thermal anomalies.

Parco delle Biancane is surrounded by vegetation and has a thermal contrast with the background lower than the one of *Solfatara* and its background. The hottest point in *Parco delle Biancane* is about 5°C (as showed in Figure 15) while in *Solfatara* is about 10°C (Figure 13). Moreover, *Parco delle Biancane* is in size smaller than *Solfatara* and in a non-urban context. Despite of all these considerations, the applied methodology has demonstrated to be reliable also for this type of area where there is a lack of geophysical information. Indeed, *Parco delle Biancane* has mainly considered from a naturalistic and tourist point of view, while the neighbour *Larderello* and *Monte Amiata* are well studied and with a lot of information because of the industrial exploitation of geothermal

energy since 1904. The contribution of this work is to look closely at this area, outlining the main thermal evidence with respect of the environment.

5.4 Application on *Modena* city for UHI detection

To refine this analysis, the PCA of the 43 LST image has been done (Figure 69). The eigenvalues of the transformation show that the majority, 81%, of the information across time is described by PC1, PC2 and PC3 contributions are both 3%, the other PCs have a very low weight (Figure 68).

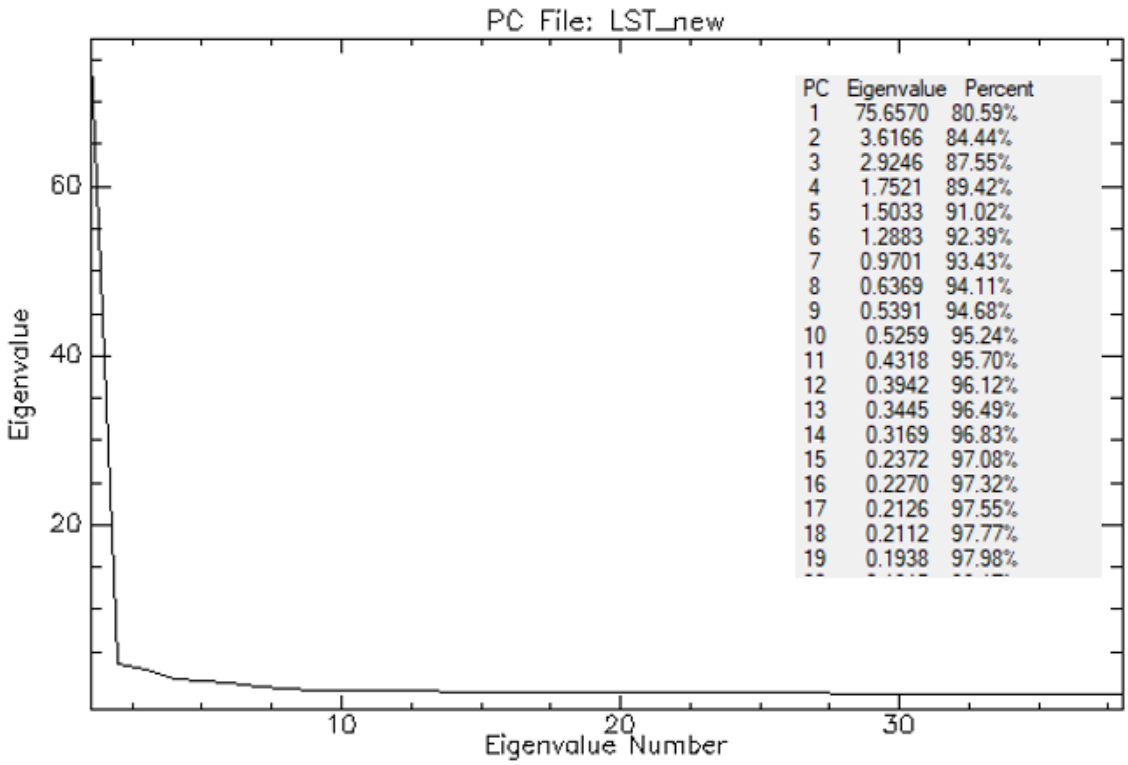

Figure 68. PCA scree plot obtained considering 43 LST Landsat 8 data. In the table the value of each eigenvalue and the cumulative percentage**.**

In Figure 69 the first three PC components are reported.

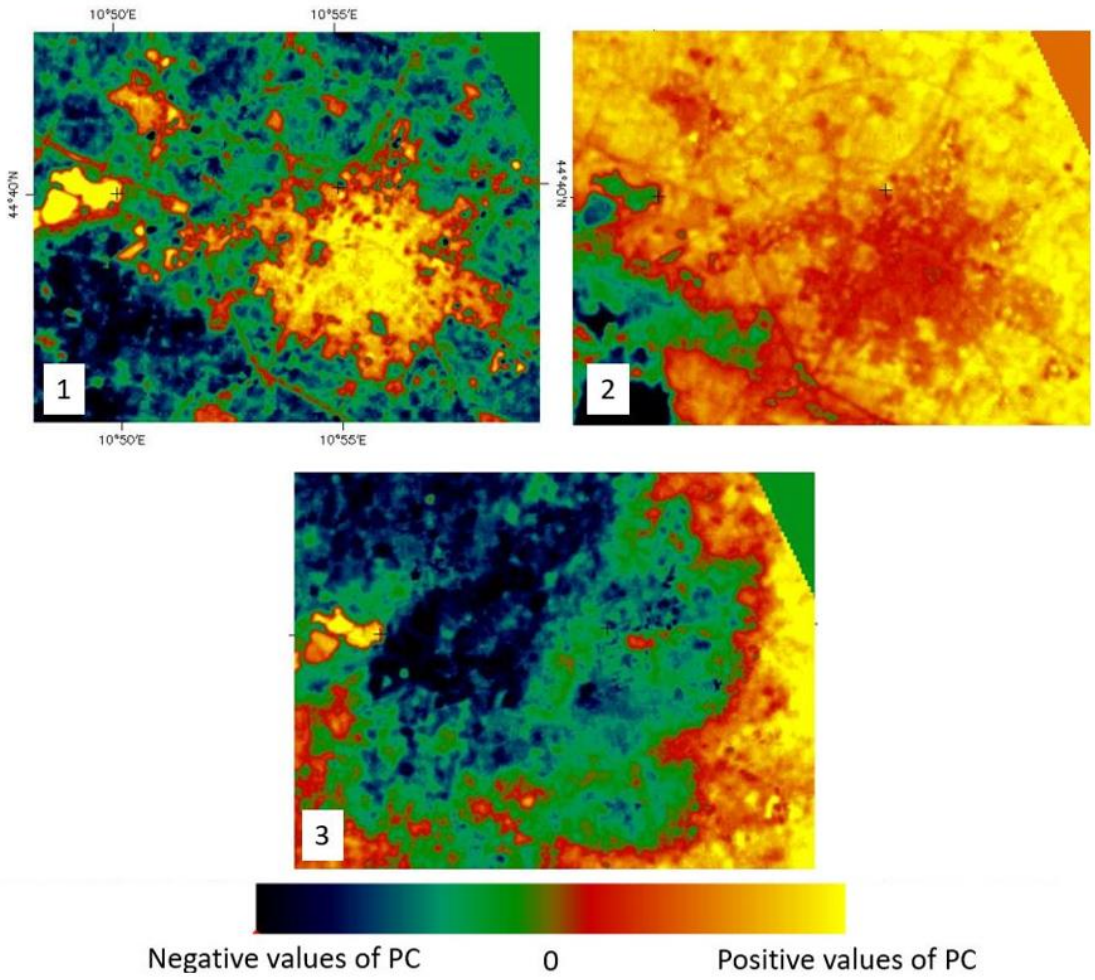

Figure 69. PCA images 1 through 3 derived from LST Landsat 8 time series from 2014 to 2019.

The scatter plot, with density slice colors (Figure 70), of PC1 vs average LST map shows that PC1 furnishes information on mean temporal variation (r=0.999). The standard deviation LST map (standard deviation of the 43 values of each pixel) was computed and compared to PC2 in a similar scatter plot (Figure 70): this comparison shows that PC2 explains a substantial portion of time variability of LST (r= -0.633). PC3 is also linked to LST standard deviation in a way very similar to PC2, i.e. they, more or less, explain similar behaviors.

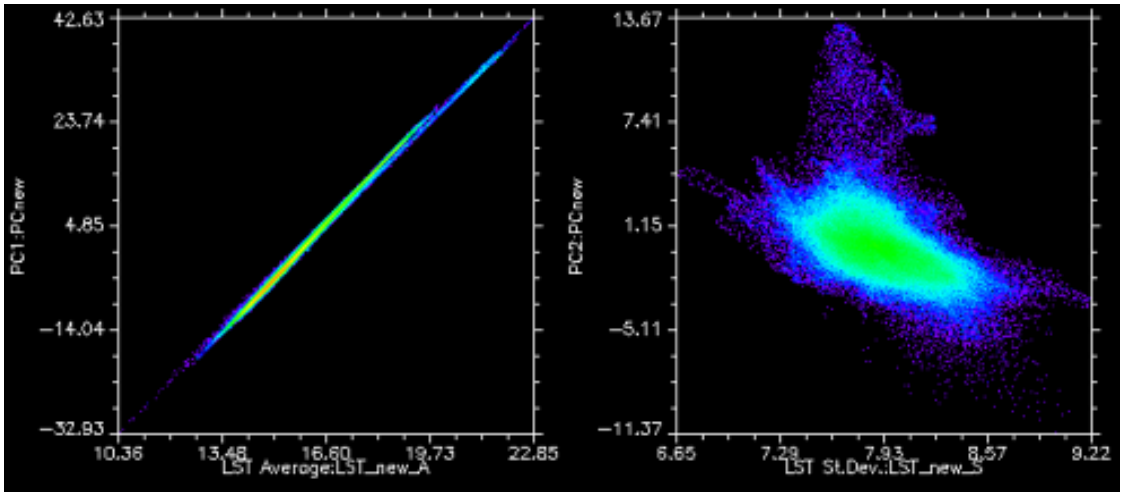

Figure 70. LST average vs PC1 (left, r = 0.999) and LST st.dev. vs PC2 (right, r = -0.633).

Also in this case, as analysed in *Campi Flegrei* and *Parco delle Biancane* areas, Figure 71 shows the correlation between each of the time-steps with the components being diagrammed as well as the mean temperature at each time-step. Also in this case, no seasonality can be observed for the PC1 (green line in Figure 71) and the loadings are consistent over the entire period. The distribution of the PC2 loadings seems to show a seasonal cycle (positive value during autumn/winter and negative during summer/spring).

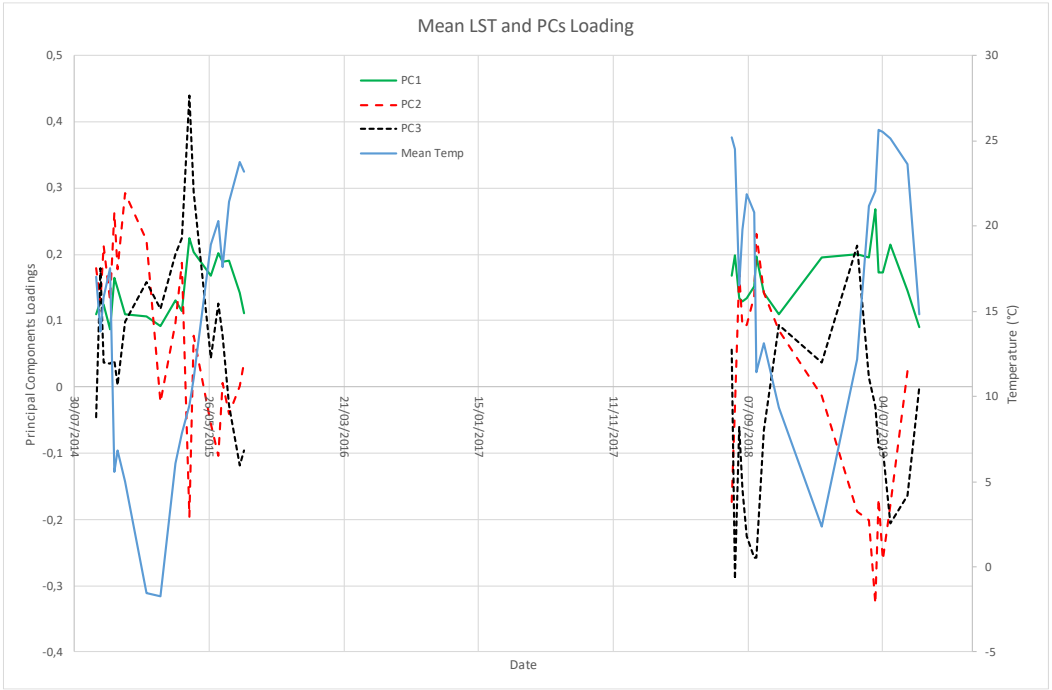

Figure 71. Mean Temperature and Component Loadings (Y-axis) on the original 43 LST Landsat 8 images (X-axis) of the first three principal components. Mean Temperature was calculated for each acquisition date.

PC1 vs PC2 scatter plot, with density slice color, evidences two main clusters (A and B in Figure 72) and an area of sparse points (C in Figure 72). The analysis of this plot showed that the cluster A is mainly composed by built (warm) pixels, the sparse area C indicates water surface (warm) pixels and cluster B is mainly composed by rural pixels.

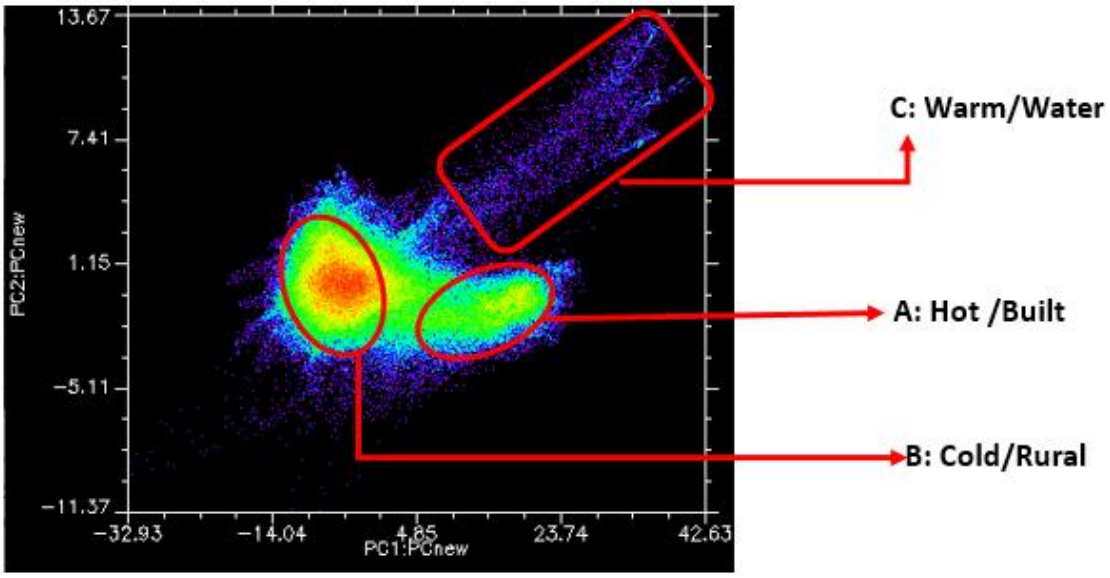

Figure 72. Scatter plot between PC1 and PC2.

Three set of pixels were extracted from the clusters A and B and from the area C and used as endmembers for the maximum likelihood classification. The A and C classes obtained by the classification have been extracted and shown in Figure 73 along with the "0" and "2" isolines. The points of A and C classes represent almost all the warm area included inside the "0" isoline. A class covers built areas, while C covers water surfaces. No points of B class (not represented in figure) are included in the warm region, i.e. they are all outside isoline "0".

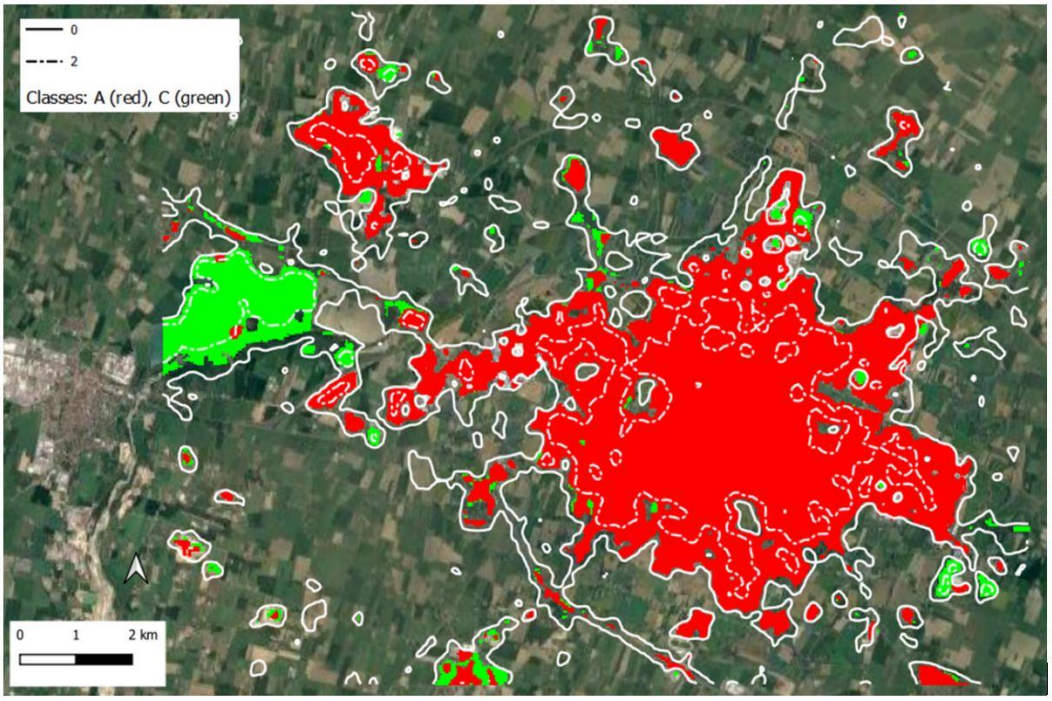

Figure 73. A and C classes, "0" and "2" isolines**.**

The analysis of the 43 Landsat 8 TIRS images furnished indications on the spatial distribution of the mean night time LST.

Using the PCA, it was possible to separate the statistics for rural environment, built areas and water surfaces without additional information on land cover (e.g. classification obtained by VIS/NIR imagery or other land cover database).

The comparison between rural and built areas showed the latter are 2.7 °C (median value) warmer then the first during night time. This temperature raise is higher for water surfaces: 4.8 °C, nevertheless the area covered by water is low compared to the total, thus its contribution to local climate is minor.

The comparison of LST with air temperature measured simultaneously with satellite overpass demonstrated high correlation between the kind type of data, this lead to the conclusion that the temperature LST differences are very similar to air temperature differences and then suitable to UHI characterization.

5.5 Interpretation of PCs for the three test sites

Through the application of PCA on LST time series above three different test sites, the position of cluster, which have been selected considering the PC1

and PC2, is approximatively the same in the three scatter plots (Figure 74). The warm pixels or thermal anomalies in terms of geothermal anomalies or UHI (class A, green line in Figure 74) are located in the same space of the scatter plot (black dotted line of Figure 75), land areas (in terms of background or rural areas, class B of Figure 43, Figure 62 and Figure 72, red line) are included in the black solid line of Figure 75 and water areas (in terms of sea, lake or water surfaces, classified as class C of Figure 43 and Figure 72, yellow line) seem to locate in the same area of scatter plot (are located in the back dash-dotted line of Figure 75).

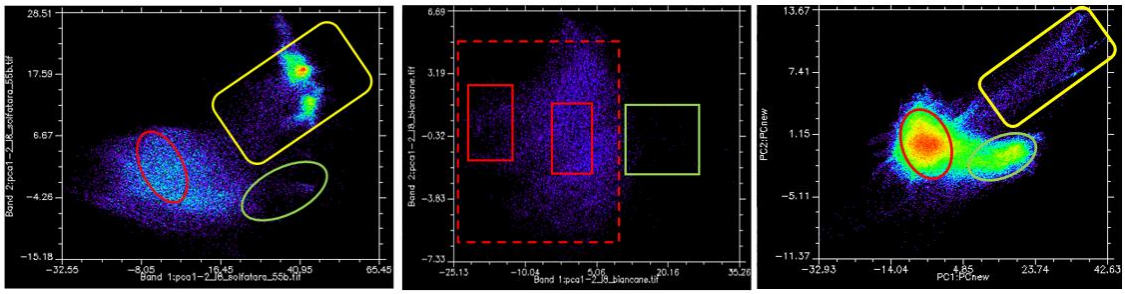

Figure 74. PC1 vs PC2 cluster: *Campi Flegrei* (left), *Parco delle Biancane* (middle), *Modena* City (right). Yellow line represents the water cluster, red line the background (land, rural areas) and green line represents the thermal anomaly or warm area due to UHI.

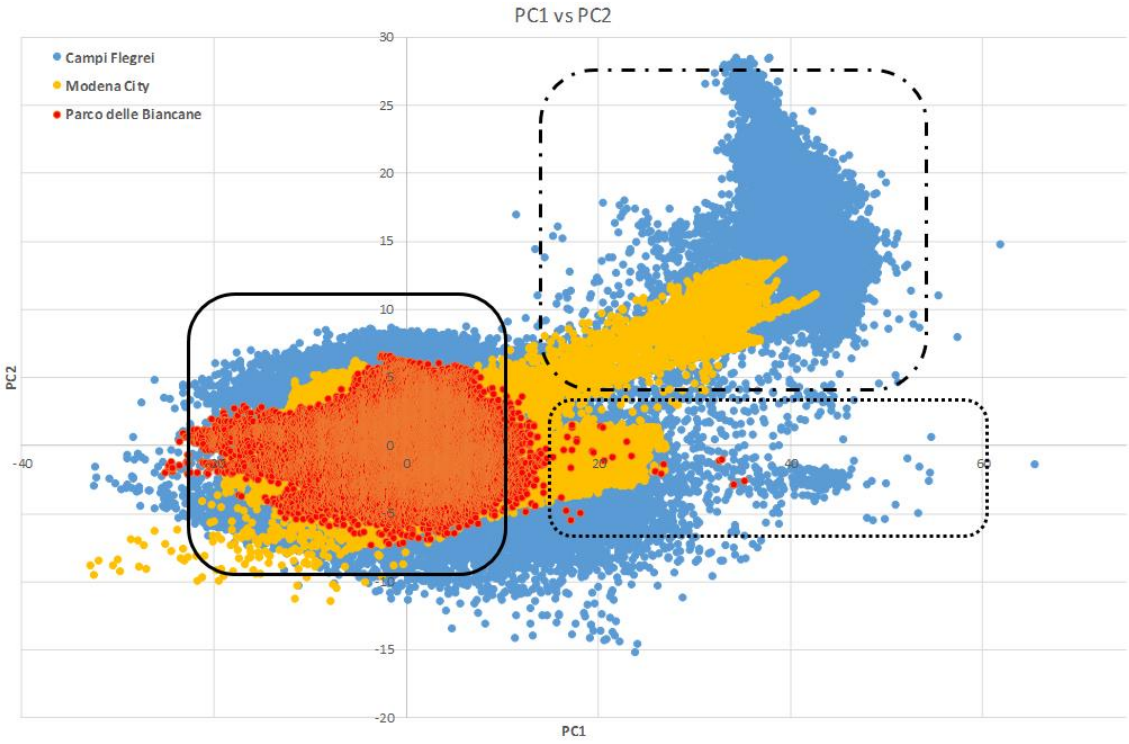

Figure 75. PC1 vs PC2 of the three test sites. Dash-dotted line represents the water cluster, solid line the background (land, rural areas) and dotted line represents the thermal anomaly or warm area due to UHI.

Next steps will be the deduction of a classification scheme based on the principal components. This solution could be applied to the component values to order and group grid cells of similar thermal behavior into several classes that could be used for a better classification of the sites.

Other work that will be considered for a future analysis is the study of PCs for a distinction between seasonal changes in thermal variability. For example, PCs of LST time series could be better analysed into di classes representing the behavior for different seasons.

5.6 References of chapter 5

78. Harris, A. J., Butterworth, A. L., Carlton, R. W., Downey, I., Miller, P., Navarro, P., & Rothery, D. A. (1997). Low-cost volcano surveillance from space: case studies from Etna, Krafla, Cerro Negro, Fogo, Lascar and Erebus. Bulletin of Volcanology, 59(1), 49-64.
79. Higgins, J., & Harris, A. (1997). VAST: a program to locate and analyse volcanic thermal anomalies automatically from remotely sensed data. Computers & Geosciences, 23(6), 627-645.
80. Lago González, D., & Rodríguez-Gonzálvez, P. (2019). Detection of Geothermal Potential Zones Using Remote Sensing Techniques. Remote Sensing, 11(20), 2403.
81. Abubakar, A. J. A., Hashim, M., Pour, A. B., & Shehu, K. (2017). A review of geothermal mapping techniques using remotely sensed data. Science World Journal, 12(4), 72-82.
82. Avtar, R., Sahu, N., Aggarwal, A. K., Chakraborty, S., Kharrazi, A., Yunus, A. P., ... & Kurniawan, T. A. (2019). Exploring renewable energy resources using remote sensing and GIS—A review. Resources, 8(3), 149.
83. Eklundh, L., & Singh, A. (1993). A comparative analysis of standardised and unstandardised principal components analysis in remote sensing. International Journal of Remote Sensing, 14(7), 1359-1370.
84. Henebry, G. M., & Rieck, D. R. (1996, May). Applying principal components analysis to image time series: effects on scene segmentation and spatial structure. In IGARSS'96. 1996 International Geoscience and Remote Sensing Symposium (Vol. 1, pp. 448-450). IEEE.
85. Singh, A., & Harrison, A. (1985). Standardized principal components. International Journal of Remote Sensing, 6(6), 883-896.
86. Mas, J. F. (1999). Monitoring land-cover changes: a comparison of change detection techniques. International journal of remote sensing, 20(1), 139-152.

87. Gaitani, N., Burud, I., Thiis, T., & Santamouris, M. (2017). High-resolution spectral mapping of urban thermal properties with Unmanned Aerial Vehicles. Building and Environment, 121, 215-224.
88. Vázquez-Jiménez, R., Ramos-Bernal, R. N., Romero-Calcerrada, R., Arrogante-Funes, P., Tizapa, S. S., & Novillo, C. J. (2018). Thresholding algorithm optimization for change detection to satellite imagery. In Colorimetry Image Processing. InTech.
89. Müller, B., Bernhardt, M., & Schulz, K. (2014). Identification of catchment functional units by time series of thermal remote sensing images. Hydrology and Earth System Sciences Discussions, 11(6), 7019–7052. doi:10.5194/hessd-11-7019-2014
90. ENVI software, https://www.harrisgeospatial.com/Software-Technology/ENVI (accessed on 24 April 2021).
91. Bollettino Campi Flegrei_2019, https://www.ov.ingv.it/ov/bollettini-mensili-campania/Bollettino_Mensile_Campi_Flegrei_2019_12.pdf (accessed on 29 April 2021)
92. Marotta, E., Peluso, R., Avino, R., Belviso, P., Caliro, S., Carandente, A., ... & Marfè, B. (2019). Thermal Energy Release Measurement with Thermal Camera: The Case of La Solfatara Volcano (Italy). Remote Sensing, 11(2), 167.
93. Hirosawa, Y., Marsh, S. E., & Kliman, D. H. (1996). Application of standardized principal component analysis to land-cover characterization using multitemporal AVHRR data. Remote Sensing of Environment, 58(3), 267-281.
94. Wang, T., Kou, X., Xiong, Y., Mou, P., Wu, J., & Ge, J. (2010). Temporal and spatial patterns of NDVI and their relationship to precipitation in the Loess Plateau of China. International Journal of Remote Sensing, 31(7), 1943-1958.
95. de Almeida, T. I. R., Penatti, N. C., Ferreira, L. G., Arantes, A. E., & do Amaral, C. H. (2015). Principal component analysis applied to a time series of MODIS images: the spatio-temporal variability of the Pantanal wetland, Brazil. Wetlands ecology and management, 23(4), 737-748.
96. Cappetti, G., Romagnoli, P., & Sabatelli, F. (2010). Geothermal power generation in Italy 2005–2009 update report. In Proceedings world geothermal congress (p. 8).
97. Enel Green Power web site https://www.enelgreenpower.com/countries/europe/Italy (accessed on 29 April 2021).
98. Minissale, A. (1991). The Larderello geothermal field: a review. Earth-Science Reviews, 31(2), 133-151.

6 CONCLUSION AND FINAL CONSIDERATIONS

6.1 Conclusion

In this work, LST estimation techniques applied to the remote sensing data offering a systematic and precise detection of thermal anomalies and UHI. LST was retrieved by two methodologies and results were validated thanks to ground measurements collected during field campaigns or fixed measurements station and/or cross-validation technique. The main analyses were conducted using nighttime satellite data, in order to reduce the solar effects and comparison results showed very good agreements. However, also comparison of ground data collected during the morning and LST retrieved by daytime satellite data showed good agreements. For these reasons, the methodologies used to obtain LST produce good temperature estimates in the very particular case of geothermal anomalies and usable for near ground air temperature trends analysis.

The use of two sensors (ASTER and Landsat 8), despite the different GSD and LST methodologies, have produced results with high correlation offering the possibility to extend the LST time series. ASTER is one of the more versatile satellite imagers used for studies of thermal anomalies; it can estimate surface temperatures with several thermal infrared spectral channels. TIRS/Landsat 8 images, while having fewer spectral channels and slightly lower spatial resolution than ASTER, provide additional temperature data for estimating and monitoring LST on active volcanoes as well as geothermal areas. The use of two sensors has proven cost-effective technical method for generating products for the detection of geothermal anomalies and UHI.

PCA on LST time series allows for a derivation of direct indicators of thermal anomalies “removing” the effect of seasonality that is visible in the LST time series. In this way, in case of thermal anomalies connected to geothermal fields, satellite data could be successfully integrated with low cost techniques by means of UAVs adapted to optimize thermal, geochemical and geomorphologic measurements in selected sites.

The use of PCA offers the possibility to automatically classify some basic surface cover types, as built areas and waters, without using auxiliary information as remote sensing images acquired in the Visible-Near Infrared regions. This simple classification allows the analysis of the thermal behavior of urban and rural areas separately, that is, facilitates the characterization of urban climate zone. This last is an important aspect for the evaluation of the spatial-temporal dynamic change of urban areas, and provide the decision support for further sustainable urban planning.

With this work, a robust and easy-to-use procedure for the thermal anomaly detection has been applied. The proposed methodology can be easily replicated, ensuring the conceptual correctness and reproducibility of image processing. Despite the results reported in this work concern three different test sites located in Italy, their differences show that the procedure could be applied on different geological settings and manmade related environments. This means that it can be exported with no particular limitation for studying natural event in remote area or/and UHI for both villages or cities. Besides its exportability and reproducibility, this methodology could be considered in the preliminary steps of new geothermal field exploration as costless methodology to identify area of interest where exploit more accurate analysis. At the same time this procedure may support who is in charge to plan the city management and development highlighting the thermal behavior of urbanized area.

6.2 Limitations in the research

Some limitations should be considered in this work. The number of cloud-free satellite acquisition, respect to the nominal revisit time (16 days for ASTER and Landsat 8) is strongly reduced if we consider the analysed long time.

Other constrains are the sensor spatial and radiometric resolutions. At today, due to the available sensors acquiring in thermal region, only anomalies with geometrical dimension of the same order of GSD or with high radiative power can be detected. Most of the geothermal manifestations having areas larger than GSD used, such as craters or fumarolic fields, have been detected as geothermal anomalies with the approaches described in this thesis. However, thermal manifestations in areas smaller than GSD used, or having a small thermal anomaly require different methodologies strongly customized for each different size. Therefore, the proposed methodology is able to detect areas with temperatures greater than 5 °C above ambient temperature (as showed in Figure 36 and Figure 54).

Validation of LST is of crucial importance for estimating the accuracy of the final product. In this thesis this step has been deployed for *Solfatara-Campi Flegrei* and *Modena* city ensuring the performance of the procedure also for the *Parco delle Biancane*. As a final remark, the availability of the in-situ data in synchronous with satellite acquisitions offers the advantage to validate the methodologies used for LST estimation and then the reliability on the proposed methodology.

6.3 Final considerations

Thermal data can have an important role in the delineation of surface temperature anomalies associated with a geothermal activity and for the measurement of near-surface heat fluxes associated with geothermal systems as input for monitoring and resource assessment.

The two studied cases represent two more demonstrations of the potentiality of satellite observations in TIR for environmental applications and confirm the request to the remote sensing community for a continuous improvement of satellite sensors in the TIR, especially in terms of spatial resolution.

A future development of this work will be to analyze time series of satellite thermal data using Landsat 8, ASTER thermal data (90 m pixel spatial resolution) and the last ECOSTRESS (69 m × 38 m pixel spatial resolution at nadir and with a temporal resolution of 3-4 days), in order to observe changes in the surface temperatures using a LST.

This study wants also to support the interest for the future developments of sensors that have characteristics to perform regional analyses whit high spatial resolution, in a shorter time respect to the current availability.

ACRONYMS

ASTER	Advanced Spaceborne Thermal Emission and Reflection Radiometer
ASTER-GED	ASTER Global Emissivity Dataset
DEM	Digital Elevation Model
DSM	Digital Surface Model
DN	Digital Number
ECOSTRESS	ECOsystem Spaceborne Thermal Radiometer Experiment on Space Station
EO	Earth Observation
EOS	Earth Observing System
GCP	Ground Control Points
GSD	Ground Sample Distance
HyTES	Hyperspectral Thermal Emission Spectrometer
INGV	Istituto Nazionale di Geofisica e Vulcanologia
IR	InfraRed
LSE	Land Surface Emissivity
LST	Land Surface Temperature
MMD	Maximum-Minimum Difference
MODIS	Moderate Resolution Imaging Spectroradiometer
MODTRAN	MODerate resolution atmospheric TRANsmission
MSG	Meteosat Second Generation
NASA-JPL	National Aeronautics and Space Administration -Jet Propulsion Laboratory
NDVI	Normalized Difference Vegetation Index
NEM	Normalized Emissivity Method
OLI	Operational Land Imager

PCA	Principal Component Analysis
RTE	Radiative Transfer Equation
TES	Temperature and Emissivity Separation
TIR	Thermal InfraRed
TIRS	Thermal InfraRed Sensor
TOA	Top of Atmosphere
SCA	Single Channel Algorithm
SLSTR	Sea and Land Surface Temperature Radiometer
SWIR	Short Wave InfraRed
UAV	Unmanned Aerial Vehicles
UHI	Urban Heat Island
USGS	United States Geological Survey
VNIR	Visible and Near-InfraRed